MAGNESIUM HYDROXIDE SORBENTS FOR COMBINED CARBON DIOXIDE CAPTURE AND STORAGE IN ENERGY CONVERSION SYSTEMS

Kyle J. Fricker

Submitted in partial fulfillment of the
Requirements for the degree of
Doctor of Philosophy
In the Graduate School of Arts and Sciences

COLUMBIA UNIVERSITY

2014

ABSTRACT

Magnesium Hydroxide Sorbents for Combined Carbon Dioxide Capture and Storage in Energy Conversion Systems

Kyle J. Fricker

Ever increasing anthropogenic emissions of greenhouse gas carbon dioxide (CO_2) are considered as the main driving force behind climate change on Earth. The environmental impacts of greenhouse gases will be further intensified as the world's population continues grow while the developing world is modernized concurrently. Three solutions exist, and each must be pursued in parallel. CO_2 emissions can be reduced by improving the energy efficiency across all sectors, hastening the transition to carbon-free energy sources like solar and wind power, and developing carbon capture and storage (CCS) technologies. Despite the incentives surrounding carbon-free energy, it will take decades until significant market penetration is achieved. In the meantime, while carboneous fossilized energy sources continue to dominate the energy blend and worldwide energy demand is continuously increasing, CCS can offer an immediate solution to fight climate change. Furthermore, CCS has the potential to stabilize or even reduce the atmospheric CO_2 concentration.

Several high temperature CO_2 capture technologies are under development. Chemical looping of calcium (Ca) sorbents is predicted to provide zero emission energy from coal. Ca-based sorbents must be recycled given the natural state of most Ca in the Earth's crust as calcium carbonate. Looping raises concerns about the ultimate fate of the separated CO_2 as well as the degradation of the sorbent material. Unlike their Ca-based counterparts, Mg-bearing sorbents, derived from silicate minerals and industrial wastes,

can act as combined carbon capture and storage media in various energy conversion systems. By combining CO_2 capture and storage, energy intensive sorbent regeneration and uncertainties associated with geological sequestration of CO_2 can be avoided. The magnesium carbonate formed during the carbon mineralization process is recognized as the most safe and permanent method to store anthropogenic CO_2. Locked within the mineral carbonate crystal structure, CO_2 achieves its lowest energy state. Despite the benefits of Mg carbon mineralization, the reactions experience limitations in terms of kinetics and overall conversion, depending on the reaction system, and the mechanisms are not well understood, especially at high temperature and pressure conditions.

$Mg(OH)_2$ carbonation in the slurry phase occurs spontaneously and recent results show improved gas-solid carbonation with comparable materials in the presence of H_2O vapor. The pathways of H_2O enhanced $Mg(OH)_2$ carbonation were investigated at elevated temperatures and CO_2 pressures (up to 400 °C and 15 atm) in the presence of steam. For a given reaction temperature, carbonation conversion showed dramatic increase with increasing H_2O loading. The results suggest that a hydrated environment facilitates the formation of intermediate hydrated magnesium carbonate species. The hydrated carbonates form relatively quickly and can transform into anhydrous carbonates while subjected to greater H_2O loading, higher temperature, and/or longer reaction time. Still, carbonation of $Mg(OH)_2$ in a gas-solid system has largely demonstrated limited reaction kinetics and overall conversion.

The limitations observed in the gas-solid carbonation reaction and the enhanced effect of steam motivated a series of studies around slurry phase $Mg(OH)_2$ carbonation. The literature lacked an investigation of $Mg(OH)_2$ slurry carbonation at elevated temperature,

thus this study examined carbonation at moderate temperature and CO_2 pressure (up to 200 ºC and 15 atm). Various metastable hydrated magnesium carbonates (e.g. $MgCO_3 \cdot 3H_2O$ and $Mg_5(CO_3)_4(OH)_2 \cdot 4H_2O$), with differing amounts of hydroxide and structural H_2O incorporated within the carbonate crystal, tend to form quickly and persist for long periods of time in aqueous systems, complicating the reaction engineering. The reaction conditions responsible for hydrated and anhydrous carbonate product phases were evaluated and carbonate formation kinetics were investigated. Reaction temperature was found to be the dominant parameter driving the formation of specific carbonate phases, though solution additives also showed potential for bypassing the temperature effect.

Magnesite (anhydrous magnesium carbonate, $MgCO_3$) is the most desirable phase within the magnesium carbonate family for carbon storage for a number of reasons, including its magnesium efficiency, omission of additional crystal waters and thermodynamic stability. For large-scale carbonation to be a viable industrial process, magnesite precipitation, which is known to have slower nucleation and growth rates than its metastable competitors, must be made to occur rapidly and reliably. Furthermore, the reaction conditions required for the formation of each magnesium carbonate phases have not been well understood with conflicting literature data. In this study, the effects of both magnesite and inert (Al_2O_3) seed particles on the precipitation of magnesium carbonates from a $Mg(OH)_2$ slurry were explored. It was interesting that $MgCO_3$ seeding was shown to accelerate anhydrous magnesite growth at temperatures (80-150 ºC), where it would normally not form in short time scale. Since the specific surface areas of $MgCO_3$ and Al_2O_3 seeding particles were similar, this phenomenon was due to the difference in the

surface chemistry of two seeding particles. By providing a template with similar chemistry for the growth of magnesite, the precipitation of anhydrous magnesite was demonstrated.

After the in depth study of $Mg(OH)_2$ carbonation in both gas-solid and slurry arrangements, its integration with an energy conversion process, the water gas shift reaction (WGSR), was explored to increase the sustainability of carboneous energy sources. Due to the limitations witnessed in the gas-solid carbonation system, this study investigated the integration of slurry phase $Mg(OH)_2$ carbonation with the WGSR at temperatures up to 215 °C with a 0.5 wt% platinum on alumina catalyst. The removal of CO_2 by the carbonation reaction enhanced hydrogen yield of the WGSR as the equilibrium of the gas phase reaction was shifted towards products. Unexpectedly, a side reaction was exposed, which converted CO to aqueous formate ion and limited the overall production of hydrogen. The formate can persist in solution or decompose to yield hydrogen depending on the solution conditions. This study also tested industrial catalysts and proposed various practical reactor arrangements for the integrated system.

Overall, this study explored the fundamental chemistry relating to carbonate phase formation mechanisms and kinetics during the carbonation reaction of $Mg(OH)_2$ in various reactor systems. $Mg(OH)_2$ carbonation is under continued development as a combined CO_2 capture and storage technology. The integration of the carbonation system with an energy conversion process motivated the investigation at elevated temperature and CO_2 pressure conditions. Ultimately, the carbonation reaction was integrated with the WGSR to capture and store the produced CO_2 as well as enhance the production of H_2.

Table of Contents

List of Figures

List of Tables

Acknowledgments

First, I must thank my mentor, Professor Ah-Hyung ("Alissa") Park, who guided me through each stage of my doctorate degree. I am deeply grateful that she saw my potential and even lobbied for me to stay in graduate school beyond the Master of Science degree. Her motivation and diligence inspired me, and thankfully my dissertation was funded by her grant-writing prowess (NSF CAREER Award #0846846).

Many thanks also to my esteemed committee members: Dr. Paul Duby, Dr. Robert ("Bob") Farrauto, Dr. Patricia Culligan, and Dr. Patrick Brady. Specifically, Professors Farrauto and Duby have followed my research and taught me a range of fascinating topics, including the complexities of catalyst activity and the construction of a metallurgical phase diagram.

The Park Group has been there for me from day one. Whether it was to critically review a manuscript, assist with repetitive analyses, provide moral support over a burrito, troubleshoot my experimental apparatus, or sit through the hours of group presentations over the years (and offer excellent feedback!), I am forever grateful for all that you have done. In no particular order, I would like to thank: Mr. Zidu Tang, Dr. Camille Petit, Mr. David Dogon, Dr. Huangjing Zhao, Dr. Greeshma Gadikota, Mr. Thomas Ferguson, Mr. Xiaozhou Zhou, Dr. Andrew Lin, Dr. Youngjune Park, Dr. Edward Swanson, Mr. Maxim Stonor, Mr. Nabil Ashraf Sisani, Ms. Micaela Naibryf, and Mr. Luis Abrego.

Outside of the Park Group there were numerous friends and colleagues at Columbia always there to assist with tangential scientific pursuits, bounce ideas off of, pick me up on those rough days, enjoy a nice summer afternoon at Amsterdam Café, and

philosophize about the Ph.D. and our futures. First to mind are Dr. Rob van Haaren, Mr. Jared Roseman, Dr. Garrett Fitzgerald, and Mr. Timothy Sharobem, though there are many more and simply not enough space to list you all. Thanks for everything.

My good friends around New York and beyond (you know who you are!) deserve recognition. You have showed me what it is to live a fun and full life outside of the lab. Your care and support is invaluable. Let's hangout after this is all done!

I cannot thank my family enough for the years of love. My sisters, Ms. Kate Fricker and Ms. Emily Fricker, and I have gotten much closer (despite huge geographic distances) during my time at Columbia, and I am excited to experience our shared future. My parents, Mr. Eric Fricker and Mrs. Susie Fricker, have never wavered in their support. I strive to emulate their open-mindedness and compassion, and I am forever thankful for their guilt-free parenting, always pushing me to find true happiness.

Finally I would to thank my fiancée, Ms. Jessica Greenbaum, for her unconditional love and encouragement during my Ph.D. She has been there through thick and thin, always there to make me smile at the end of day. Also, through Jess I have been invited into the Greenbaum family, and, in particular, I would like to acknowledge Mr. David Greenbaum, Mrs. Laureine Greenbaum, Mr. Gabe Libhart, and Mrs. Allie Libhart for their kindness and generosity over the past years.

For Eric and Susie

1. Introduction

Population growth stands among the largest environmental challenges facing the World today. Said best by Albert Einstein: “The latest phase of technical-scientific progress, with its fantastic increases in population, has created a situation fraught with problems of hitherto unknown dimensions.” Being finite, the Earth can only support as many humans as its resources will allow. The developed world (Europe, North America, Australia/New Zealand, and Japan) population is projected to level off over the next century; however, less developed regions (Africa, Asia (excluding Japan), Latin America, the Caribbean, Melanesia, Micronesia and Polynesia) are expected to continue their rise (Figure 1.1). By 2060, the United Nations predicts world population to surpass 10 billion people, with nearly all of the growth from 2020 and beyond occurring in the developing world (UN, 2012). While these regions grow in population, they will certainly undergo technological development and experience vast upgrades in life quality; however, as Einstein pointed out, these changes will undoubtedly result in challenges requiring truly innovative engineered solutions.

Both population growth and life quality improvement require energy. Energy has become a basic human need, along with food, water, and shelter. The evidence surrounds us; energy is needed across all sectors and at all segments of the value chain. A closer look into agriculture infrastructure reveals our intertwined relationship with energy. Energy is found in the machines for working the land and the production of those machines, development and production of fertilizers and pesticides, mechanization in processing the crop, transportation of products to market, cooking and use of said products, and transportation of the waste. The problems surrounding the usage of energy

lie in the depletion of non-renewable resources and the potential environmental impacts related to the use of various energy sources.

The International Energy Agency's biennial report, *World Energy Outlook*, provides historical energy data and produces projections based on their assessment of current and future energy policies (IEA, 2013). Projections include announced and planned policy changes that may not be in effect in 2013 but are expected to come to fruition. From Figure 1.2(a) it is observed that the majority of the world's installed energy capacity is composed on non-renewable coal, gas, oil, and nuclear energy sources. This trend is forecasted to continue, though by 2035 renewable energy sources including hydropower, wind, and others like solar will grow in their respective market share. Despite the increased presence of renewable sources, non-renewable energy sources will continue to dominate the energy mix, even used at a larger rate than today, simply due to the increased demand expected as a result of population and life quality increases.

If similar data is separated by the countries level of development, significant differences appear. Figure 1.2(b) shows the quantity of electricity generated from each energy source for Organisation for Economic Co-operation and Development (OECD) member states and non-OECD countries. It is apparent that energy policies in OECD countries are promoting the development of renewable energy sources and natural gas, a cleaner burning fossil fuel than coal. Electricity derived from coal decreases over the next 21 years while nuclear is maintained. In the OECD countries energy demand is relatively stable. Conversely, energy demand in non-OECD countries is growing along with quality of life. Aside from oil, electricity generation is growing with respect to each energy source, including coal.

When environmental impacts of energy sources are considered, the real costs associated with the use of non-renewable fossilized hydrocarbon fuels, like coal, oil, and gas, can be assessed. Fossilized hydrocarbon fuels, and coal in particular, release CO_2 when they are burned to produce energy along with a host of other harmful compounds and residues. Generally, consensus exists in the scientific community about the link between the emissions of CO_2 and other greenhouse gases and anthropogenic climate change (IPCC, 2013). The increases in atmospheric CO_2 concentration are visualized in Figure 1.3(a). In the 50 years from 1960 to 2010, CO_2 levels increased over 20%. Since CO_2 is soluble in water, the increased levels of CO_2 in the atmosphere result in increased concentrations of CO_2 and higher acidity in seawater, which threatens marine ecosystems (Figure 1.3(b)). The quintessential indicator of climate change is that of global mean surface temperature increases. Figure 1.3(c) contains the temperature anomaly data as a function of cumulative anthropogenic CO_2 emissions. It should be noted that small average temperature increases of only a few degrees Celsius can have dramatic impact on the Earth's natural systems. The latest report from the Intergovernmental Panel on Climate Change (IPCC) basically concluded that enough CO_2 has already been emitted to cause irreversible harm, unless the atmospheric CO_2 levels could actually be reduced (IPCC, 2013).

Not one cure exists for the CO_2 problem; all solutions must be explored with the best ones implemented. Pacala and Socolow dubbed the various solutions 'stabilization wedges,' noting that the carbon imbalance could be reversed using only technology already developed (Pacala & Socolow, 2004). When all wedges are combined, emission reductions are achievable and atmospheric CO_2 concentration can stabilize. Using an all-

around approach means developing and implementing clean, renewable energy solutions as well as mitigating the effects of the inevitable continued use of fossilized hydrocarbon fuels. The carbon capture and storage (CCS) field is poised to reduce greenhouse emissions for the time it takes to transition to renewable energy sources, which could take centuries. Direct air capture of CO_2 and subsequent storage is the only solution which can actually reverse the trend and decrease the concentration of CO_2 in the atmosphere in the long run (Lackner, 2009).

Numerous technologies exist for capturing and storing CO_2, each with their own benefits and challenges. The technology disclosed herein is an engineered ex-situ carbon mineralization process. Carbon mineralization is a natural phenomenon whereby CO_2 reacts with alkaline earth minerals to form carbonate minerals, like limestone. The natural process occurs over geological timescales and cannot maintain pace with the rate of anthropogenic CO_2 emission. This technology captures and stores CO_2 as a carbonate mineral, which is highly stable and could be utilized as a construction material or simply stored safely for ages. The majority of this study investigates the reaction between magnesium hydroxide ($Mg(OH)_2$) and CO_2 in both gas-solid and gas-liquid-solid arrangements to elucidate the reaction pathways and relevant chemical phenomena. Subsequently, the carbon capture and storage process is integrated with an energy conversion reaction, the water gas shift reaction, to explore the synergistic effect of enhancing hydrogen production by separating carbon dioxide. Combined carbon capture and storage via Mg-bearing sorbents is a research area under continued development within the Park group and across the world. Ultimately the fundamental understanding of

the chemistry can lead to development of an industrial process or spinoff technology. The organizational structure of this study is as follows:

Chapter 2 examines the background information necessary to make a case for the following research. The relevant literature in the field of carbon dioxide capture and storage is organized, with specific emphasis on studies which utilized $Mg(OH)_2$ as a sorbent material. The chapter introduces the notion to integrate the CCS technology with an energy conversion system, and also details the specific scientific questions and objectives of the dissertation.

Chapter 3 brings perspective to the proposed combined CO_2 capture and storage technology. One possible application involves the decarbonization of a process for converting waste plastic to liquid fuel via a gasification and Fischer-Tropsch reaction system. A literature study on the key parameters influencing gasification of carboneous materials is presented. Subsequently, a comparative life cycle analysis of the waste conversion process with an alternative energy recovery from waste technology, incineration, shows the need for integrated CO_2 capture and storage with such operations.

Chapter 4 examines the gas-solid reaction between CO_2 and $Mg(OH)_2$ to understand the fundamental chemistry and limitations of the sorbent material. Various pathways to carbonate $Mg(OH)_2$ are proposed and investigated systematically. The effect of temperature, CO_2 pressure, and the presence of H_2O on gas-solid $Mg(OH)_2$ carbonation is noted, and a mechanism for carbonation in the presence of H_2O through a hydrated magnesium carbonate intermediate follows.

Chapter 5 continues from the critical finding of Chapter 4, that H_2O is a promoter of carbonation, to investigate the carbonation of $Mg(OH)_2$ in a highly hydrated system. The slurry phase $Mg(OH)_2$ investigation reveals the effect of temperature on carbonation, which is the key parameter in determining the magnesium carbonate phase produced as well as the formation kinetics of that phase. Understanding the formation of metastable hydrated magnesium carbonates is crucial since the anhydrous carbonate is desirable in terms of both permanence and efficiency. Generally, higher temperatures (above 100 °C, depending on the CO_2 pressure) favor formation of the more stable anhydrous carbonate phase. Solution additives show their potential to interfere with the metastable species and promote anhydrous carbonate formation.

Chapter 6 provides a novel approach to avoiding the production of metastable hydrated carbonates in aqueous magnesium carbonation systems. First, a detailed literature review reveals confusion within the literature caused by the kinetic inhibition in forming anhydrous magnesium carbonate, which is the most thermodynamically stable carbonate at all temperature and P_{CO2} conditions. Subsequently, the chapter investigates the concept of seeding the mixture with anhydrous carbonate particles to produce the desired phase at conditions where it is normally not favored.

Chapter 7 returns to the application the $Mg(OH)_2$ sorbent system to an energy conversion process. The water gas shift reaction (WGSR) is integrated with the slurry carbonation system to explore the synergies. CO_2 uptake by the sorbent should shift the equilibrium of the gas phase WGSR. The chapter includes an investigation of the complexities of the system, including the elusive formation of formate ions which limit

the conversion of carbon monoxide to hydrogen. Reactor arrangements and methods to bypass the issue of formate buildup within the aqueous phase are proposed.

Lastly, in Chapter 8, the conclusions of the study are summarized with recommendations for future work to expand on concepts developed in this dissertation.

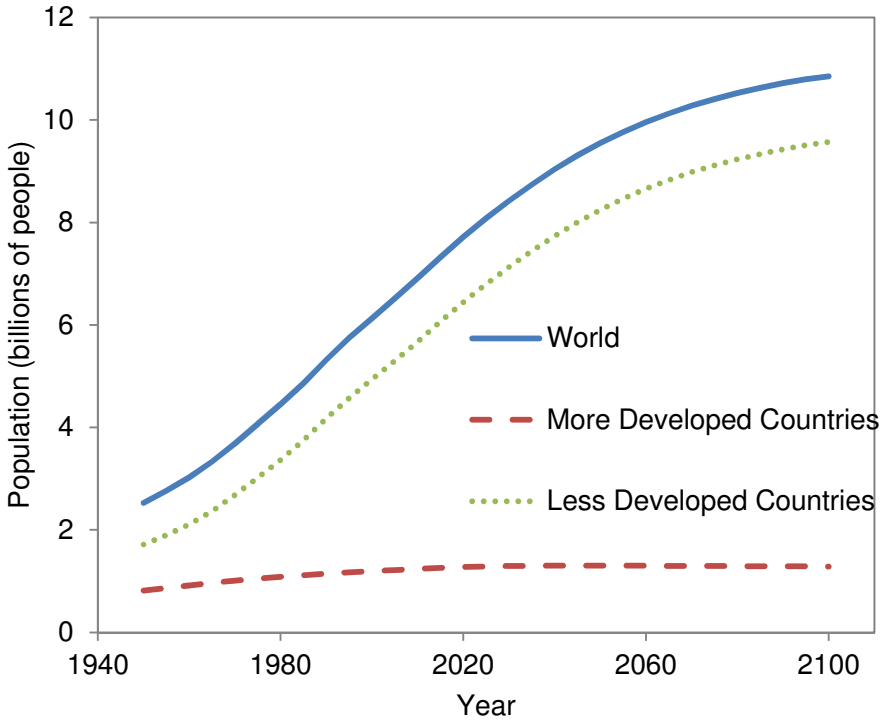

Figure 1.1: Population growth and projections. More developed countries include those in Europe, North America, Australia/New Zealand, and Japan. Less developed countries include those in Africa, Asia (excluding Japan), Latin America, the Caribbean, Melanesia, Micronesia and Polynesia (UN, 2012).

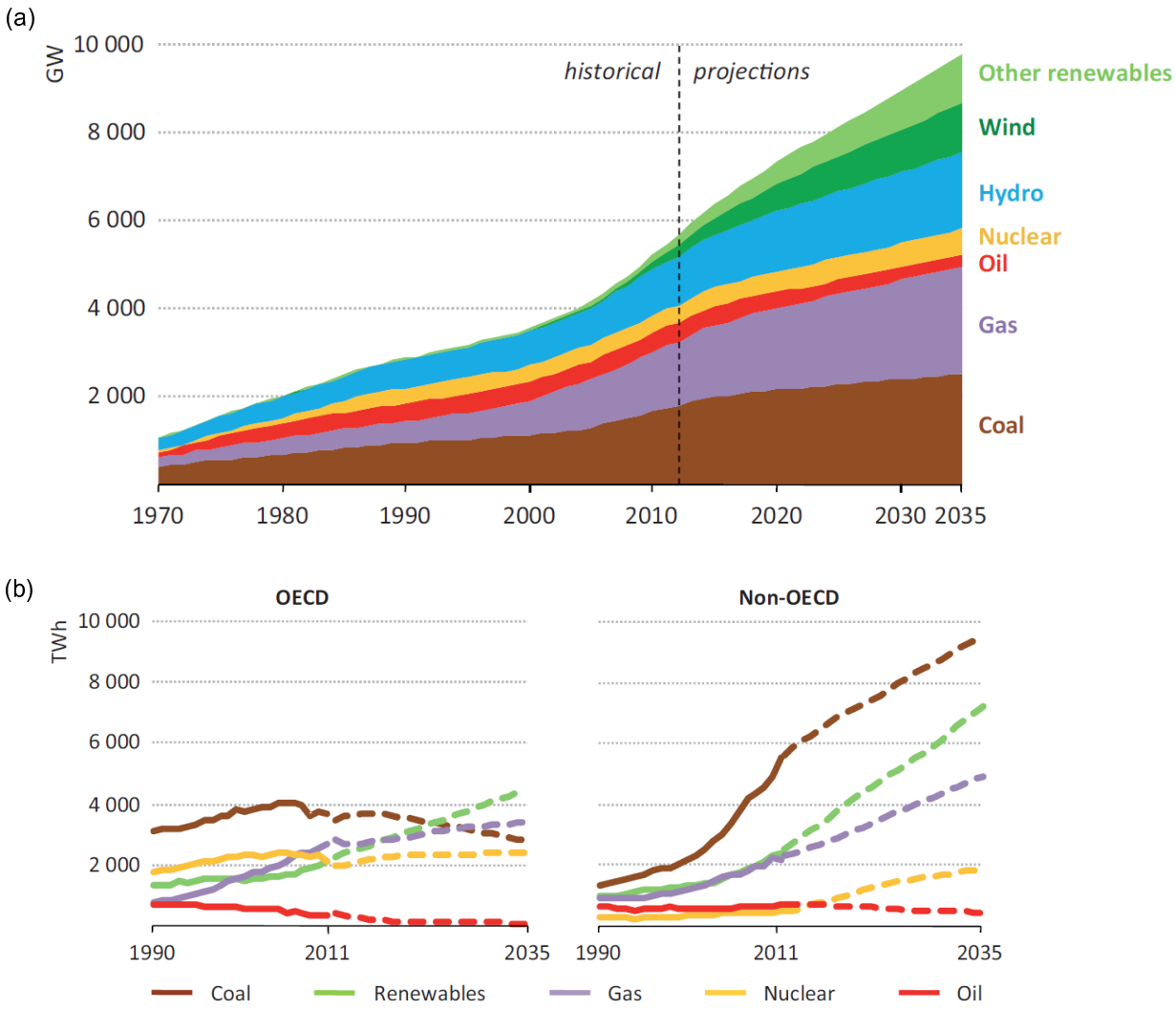

Figure 1.2: Historical and projected worldwide (a) installed energy capacity differentiated by energy source and (b) electricity generation differentiated by level of economic development and energy source (IEA, 2013).

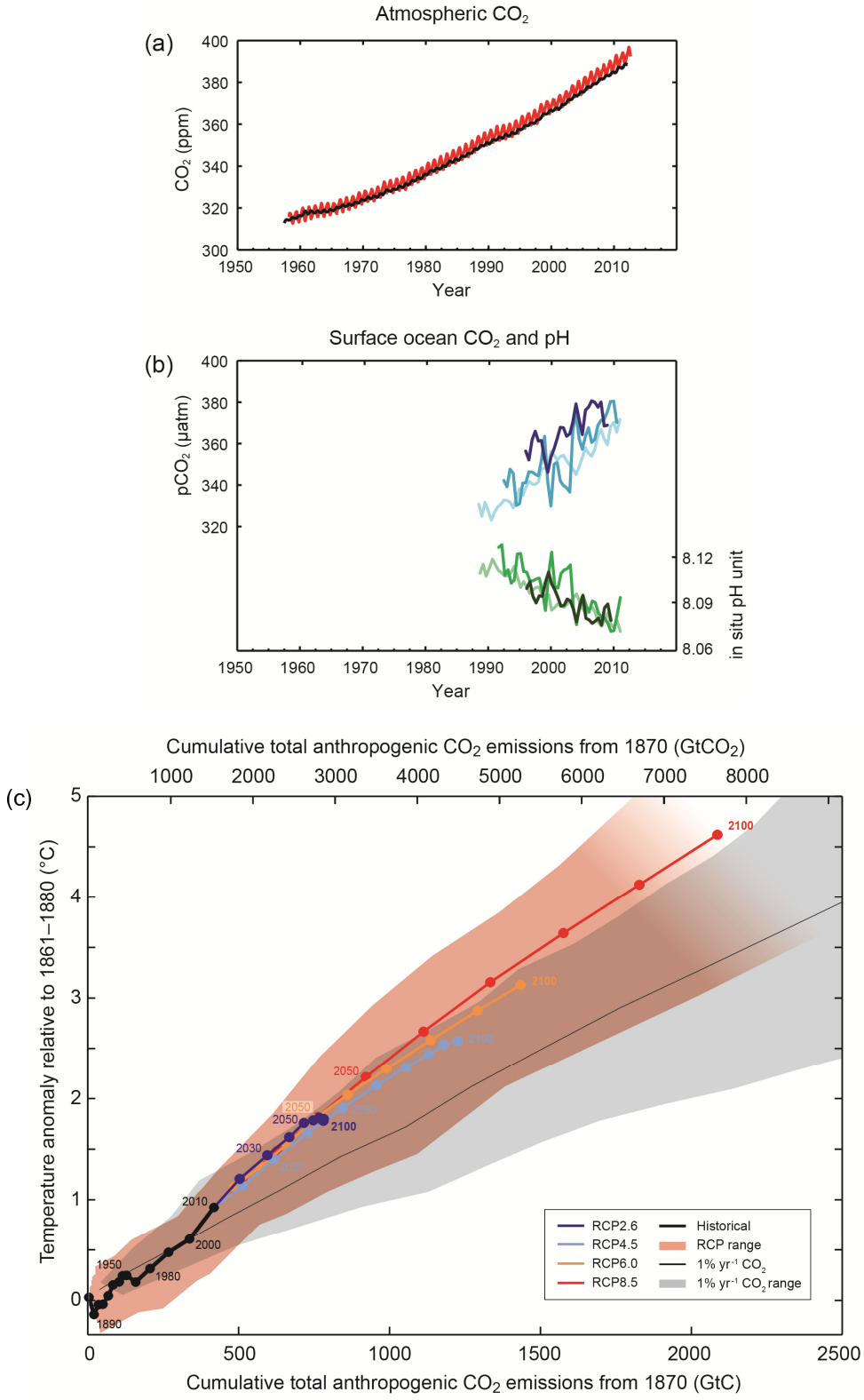

Figure 1.3: Graphs: (a) Atmospheric CO_2 concentration rise over the past 50 years, (b) CO_2 concentration in ocean and effect on pH, and (c) correlation between temperature anomaly and cumulative CO_2 emissions (IPCC, 2013).

2. Background

2.1. Conventional Methods of Carbon Capture and Storage (CCS)

Largely, the CCS field has split its efforts into research on CO_2 separation and CO_2 storage. Once separated—or captured—the highly pure CO_2 stream is pressurized and transported to a storage site. The state of art capture technology is a temperature swing utilizing an aqueous amine solvent, specifically up to 30 wt% monoethanolamine (MEA) in water, which reversibly binds CO_2. Conventional practices aim to pair MEA scrubbing of CO_2 with geological storage by injection into an underground reservoir. Though the capture technology is demonstrated on large scales (Rochelle, 2009), amine-based CO_2 scrubbing still faces challenges, namely the energy penalty associated with looping large water quantities since the corrosive MEA must be present in a dilute aqueous solution as well as its own thermal degradation over time. Furthermore, this technique separates CO_2 at low temperature (below 100 °C) and would not support the integration of CO_2 within a high temperature energy conversion system.

Many other technologies are under development, like advanced membranes, zeolites, and chemical looping schemes, and some are capable of operating at high temperature. For example, the Zero Emission Coal Alliance (ZECA) process and some chemical looping technologies capture CO_2 by reaction with a metal oxide (Feng *et al.*, 2007). The metal is typically calcium (Ca), usually in the form of calcium hydroxide ($Ca(OH)_2$) or calcium oxide (CaO). Ca-based sorbents have demonstrated much success as carbon capture media, providing significant carbonation reaction kinetics as well as overall conversion (Feng *et al.*, 2007). Beyond their optimal reaction characteristics, Ca-based

sorbents are attractive as they are derived from inexpensive materials like limestone. These resources are all carbonate minerals (fast Ca carbonation kinetics led to the natural widespread existence of calcium carbonates), and therefore the production of the sorbent requires the release of a mole of CO_2 for each mole of sorbent manufactured, at least. To justify their use in a CCS scenario, the sorbents must be regenerated and looped, requiring significant energy and cost especially when considering sorbent degradation (Dasgupta *et al.*, 2008; Senthoorselvan *et al.*, 2009). The enormous energy penalty lies in the stability of the carbonate species, requiring temperatures over 800 °C to liberate the CO_2.

As mentioned, conventional CCS is dependent on long term geological storage (see overview in Figure 2.1). Independent of capture technology, CO_2 is compressed and transported to suitable reservoirs including depleted oil and gas fields, on and offshore subsurface saline formations. The CO_2 can also provide added benefit in the cases of enhanced oil recovery, where CO_2 is injected into poorly producing oil wells to reduce the fluid viscosity while maintaining the pressure in the reservoir, and enhanced coal bed methane recovery operations. These beneficial scenarios do not present a long term solution to the ever increasing amounts of CO_2 entering the atmosphere. Ultimately, geological storage is far from being accepted as a foolproof CO_2 storage solution. The hurdles involve societal issues of public perception (not wanting the CO_2 pumped beneath your home, city, etc.) and continued scientific inquiries into the fate of geologically stored CO_2 as well as methods for accounting for stored CO_2. Depending on the mineral formation at the injection site, chemical reactions between the mineral

components and CO_2 can result in trapping mechanisms where the CO_2 is immobilized in a safe and permanent solid mineral carbonate.

2.2. Carbon Mineralization as a Carbon Capture and Storage Process

Most magnesium within the Earth's crust is contained in minerals other than carbonates. Thus, the conversion of Mg-bearing minerals to carbonates represents a CCS scenario capable of combining CO_2 capture with storage (IPCC, 2005). The process by which minerals form carbonates is called carbon mineralization or weathering, and generally it occurs on geological timescales. A generalized representation of a process for CO_2 capture and storage by mineralization is depicted in Figure 2.2. Industrial wastes or mined sorbent materials containing metal oxide/hydroxide compounds react with concentrated CO_2 to form highly stable carbonate minerals, e.g. Equation 2.1 or Equation 2.2 (Q is a divalent metal like Mg or Ca). The produced solids can be returned to the mine, re-used as a construction aggregate material, or safely disposed of in a landfill.

Equation 2.1: $QO_{(s)} + CO_{2(g)} \rightarrow QCO_{3(s)} + \text{heat}$

Equation 2.2: $Q(OH)_{2(s)} + CO_{2(g)} \rightarrow QCO_{3(s)} + H_2O_{(g)} + \text{heat}$

Suitable Mg-bearing minerals (e.g. olivine and serpentines) are in abundance around the world, with a capacity that far exceeds the total CO_2 which could be liberated by burning through our fossilize carbon fuel reserves (Lackner *et al.*, 1995). Storage of CO_2 in the mineral carbonate matrix is advantageous from permanence and safety standpoints. Carbonation reduces the thermodynamic free energy of carbon significantly, see Figure 2.3. Furthermore, the carbonation reaction is exothermic, releasing just over 100 kJ per

mole in the reaction of MgO with CO_2 to form $MgCO_3$. The stability of mineralized carbon enables the opportunity to dismiss long-term monitoring of the CO_2 as will likely be needed in mass adoption of geological storage.

Carbon mineralization does have its share of drawbacks. Most notably, weathering processes occur on geological timescales. Much of the technological development in this field focuses on improving the carbonation rates. Direct gas-solid carbonation of the minerals is not feasible. Research has focused on aqueous processes involving the enhancement of silicate mineral dissolution (Equation 2.3), CO_2 dissolution and hydration (Equation 2.4 and Equation 2.5), and carbonation reactions (Equation 2.6) in standalone modes as well as integrated (Park & Fan, 2004).

Equation 2.3: $Mg_3Si_2O_5(OH)_4(s) + 6H^+ = 3Mg^{2+} + 2Si(OH)_4 + H_2O$

Equation 2.4: $CO_2(g) = CO_2(aq)$

Equation 2.5: $CO_2(aq) + H_2O = H_2CO_3(aq) = HCO_3^- + H^+ = CO_3^{2-} + H^+$

Equation 2.6: $Mg^{2+} + CO_3^{2-} = MgCO_3(s)$

The pH swing from low pH (dissolution) to high pH (carbonation) results in the conversion of silicate mineral to precipitated magnesium carbonate (PMC). Depending on the reaction conditions, the PMC may come in the anhydrous form presented in Equation 2.6 or may come in a hydrated form (to be explored more fully in a subsequent chapter). CCS via aqueous carbonation of silicate minerals has been investigated in our research group and elsewhere (O'Connor *et al.*, 2004; IPCC, 2005; Gadikota *et al.*, 2014). Because the mineralization reactions have been performed in aqueous phase, their

application has generally been limited to relatively low reaction temperatures. Thus, the following study focused on the carbonation of a specific magnesium species, magnesium hydroxide ($Mg(OH)_2$), to explore the carbonation at higher temperatures consistent with various energy conversion processes.

2.3. $Mg(OH)_2$ as Carbon Capture and Storage Sorbent Material

As given in Figure 2.4, an adaptation of a pH swing process for carbonating magnesium silicate minerals outlined in the previous section, $Mg(OH)_2$ can be produced instead of $MgCO_3$ by raising the pH without introducing CO_2 (Park, 2005). The solid $Mg(OH)_2$ sorbent material can capture CO_2 via the following gas-solid reactions, which can occur at high temperatures (as long as they are below the decomposition temperature of $MgCO_3$).

Equation 2.7: $Mg(OH)_2(s) = MgO(s) + H_2O(g)$ $\Delta H° = 81.2$ kJ/mol

Equation 2.8: $MgO(s) + CO_2(g) = MgCO_3(s)$ $\Delta H° = -100.9$ kJ/mol

The overall gas-solid reaction becomes:

Equation 2.9: $Mg(OH)_2(s) + CO_2(g) = MgCO_3(s) + H_2O(g)$

$\Delta H° = -19.7$ kJ/mol

Mg-based sorbents derived from silicate minerals for gas-solid carbonation applications have seen less research interest than their calcium counterparts. The reaction kinetics are slower, though reactivity can be improved through optimization of the sorbent characteristics and reaction conditions (Butt *et al.*, 1996; Goff & Lackner, 1998; Béarat *et al.*, 2002; Lin *et al.*, 2008; Zevenhoven *et al.*, 2008; Fagerlund *et al.*, 2010; Fagerlund & Zevenhoven, 2011). Comparatively, MgO carbonation occurs at a much slower rate than $Mg(OH)_2$ carbonation. The kinetics are such that MgO is unreactive at

low CO_2 partial pressure (Béarat *et al.*, 2002; Zevenhoven *et al.*, 2008; Fricker & Park, 2013). Because of this discrepancy, and the fact that both dehydroxylation (Equation 2.7) and carbonation (Equation 2.8) reactions occur in the same temperature range, control over dehydroxylation can be crucial. Another complication with $Mg(OH)_2$ carbonation, and similar gas-solid reactions, is the formation of a diffusion resistant passivation layer as carbonation proceeds. The formation of the passivation layer limits overall conversion by effectively reducing the quantity of reactive sorbent material (Butt *et al.*, 1996).

Pressurization can increase reaction kinetics and overall conversion due to the higher carbonation rates. Increasing P_{CO2} allows the increasing the reaction temperature, because at larger P_{CO2}, the $MgCO_3$ is stable to higher temperature (Figure 2.5). For example, conversions as high as 60% were reported at CO_2 pressures in the range of 40-45 bar at a critical reaction temperature just below the stability of $MgCO_3$ (Zevenhoven *et al.*, 2008). When P_{CO2} was increased much further, at the same critical temperature, a suppressive effect was observed (Béarat *et al.*, 2002). Control over reaction conditions can yeild high conversions. Moreover, reaction engineering can increase kinetics and yeild. A pressurized fluidized bed showed enhanced reaction rate, attributed mainly due to the attrition of sorbent particles resuloting in the loss and entrainment of the carbonated particle portions (Fagerlund *et al.*, 2010). As of now, fundamental mechanistic analysis of the reaction system under continued development.

Another technique to enhance carbonation rates and conversion involves H_2O. An enhanced effect of water on carbonation was exhibited under wide ranging experimental conditions by numerous comparable materials, such as Mg and Ca oxides, hydroxides, and raw minerals (Shih *et al.*, 1999; Beruto & Botter, 2000; Kwak *et al.*, 2010; Kwak *et*

al., 2011; Schaef *et al.*, 2011; Torres-Rodríguez & Pfeiffer, 2011; Larachi *et al.*, 2012; Loring *et al.*, 2012). The presence of H_2O may inhibit dehydroxylation, thus preventing the formation of unreactive MgO (Fagerlund *et al.*, 2011). Bearing in mind the fast carbonation of $Mg(OH)_2$ in the slurry phase (Botha & Strydom, 2001; Park *et al.*, 2003; Zhao *et al.*, 2010; Hövelmann *et al.*, 2012; Harrison *et al.*, 2013), the involvement of H_2O could facilitate an entirely different reaction mechanism.

The enhanced effect of H_2O and unavoidable limitations observed during the gas-solid carbonation of $Mg(OH)_2$ (Fricker & Park, 2013), guided the return to an aqueous system, albeit at higher temperatures than previously studied in the literature ($30 < T < 200$ °C). Instead of producing dry $Mg(OH)_2$ in the schematic of Figure 2.4, a slurry could be recovered and used directly depending on the application. Mechanistically, in heavily hydrated systems (slurry phase carbonation), the carbonation reaction was found to proceed via a homogeneous precipitation reaction between dissolved Mg^{2+} and CO_3^{2-} (Zhao *et al.*, 2010). In addition to Equation 2.6, which produces anhydrous $MgCO_3$ (also known as magnesite), other carbonation reactions can occur, especially in hydrated systems. Various metastable phases are known to form, of which the most prevalent are nesquehonite ($MgCO_3 \cdot 3H_2O$) and hydromagnesite ($Mg_5(CO_3)_4(OH)_2 \cdot 4H_2O$) pruced according to Equation 2.10 and Equation 2.11 respectively.

Equation 2.10: $Mg^{2+} + CO_3^{2-} + 3H_2O = MgCO_3 \cdot 3H_2O(s)$

Equation 2.11: $5Mg^{2+} + 4CO_3^{2-} + 2OH^- + 4H_2O = Mg_5(CO_3)_4(OH)_2 \cdot 4H_2O(s)$

Despite magnesite being the most stable carbonate at all temperatures and CO_2 pressures (Kittrick & Peryea, 1986), the metastable hydrated carbonates form and persist

for long times under a wide range of conditions. Mg^{2+} is highly hydrated in solution, and therefore H_2O tends to be incorporated into the carbonate matrix (Sayles & Fyfe, 1973). Temperature's influence on the formation of metastable magnesium carbonates has been evaluated, and distinct phase boundaries were devised accordingly (Fricker & Park, 2014). Factors like aging time (metastability is ultimately is governed by kinetics) and the presence of other species in solution can affect the carbonate phase produced (Hänchen *et al.*, 2008). Generally, higher carbonation temperatures favor magnesite formation, though CO_2 solubility and relatedly $Mg(OH)_2$ dissolution are favored at lower temperatures (Park *et al.*, 2003). Other ways to stimulate magnesite formation at lesser conditions involve various solution additives such as salts to interfere with the Mg-water attraction (Sayles & Fyfe, 1973) or polymers to reduce water activity (Sandengen *et al.*, 2008).

Ultimately the metastable carbonates complicate the slurry phase $Mg(OH)_2$ system by reducing (1) carbonate stability and (2) process efficiency. The higher solubility of hydrated carbonates means that less carbonate is captured per input material and that the produced carbonates are more susceptible to dissolution/decomposition after CCS. Hydrated carbonates include crystallized water and hydroxide in some cases, which result in the inefficient utilization of Mg to store CO_2. Beyond process implications, metastability within the aqueous Mg carbonation field has led to confusion in the literature surrounding the interpretation of experimental results and conclusions (Swanson *et al.*, 2014). Seeding has been proposed to remedy the metastability issue, getting around slow nucleation and crystal growth rates of magnesite as compared with the hydrated carbonates. Magnesite nucleation has been observed to be temperamental, requiring a specific set of experimental conditions and supersaturation (Giammar *et al.*,

2005). Seeds have provided faster nucleation rates and shorter induction times in similar systems (Sheila & Khangaonkar, 1989; Giammar *et al.*, 2005), and in some case, precise morphological control was achieved through the use of seeds (Donnet *et al.*, 2005).

In all, the $Mg(OH)_2$ carbonation system is unexpectedly complex. In both gas-solid and slurry phase carbonation arrangements, various limitations exist, each with their own engineered solutions. A fundamental understanding of the carbonation mechanisms and phenomena is crucial to the development of this CCS technology and possible integration of said technology with an energy conversion system.

2.4. Potential for Integration of CCS with Energy Conversion Processes

A critical aspect of any CCS technology is in its integration with CO_2 production. Whereas many of the conventional CO_2 capture technologies focus on CO_2 separation from flue gas, carbon mineralization is suitable for process integration given the potential temperature ranges where the sorbents are stable. In fact, carbonation reactions are generally more favorable at higher temperatures. One potential arrangement could combine the water gas shift reaction (WGSR) (Equation 2.12) with carbon mineralization to capture CO_2 right where it is formed.

Equation 2.12: $CO(g) + H_2O(g) = CO_2(g) + H_2(g) \quad \Delta H° = -41.1$ kJ/mol

A number of energy conversion technologies, including the waste-to-fuel process mentioned herein, utilize the WGSR to tailor the syngas composition for specific applications. Despite its long industrial history, the WGSR is plagued by the competition between thermodynamics and kinetics. To overcome the kinetic limitations of the low-

temperature WGSR, large quantities of catalyst are employed in a two separate reactors, the high temperature shift (HTS) and low temperature shift (LTS), in series with inter-bed cooling (Lloyd *et al.*, 1989).

By capturing the CO_2 in the WGSR, H_2 production is enhanced via an equilibrium shift while the overall energy conversion process can be more sustainable. Previously, WGSR enhancement through carbon capture used a variety of materials including calcium oxide, hydrotalcite, and mixed metal oxides (Harrison, 2008), but in each case the sorbent acted only as a capture agent, meaning the separated CO_2 would still require an energy intensive release and subsequent storage solution. Figure 2.6 contains the results of a thermodynamic equilibrium model of the system, demonstrating effect of CO_2 removal (by MgO carbonation) on the equilibrium concentration of equimolar gaseous reactants ($P_{CO,i} = P_{H2O,i} = 10$ atm). Hydrogen production is sustained to nearly 100% conversion until the decomposition temperature of $MgCO_3$ is reached. Note that the decomposition temperature can be increased by increasing the P_{CO2} within the system. More details about the calculation can be found in Section 7.2.1. The benefit could extend as far as either eliminating the need for the larger and inherently more costly LTS reactor or reducing/changing the catalyst requirement. The energy conversion process could further benefit from the presence of basic sorbent materials as they would scrub for other acidic gases besides CO_2.

The enhanced WGSR system could complement a number of energy conversion systems which utilize synthesis gas (a mixture of CO and H_2, also called syngas) including advanced gasification power plants and processes for synthesizing a range of industrial chemicals and fuels. Generally, CO_2 is a byproduct of carboneous energy

conversion, and processes that produce chemicals and fuels are notoriously large emitters due to their intricate and energy intensive processing stages. Wastes, which contain vast embodied energy, are an especially appealing feedstock to such processes due to their low cost and potential for mitigation of waste management related issues. An overview schematic of a waste to chemical process can be found in Figure 2.7. Gasification can convert waste to syngas and after various gas cleanup and composition shifts, Fischer-Tropsch synthesis (FTS) technology can produce synthetic chemicals and liquid fuels that are easily incorporated the current chemical industry and fuel supply. The process would offset waste otherwise sent to be landfilled as well as reduce the amount of fossilized petroleum mobilized. Of the waste that enters a landfill, approximately 17.6% (28.9 million tons) is composed of plastics that were produced directly from petroleum. Only around 30% of plastics are recovered and recycled (EPA, 2012).

Liquid fuel, in particular, powers the transportation of the Earth's people and goods. Research in synthetic fuel production is currently focused on the biochemical conversion of biomass to ethanol and biodiesel. Such technology cannot fulfill the large-scale demands for liquid fuel since they must compete with agriculture for necessary land. Instead, the combined CCS scheme studied herein aims to integrate with the thermochemical process by which certain municipal solid wastes (MSW) can be converted to synthetic fuel. Another ancillary benefit of synthetic fuels is the reduction in mobilization of fossilized carbon. Despite the benefits associated with the conversion of waste into liquid fuels, processes that produce fuels from coal, which is similar in carbon and energy content to non-recyclable plastic waste, have nearly double the carbon footprint as compared with traditional refining of petroleum (Schrag, 2009). Because of

the high footprint, and the fact that gasification and FTS are mature technologies, the following dissertation focused on understanding the fundamentals of the CCS technology and investigated its integration with the WGSR.

2.5. Research Objectives

2.5.1. Problem Statement

The ultimate objective of this research project is to provide a comprehensive scientific understanding of the fundamentals related to a combined CO_2 capture and storage technology utilizing $Mg(OH)_2$-based sorbent materials. Its place within a broader sustainable energy conversion system that could convert wastes to value-added chemicals and fuels is considered. Gasification of solid carboneous materials and FTS processes have been studied extensively in the past and are known for their large carbon footprint; therefore, the dissertation focuses on understanding the combined carbon capture and storage step where CO_2 reacts with $Mg(OH)_2$ in gas-solid or slurry phase carbonation reactions. Carbon mineralization occurs naturally over geological timescales. Even in engineered scenarios, carbonation of magnesium-based sorbents experiences limitations with respect to kinetics and overall conversion. Moreover, the mechanisms and fundamental chemistry of the Mg carbonation reactions is not very well understood.

2.5.2. Scientific Questions

The key scientific and engineering questions to be addressed by this research are:

- Is gas-solid carbonation of $Mg(OH)_2$ feasible at low pressure?

- Does the presence of steam influence or enhance the gas-solid carbonation of $Mg(OH)_2$?
- Is it possible to synthesize anhydrous $MgCO_3$ quickly and under reasonable conditions when carbonating $Mg(OH)_2$ in the slurry phase?
- What are the optimum conditions for the carbonation of $Mg(OH)_2$?
- How does the carbonation mechanism of $Mg(OH)_2$ change under various carbonation conditions?
- Will a $Mg(OH)_2$-based sorbent enhance the WGSR by shifting its equilibrium while fixing gaseous CO_2 into a thermodynamically stable solid?
- What considerations are necessary for integrating the combined CCS process and an advanced energy conversion system?
- What would be the net environmental benefit of integrating in-situ CO_2 capture and storage?

2.5.3. Research Goals

The goals of this research are outlined below:

- Perspective within an Energy Conversion System: Consider the placement of an $Mg(OH)_2$ carbonation process within an overall energy conversion system. Qualify the potential environmental impact.
- Gas-solid $Mg(OH)_2$ Carbonation Studies: Investigate reaction pathways of $Mg(OH)_2$ carbonation at low and high pressure in gas-solid arrangement. Study

the influence of H_2O on carbonation pathways. Conduct systematic solid product analyses. Create phase diagram for the MgO-H_2O-CO_2 system.

- Slurry Phase $Mg(OH)_2$ Carbonation Studies: Probe the carbonation of $Mg(OH)_2$ in a heavily hydrated environment. Determine the important parameter(s) which determine the carbonate phase produced. Examine the kinetics and mechanism of producing various carbonate phases. Explore methods for promoting anhydrous carbonate formation at conditions where it is otherwise unfavorable.
- Direct the Precipitation of Anhydrous Magnesium Carbonate: Test the hypothesis that precipitation of a specific phase within the slurry carbonation system can be accomplished with seeding. Evaluate the mechanism for seeded carbonation. Assess the potential to seed for anhydrous production at low temperatures.
- Studies on the Integration of Carbonation with WGSR Studies: Perform WGSR in the headspace of the aqueous carbonation reactor. Evaluate the effect of both catalyst and slurry on WGSR. Explore the phenomena occurring in this complex, multiphase reaction system.

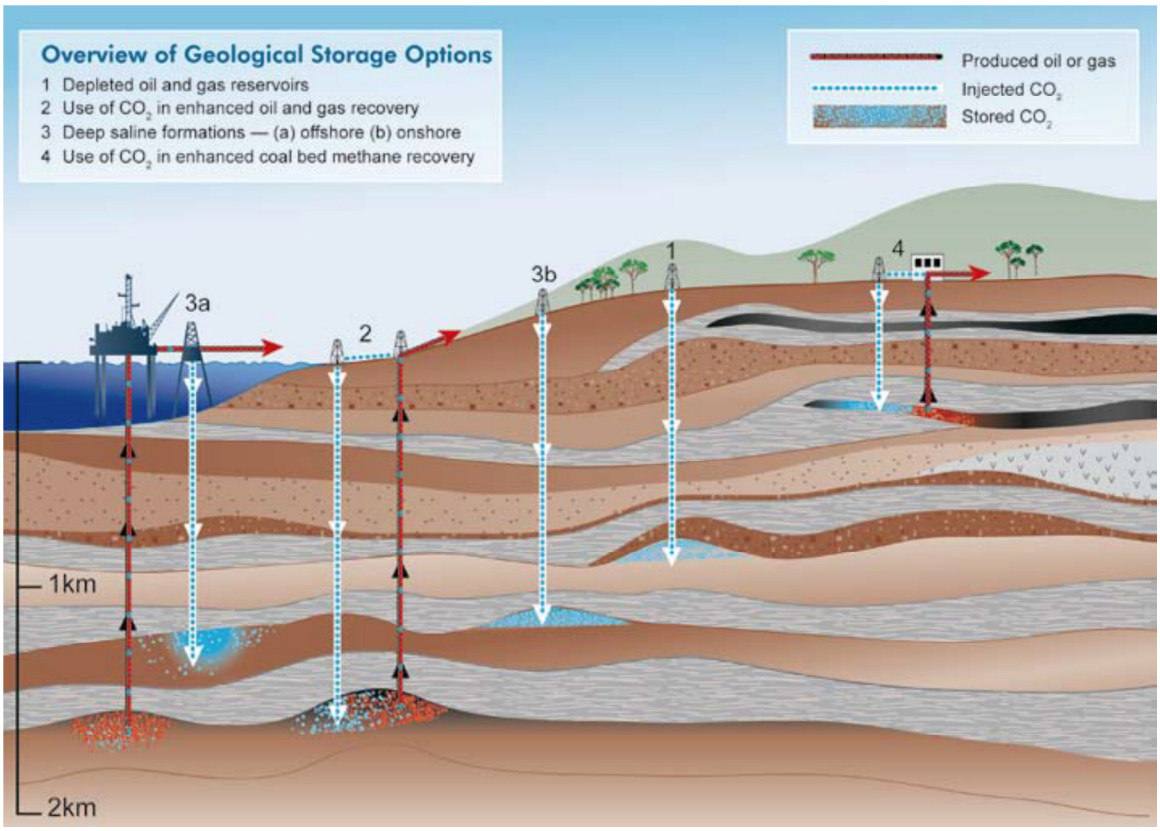

Figure 2.1: Overview of methods for the geological storage of carbon dioxide within subsurface reservoirs (IPCC, 2005).

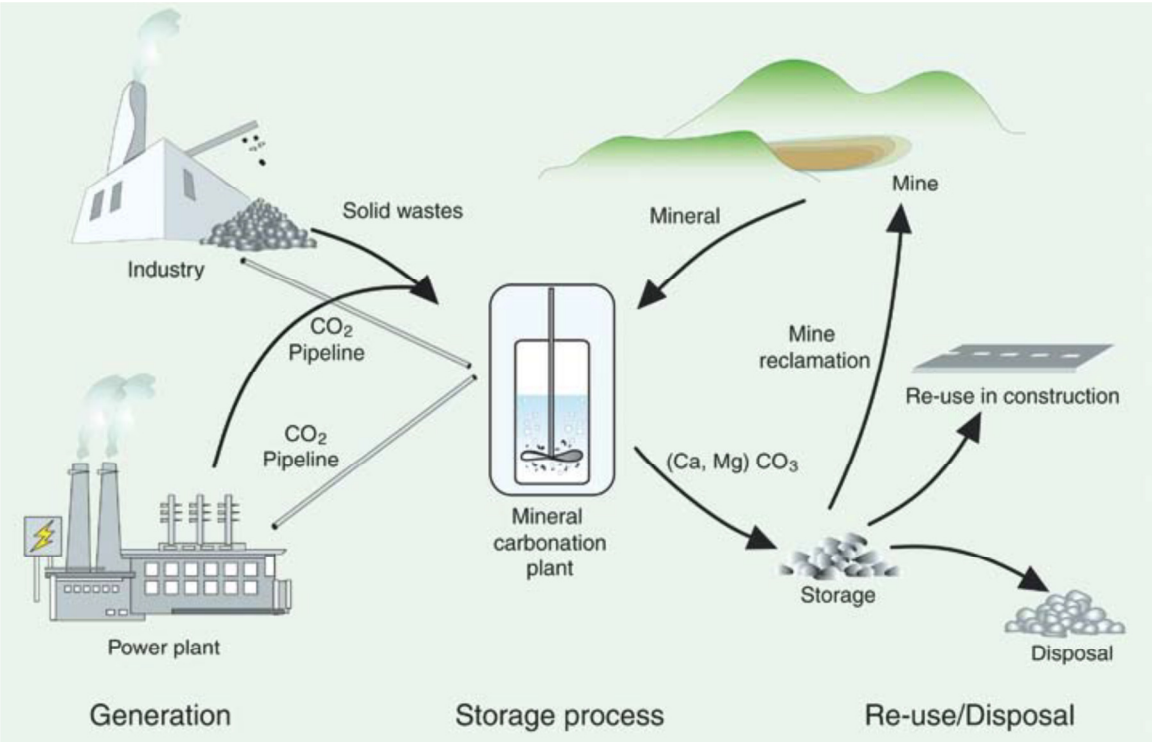

Figure 2.2: General schematic for capturing carbon dioxide from point sources by a mineral carbonation process (IPCC, 2005).

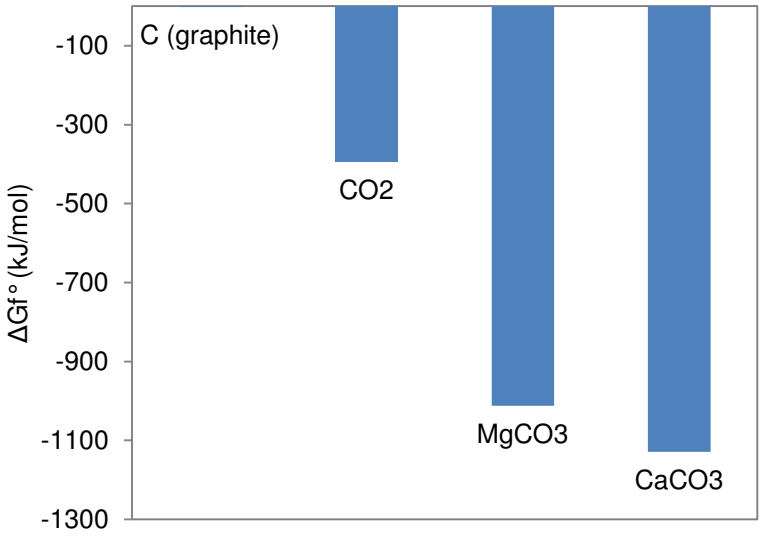

Figure 2.3: Free energy of select carbon-containing compounds.

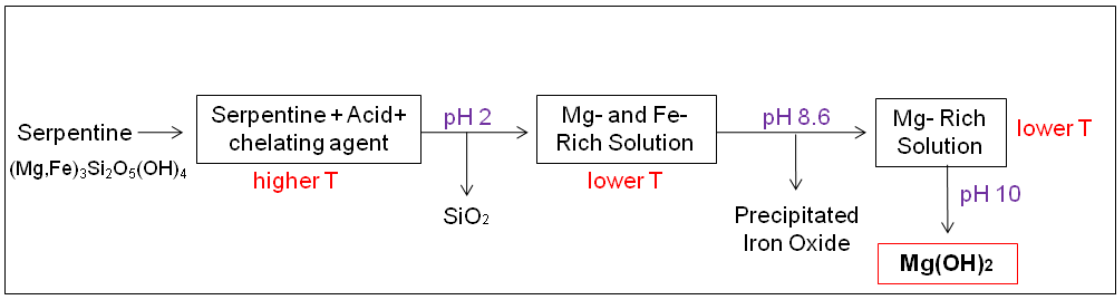

Figure 2.4: Schematic of $Mg(OH)_2$ sorbent production from Serpentine via a modified pH swing process (Park, 2005).

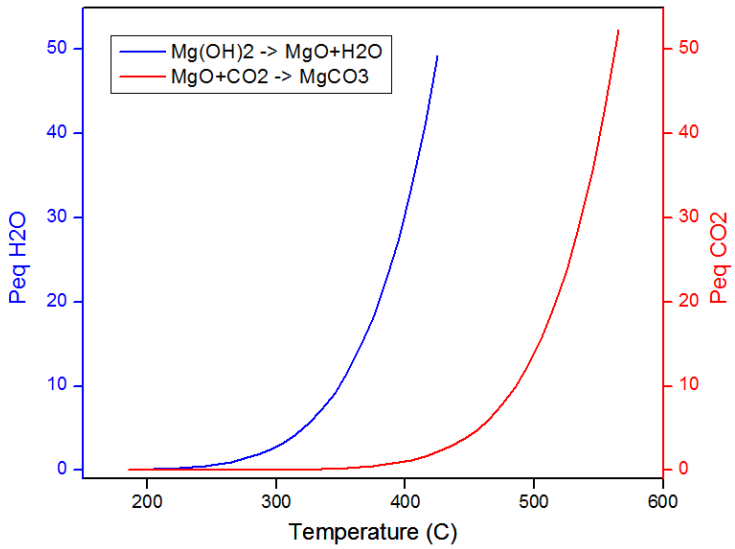

Figure 2.5: Equilibrium pressures (in atm) of dehydroxylation and carbonation reactions at different temperatures.

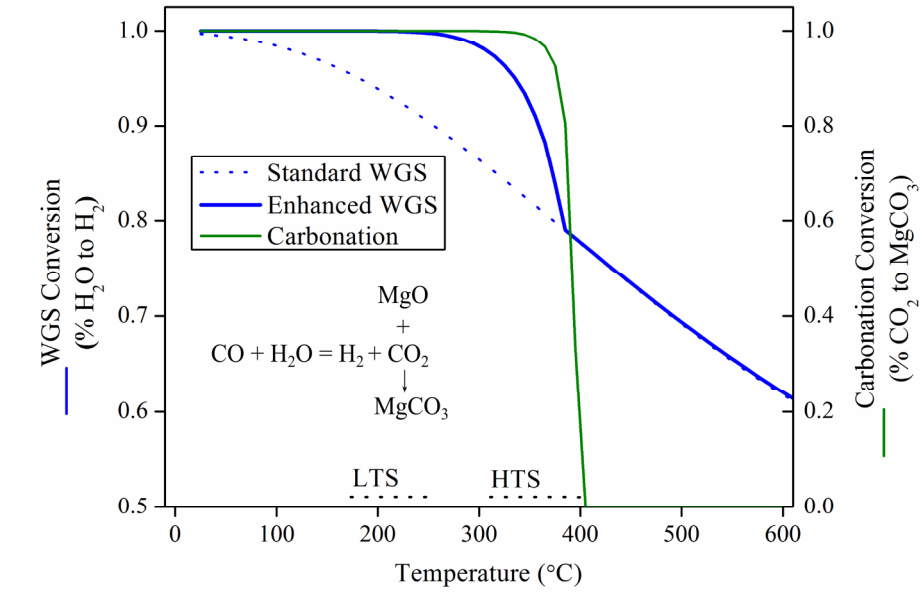

Figure 2.6: Thermodynamic model shows effect of MgO carbonation on the equilibrium WGSR conversion. Equilibrium constants generated with HSC Chemistry and NIST Chemistry WebBook (NIST; Outotec). $P_{o,H2O} = P_{o,CO} = 10$ atm.

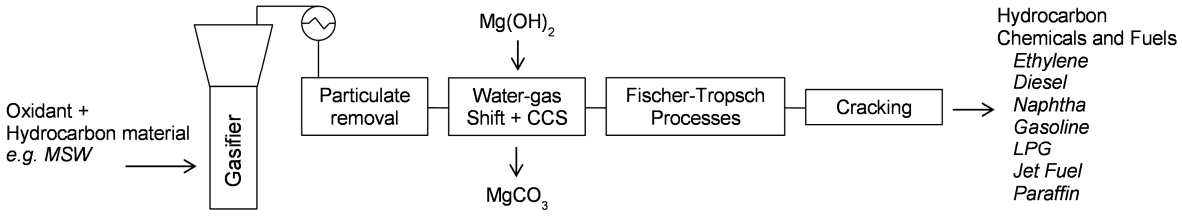

Figure 2.7: Simplified schematic of a thermochemical waste-to-fuel conversion process.

3. Perspective: Waste-to-Energy with integrated CCS Scheme

3.1. Introduction

The pursuit of sustainable energy solutions in a world still dominated by carboneous energy sources led to the application of CCS to energy conversion systems. As introduced in the previous Chapter, the goal of the following study aimed to develop an understanding of the fundamentals of carbon dioxide capture by a $Mg(OH)_2$ sorbent in order to ultimately integrate the carbonation reaction with a CO_2 source, the WGSR. Increasing the scale beyond the CCS and WGSR integrated process reveals a complex overall system that (1) produces the WGSR reactants, CO and H_2O, from the gasification of carboneous materials and generation of steam and (2) produces a range of synthetic fuels and chemicals from shifted, decarbonized syngas, which is generally a mixture of H_2 and CO gas (depicted in Figure 2.7). The following literature studies on the gasification of waste, process integration, product utilization, and life cycle comparison with an alternative waste energy recovery method (incineration) provide perspective around CCS's place within complex energy infrastructure.

3.2. Gasification Literature Study

KJF and Mr. Nabil Ashraf Sisani collaborated on the following section. A version was included in Mr. Sisani's M.S. thesis.

Gasification is a thermochemical process that converts carboneous material to syngas which can be subsequently used in power generation or chemical/liquid fuel synthesis. During gasification numerous chemical phenomena occur concurrently. Partial oxidation

is most dominant and is responsible for producing the syngas, yet pyrolysis and hydrogenation are also occurring. The process is very flexible in its feedstock—any carbon containing material can be gasified including large fractions of MSW. The products can generally be classified as main products (CO, H_2, CO_2, H_2O, CH_4, and other hydrocarbons), residues (tar, char, and ash), and troublesome emissions (HCl, NH_3, sulfur species). The products will vary greatly with feedstock, and the syngas can be further adjusted through manipulation of operating conditions and downstream gas treatment (Higman & van der Burgt, 2008; Yung *et al.*, 2009).

MSW as a feedstock for gasification presents a great opportunity to both reduce the amount of waste currently landfilled while also offset energy otherwise derived from nonrenewable sources. Of the 251 million tons of MSW Americans generated in 2012, 87 million tons, or 35%, was recovered for recycling or composting (EPA, 2012). While some materials do see a very high recycling rate (e.g. lead acid batteries at 96% recovery), others are far lower. Plastics, which embody significant energy as they were synthesized from petroleum, are only recovered at a rate of 30.8% and 28.2% for PET bottles/jars and HDPE bottles respectively (EPA, 2012). A quick calculation using the weight of plastics discarded (28.95 million tons), recycling rate (assume 30%), and energy density (assume 40 MJ/kg) reveals the energy embodied within that waste stream alone to be over 700,000 TJ.

Despite the benefits, thermochemical processing of MSW is challenged by its heterogeneity and emissions. Non-recyclable plastic waste and MSW, in general, is a heterogeneous mixture that varies by location among other factors. Different mixtures of petrochemical waste will produce varying syngas compositions and may require different

operating conditions to optimize the reaction. The ratio of CO to H_2 should vary as well as the amounts of other compounds that may evolve during heat treatment. Furthermore, potentially troublesome emissions, such as acidic gases, volatile organic compounds, aromatics, etc., may need special treatment as to be safe for both the atmosphere and downstream catalysts necessary for synthetic fuel processing. The following gasification characterization study focused on the effect of feedstock variation on syngas composition and solid residue characteristics.

3.2.1. Effect of Feedstock Size

A survey of literature revealed a wide variety of gasification feedstock, from biomass to coal, plastics, rubber, and other MSW components (Borgianni *et al.*, 2002; Pinto *et al.*, 2002; Aznar *et al.*, 2006; Jeon *et al.*, 2007; He *et al.*, 2009; Tsuji & Hatayama, 2009; Mastellone *et al.*, 2010; Zhao *et al.*, 2010; Ahmed *et al.*, 2011). Typically, particle sizes ranged from micrometers to millimeters. The relationship between particle size and char/tar residue production is most interesting from a process standpoint. Generally, larger feedstock particles resulted in greater amounts of char and tar. As with many gasification parameters, the effect is specific to each gasification system and must be studied as such. The monetary and energy cost to shred to smaller sizes should be considered. At the other extreme, with very small particles, new problems of entrained ash and potentially unreacted feedstock can occur.

3.2.2. Effect of Catalyst

Tar formation represents a huge problem in gasification systems. Beyond reducing the gas yield, tar tends to accumulate and cause substantial issue with reactor equipment. Including metal oxides as part of the feedstock blend has been shown to influence tar

formation reactions by weakening the C-C bond and lowering the tar pyrolysis reaction activation energy (Boxiong *et al.*, 2006). Numerous examples exist in the literature of the tar reducing capabilities of alkali and alkaline, oxides, salts, and minerals including CaO, MgO, SiO_2, NiO, Al_2O_3, Na_2CO_3, dolomite, and olivine. Dolomite was seen as a leading catalyst option due to its high activity for tar decomposition in the appropriate temperature range of 850-950 °C (He *et al.*, 2009). Some catalysts offer an added benefit of scrubbing other gaseous compounds. For example, CaO can remove gaseous sulfur from the gasifier.

3.2.3. Effect of Temperature

In general, increased gasification temperatures enhance syngas yield and carbon conversion (defined as ratio of carbon in produced gas to that of feedstock). The enhanced gas yield was related to the decomposition of tar. An upper limit does exist, since it requires energy to achieve and maintain the high temperature. Furthermore, gasification at high temperatures yielded syngas with a lower heating value (Pinto *et al.*, 2002). The reduced heating value was caused by the decomposition of methane and other gaseous hydrocarbons at elevated temperature. Depending on the application, these species may or may not be desired.

3.2.4. Effect of Steam

Along with air, oxygen, and nitrogen, steam is widely used as a gasifying agent. Compared against nitrogen and air, steam has been found to increase the volumes of produced gases during MSW gasification (Zhao *et al.*, 2010), likely due to the WGSR and tar reforming reactions (Pinto *et al.*, 2002). Gasification with steam tended to yield

larger hydrogen amounts due to the WGSR. The energy and cost of delivering steam to the gasifier should be considered when optimizing a gasification system.

3.2.5. Effect of Equivalence Ratio

Equivalence ratio (ER) is the ratio of the available oxygen to that of complete combustion when oxidizing with air. Increasing ER translates to delivering more oxygen, and therefore reduces tar/char formation and accumulation. However, the produced gas will have a lower heating value due to the combustion of hydrocarbon gases. Again, the ER must be determined based on the downstream syngas application. If the gas is to be sent to a turbine for combustion, a higher heating value is desired and thus a lower gasification ER would be optimal. The opposite is true if a clean syngas is required for fuel synthesis.

3.2.6. Summary

The findings of the literature survey are included in Table 3.1. The independent parameters with the largest influence on gasification outcome included the temperature, presence and type of catalyst, use of steam, and gasification feedstock. ER, steam/MSW ratio and reactor residence time had less effect comparatively. In each case, the addition of plastic was shown to enhance gasification, though if plastic addition was too large the syngas yield could be diminished due to the difficulties with reactivity. A summary of the optimum values for certain parameters is included in Table 3.2. An examination of the literature revealed a high degree of variability in both inputs and outputs of the gasification system. Gasification is a highly complex chemical process with many knobs to turn. The literature studies exposed trends between independent and dependent

parameters, and from those relationships guidelines and strict rules can be developed for specific systems.

3.3. Product Utilization

3.3.1. Downstream Chemical and Fuel Synthesis

A Fischer-Tropsch Synthesis (FTS) reactor system could follow gasification and WGSR process for producing shifted syngas from waste plastic. The overall FTS reaction is represented by Equation 3.1. The Anderson-Schulz-Flory (ASF) polymerization model predicts the distribution of alkane chain products ranging from C_1 to C_{50}. The process was developed early in the 20th century, yet catalysts are under continued development to better select the desired product range. The methane produced during FTS, usually larger quantities than predicted by the ASF model, can be used to generate electricity or heat and improve the overall process efficiency (Huber *et al.*, 2006).

Equation 3.1: $n\mathrm{CO} + (2\mathrm{n}+1)\mathrm{H_2} \rightarrow \mathrm{C}_n\mathrm{H}_{(2n+2)} + n\mathrm{H_2O}$

The products of FTS are either olefin- or paraffin-rich depending on the operating conditions and the catalyst choice. Long carbon chained paraffin products (C_{12}-C_{19}) form at low reaction temperatures and produce F-T waxes and synthetic diesel fuel. The shorter carbon chain olefins (C_5-C_{10}) occur at high reaction temperatures and can be further processed to make gasoline and other chemicals (Höök & Aleklett, 2009).

Generally, group VIII transition metals have been used as FTS catalysts. Iron is desired for its low cost and performs better at higher temperatures. Iron is also the most active of the typical FTS catalysts with respect to the WGSR. Cobalt is widely used, providing the best yields over the longest lifetimes. Ruthenium has very significant catalytic activity in gas liquefaction at low to moderate temperatures and pressures, though it is cost prohibitive in many applications. In most cases, the catalyst is promoted by also containing alkali species which improve electron transport (Van Der Laan & Beenackers, 1999).

3.3.2. Use of Carbonated Solids

Beyond the potential of carbon mineralization to safely and permanently store all the CO_2 generated from now and into the future (it is estimated that carbonate storage could total more than 10,000-1,000,000 Gt of total carbon (Sanna *et al.*, 2012)), another advantage lies in the opportunity to utilize the product to add overall process value. The solid carbonates are suitable candidates as construction materials. Though certainly unable contain our entire carbon emissions in construction materials, simply exchanging 10% of current building materials with recovered carbonates could result in a 1.6 Gt/year reduction in CO_2 emissions (Sridhar & Hill, 2011). The ability to tailor the carbonation processing to produce desired products is under continued development (Zhao *et al.*, 2010; Zhao *et al.*, 2013; Fricker & Park, 2014; Gadikota *et al.*, 2014; Gadikota *et al.*, 2014). If carbon mineralization was to dominate the CCS sector, the majority of recovered carbonates would need to be disposed of by landfilling or mine reclaiming. Still, the thermodynamic stability of the carbonates provides significantly lower risk than geological storage options.

3.4. Life Cycle Analysis Perspective

The life cycle assessment (LCA) of waste plastics treated by a gasification-Fischer-Tropsch (GFT) process or incineration was completed to compare associated greenhouse gas emissions. The scope, depicted in Figure 3.1, defined which emissions contribute to the overall process footprint. Transportation was assumed to be similar in both cases and neglected. Landfilling was not considered an option within the scope of the LCA due to the high level of uncertainty about quantifying lifetime GHG emissions associated with the practice and other externalities like land use considerations.

The Incineration, or combustion, of waste produces heat that can raise steam and generate electricity. Plastics have a high energy density (when compared to fuels like diesel), and therefore make good candidates for combustion treatment. Again, problems do arise since combustion of chlorinated plastics (such as PVC) would release dioxins requiring special pollution abatement (Kaminsky, 2006). Additionally, a study by Morris *et al.* determined that plastic recycling saves more energy from extracting virgin materials and production than is produced by incineration (Morris, 2005). As for the GFT scenario, the primary product was taken to be diesel fuel instead of electricity. Significant data exists on the gasification of coal, which is used in place of underdeveloped information on the gasification of plastics. Plastics and coal are on the same order of magnitude in terms of carbon content and heating value, see Figure 3.2 and Table 3.3.

3.4.1. Carbon Intensity of a Waste-to-Liquid Fuel Scenario

The LCA accounted for emissions from each unit operation, with the main culprits being combustion, venting, and fugitive sources. A comprehensive report by Marano and Ciferno in 2001 modeled the emissions from GFT processes from refinery data since both share many unit operations (Marano & Ciferno, 2001). Two GFT synthesis scenarios were considered: GFT-1 was the base scenario in which all emissions are vented to the atmosphere and all off-gas from the FTS reactor and the product upgrading is flared and GFT-2 assumed that nearly all the process off-gas is used for the cogeneration of heat, steam, and/or electricity. The incineration scenario is labeled PI below. Data regarding plastic incineration was scarce; therefore GHG emissions per unit heat presented in this comparative study was derived from a ratio of the average GHG emissions from the combustion of a plastic/rubber waste stream and an average heating value of plastics (Johnke, 2001). This value is calculated to be 36.47 kg CO_2-eq per million Btu. The task to compare the GHG emissions from various processes was not simple since it was heavily dependent on how to set the system boundaries and how accurate the data represents the processes. The LCA results are summarized in Figure 3.3, (a) in terms of kg CO_2-eq per million Btu of products and (b) in terms of ton of CO_2-eq per day of operation (processing 20 metric tons of waste plastics per day).

Compared to the conventional waste-to-energy scheme of incineration, both GFT-1 and GFT-2 resulted in more GHG emission per MBtu of products. It is important to note that these products are very different and a direct comparison is misleading. The GFT scenarios produced a value-added fuel, whereas the incineration method provides electricity. The comparison should only give a sense of scale to the greenhouse gas

emission analysis of GFT. Further, the combustion (end use) of upgraded liquid fuel has been left out of the GHG comparison. The results shown in Figure 3.3(b) illustrate how much carbon in waste plastics is transferred to during the process. As expected, most of carbon in waste plastics was used to generate liquid fuels in MWP and GFT technologies, while a significant amount of carbon was emitted as CO_2 during the incineration of plastics.

This analysis did not account for the environmental benefits associated with extracting less virgin carbon (crude oil) from the Earth. Also, CCS technologies under development have the potential to drastically reduce the carbon intensity of a GFT process. When compared against petroleum diesel, synthetic diesel was found to embody nearly double the carbon footprint (Schrag, 2009); therefore, CCS integration is a necessity. A study by the NETL found that removing a significant portion of the CO_2 flue gas from synthetic diesel production could significantly improve the greenhouse gas emissions disparity, becoming 5% to 12% better on a well to tank basis as compared with petroleum diesel (Tarka 2009).

Table 3.1 Summary of the effects of various independent parameters on dependent outcomes in gasification systems

	Independent Parameters (in order of most to least effective)[1]							
Dependent Parameters	Temp.	Catalyst	Steam	Addition of Plastic	Addition of Biomass	ER	Steam/MSW ratio	Residence time
H_2 Yield	++	++	+[2]	++	+	-	0	++
H_2/CO ratio	+	++	+[2]	++	+	-	+	++
Syngas Yield	++	++	+	++ → -[3]	--	0 / +[6]	++ → +[5]	++
Carbon Conversion	++	+	+	n/a	n/a	++	++	++
Heating Value of produced gas	- / +[4]	NR	-	++	++	--	-	--

SYMBOL NOTATION:
(++): Independent parameter INCREASES the amount of dependent parameter
(+): Independent parameter INCREASES MODERATELY the amount of dependent parameter
(--): Independent parameter DECREASES the amount of dependent parameter
(-): Independent parameter DECREASES MODERATELY the amount of dependent parameter
(0): Negligible effect
(→): Followed by
(NR): Not reported
(n/a): Not applicable

NOTES:
[1]Most experiments utilized atmospheric pressure condition. [2]When steam and catalyst are combined the trends become: H_2 yield (++) and H_2/CO ratio (++). [3]At high plastic loadings, several operational problems occur as a result of the formation of fine black powder, including plumbing clogs and catalyst deactivation. [4]The increase in gas yield at high temperature may be enough to compensate for the reduction in heating value due to loss of hydrocarbon gases.[5]Increasing steam/MSW ratio beyond a point results in a decreased syngas yield due to dilution and temperature conditions. [6]Conflicting results in the literature: (1) syngas yield does not change with ER (Aznar *et al.*, 2006) and (2) an effect is the result of increased O_2 favoring oxidation (Mastellone *et al.*, 2010).

Table 3.2 Optimum ranges for independent parameters influencing syngas production

Parameter	**Optimum Range**
Temperature (°C)	750-900 [a]
Catalyst	Calcined Dolomite, Al_2O_3, CaO, MgO [b]
Steam/MSW ratio (w/w)	0.5-0.8
Mixed Feed (wt%) Case A: Plastic + Biomass Case B: Plastic + Biomass + Coal	 20% + 80% 20% + 20% + 60%
Equivalence Ratio (ER)	0.2-0.4 [a]

[a] Depends on feedstock mix and desired syngas product
[b] Selection of catalyst based on price and availability

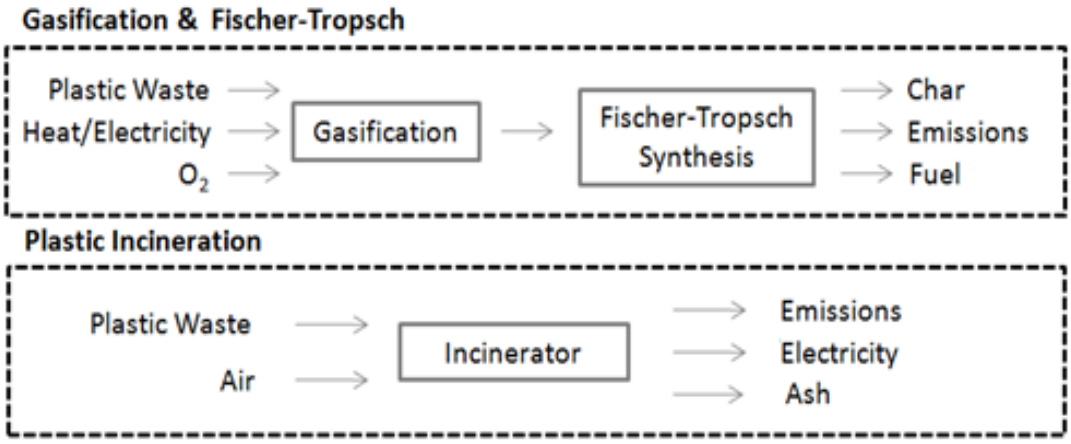

Figure 3.1 Scope of the lifecycle assessment with boundary conditions represented by dashed lines.

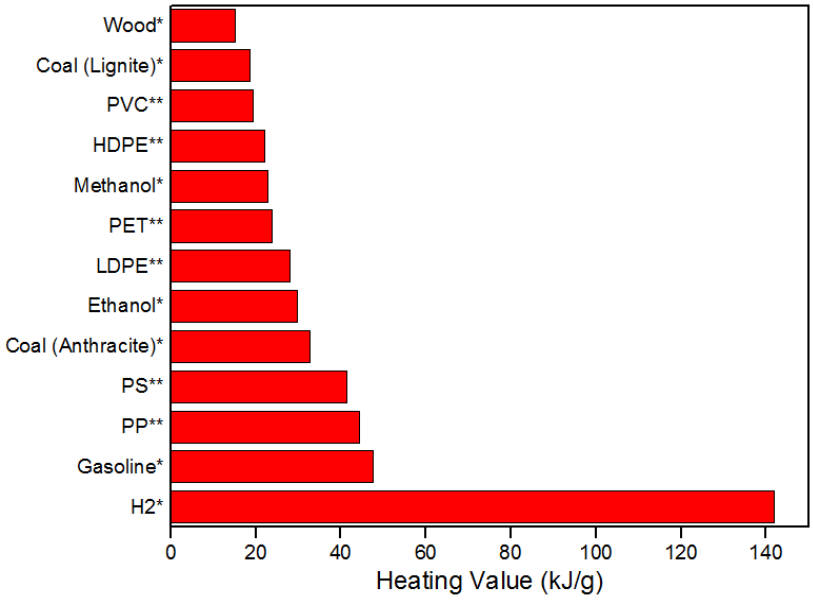

Figure 3.2 Heating values of various materials (NIST; EIA, 2008).

Table 3.3 Carbon Content of Gasification Feedstock

Material	Approx. C Content (wt. %)
Coal	75% *
Woody biomass	50% *
HDPE	85% **
PET	62% ***

* ORNL
** - $[C2H4]_n$ -
*** - $[C_{10}H_8O_4]_n$ -

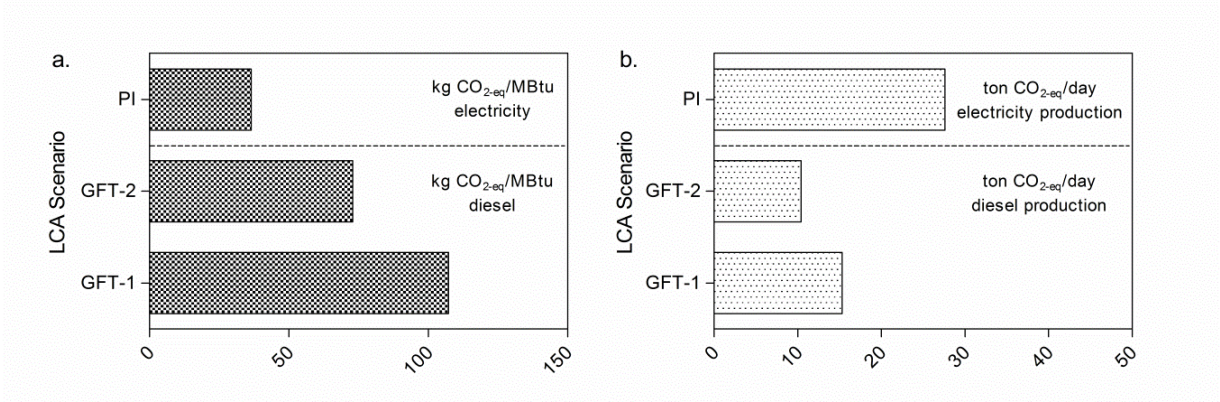

Figure 3.3 LCA result comparing emissions of two GFT processes and an incineration scenario for treating waste plastics in terms of (a) emissions per usable energy and (b) emissions per day of operation. Discussion of this figure can be found on pages 40-41.

4. Effect of H_2O on $Mg(OH)_2$ Carbonation Pathways for Combined CO_2 Capture and Storage

The contents of this chapter are published in Elsevier's *Chemical Engineering Science* (Fricker & Park, 2013).

4.1. Introduction

The rapid increase in carbon dioxide (CO_2) emissions from industrial sources is considered one of the main causes for the Earth's changing climate (IPCC, 2007). Reduction of CO_2 emissions can be achieved by improving energy efficiency, implementing renewable carbon-free energy sources, and developing carbon capture, utilization and storage (CCUS) technologies. Worldwide energy use will continue increasing (IEA, 2010), and thus, CCUS could provide an immediate solution to the global carbon imbalance while renewable energy technologies develop. By sequestering CO_2, the atmospheric CO_2 concentration can be stabilized or reduced. Most focus in the CCUS field has been placed on amine-based CO_2 capture combined with geological storage. While these technologies have already been demonstrated in large scales (Rochelle, 2009), amine-based CO_2 capture process and the geological storage of CO_2 still face challenges, such as high parasitic energy consumption during solvent regeneration and the permanence and accountability issues for long term CO_2 storage. Furthermore, these schemes would not allow direct integration of carbon capture and storage with high temperature energy conversion systems.

A few high temperature carbon capture schemes exist that utilize a metal oxide as a carbon capture medium such as Zero Emission Coal Alliance (ZECA) process and calcium looping technologies (Feng *et al.*, 2007). Numerous studies have shown that Ca-

based sorbents, often in the form of $Ca(OH)_2$ or CaO derived from $CaCO_3$, provide substantial carbonation conversion and kinetics (Feng *et al.*, 2007). Ca-based sorbents are attractive because they can be prepared using inexpensive resources such as limestone; however, since they are derived from carbonate mineral, Ca-based sorbents cannot be used as direct carbon storage. The spent sorbents need to be regenerated, which requires significant energy and cost, especially when accounting for sorbent degradation (Dasgupta *et al.*, 2008; Senthoorselvan *et al.*, 2009).

On the other hand, carbon mineralization technology that converts Mg-bearing minerals into mineral carbonates is a CCUS scheme that could combine CO_2 capture and storage technologies (IPCC, 2005). Research has shown that the abundance of suitable minerals, particularly those containing high magnesium fractions (e.g., olivine and serpentine), far exceeds the total CO_2 that could be produced from fossil fuel reserves (Lackner *et al.*, 1995). Mineralized carbon is significantly more thermodynamically stable than gaseous carbon, and carbonation reactions are exothermic. Thus, carbon mineralization is the most secure and permanent solution for carbon storage that does not require long-term monitoring (Lackner *et al.*, 1995). Unfortunately, mineral weathering naturally occurs on geological timescale; therefore, feasible carbon mineralization processes must provide significant enhancement to mineral dissolution and carbonation rates. As a result, most of the research in this area has been focused on the enhancement of silicate mineral dissolution (Equation 4.1), CO_2 hydration (Equation 4.2 and Equation 4.3), and carbonation (Equation 4.4) (Park & Fan, 2004).

Equation 4.1: $Mg_3Si_2O_5(OH)_4(s) + 6H^+ = 3Mg^{2+} + 2Si(OH)_4 + H_2O$

Equation 4.2: $CO_2(g) = CO_2(aq)$

Equation 4.3: $CO_2(aq) + H_2O = H_2CO_3(aq) = HCO_3^- + H^+ = CO_3^{2-} + H^+$

Equation 4.4: $Mg^{2+} + CO_3^{2-} = MgCO_3(s)$

These reactions have generally been performed in aqueous phase, which limits their application to relatively low reaction temperatures. By raising the pH without introducing CO_2 and producing $Mg(OH)_2$ instead of $MgCO_3$, a solid $Mg(OH)_2$ sorbent can be formed to capture CO_2 via high temperature gas-solid reactions (Equation 4.5 and Equation 4.6).

Equation 4.5: $Mg(OH)_2(s) = MgO(s) + H_2O(g)$

Equation 4.6: $MgO(s) + CO_2(g) = MgCO_3(s)$

The overall reaction becomes:

Equation 4.7: $Mg(OH)_2(s) + CO_2(g) = MgCO_3(s) + H_2O(g)$

Carbonation of Mg-based sorbents extracted from silicate minerals has seen less research interest, mainly due to its slower kinetics, though optimized reaction conditions and sorbent characteristics, such as surface area, can improve sorbent reactivity (Butt *et al.*, 1996; Goff & Lackner, 1998; Béarat *et al.*, 2002; Lin *et al.*, 2008; Zevenhoven *et al.*, 2008; Fagerlund *et al.*, 2010; Fagerlund & Zevenhoven, 2011). Much of the complexity of the $Mg(OH)_2$ carbonation system arises from the simultaneous dehydroxylation and carbonation reactions (Equation 4.5 and Equation 4.6), which occur in similar temperature ranges (Butt *et al.*, 1996). MgO carbonation has been shown to be considerably slower than $Mg(OH)_2$ carbonation. In fact, MgO is effectively unreacitve at low partial pressures of CO_2 (Béarat *et al.*, 2002; Zevenhoven *et al.*, 2008). Though $Mg(OH)_2$ is more reactive, the carbonation reaction can produce a diffusion limited carbonate shell which restricts the overall carbonation conversion (Butt *et al.*, 1996).

Some argue that the effect of water on $Mg(OH)_2$ carbonation was to prevent dehydroxylation (Fagerlund *et al.*, 2011). Other literature available on carbonation of Mg and Ca bearing oxides, hydroxides, and raw minerals supports a water enhanced carbonation theory under a wide range of reaction conditions (Shih *et al.*, 1999; Beruto & Botter, 2000; Kwak *et al.*, 2010; Kwak *et al.*, 2011; Kwon, 2011; Schaef *et al.*, 2011; Torres-Rodríguez & Pfeiffer, 2011; Larachi *et al.*, 2012; Loring *et al.*, 2012). Considering $Mg(OH)_2$ carbonation in slurry phase is relatively rapid (Botha & Strydom, 2001; Park *et al.*, 2003), the reaction mechanism likely proceeds through a different pathway when H_2O is involved. Highly hydrated environments may even eliminate the occurence of the heterogeneous carbonation reaction (Zhao *et al.*, 2010). Thus, this study aimed to investigate the effect of H_2O on the reaction pathways of $Mg(OH)_2$ carbonation in high pressure gas-solid experiments and a slurry phase experiment through systematic solid product analyses.

4.2. Experimental

4.2.1 Sample Preparation

Reagent-grade $Mg(OH)_2$ (Acros Organics) was used throughout the carbonation experiments. The particle size distribution was obtained through the laser diffraction measurement (LS^{TM} 13 320 MW, Beckman Coulter, Inc.). All $Mg(OH)_2$ particles were under 150 μm with the majority under 50 μm. $Mg(OH)_2$ particles had a surface area of 6.93 $m^2 \cdot g^{-1}$, and the majority of pores were under 5 nm in diameter (NOVA-win 2002 BET analyzer, Quantachrome Corporation). A thin layer of $Mg(OH)_2$ was coated on glass slides to minimize mass transfer limitations within bulk powder during reaction. The

layer was prepared by adding ~5 mL of a 0.1 $g \cdot mL^{-1}$ $Mg(OH)_2$ aqueous suspension to the slide and excess water was evaporated in an oven at 353 K overnight.

4.2.2 Low Pressure Carbonation of $Mg(OH)_2$

A Setaram SETSYS thermogravimetric analyzer (TGA) was used to perform atmospheric pressure carbonation experiments while allowing for continuous monitoring of reaction progress, in terms of mass change, and precise control of reaction temperature and gaseous environment composition. 30-50 mg samples of $Mg(OH)_2$ were loaded into alumina crucibles for each TGA run. Pure helium (He) or CO_2 was introduced to the TGA, and in all experiments the gas flow rate was maintained at 20 $mL \cdot min^{-1}$. Non-isothermal experiments used a slow temperature ramp rate (1-5 $K \cdot min^{-1}$), whereas isothermal experiments were quickly ramped (20 $K \cdot min^{-1}$) to the desired reaction temperature (533 K, 553 K, 573 K, 593 K) and held there for 12 hours.

4.2.3 High Pressure Carbonation of $Mg(OH)_2$

Figure 4.1 shows the experimental setup for the high pressure carbonation study, which consisted of a ~150 mL pressure vessel within a horizontal furnace (SC12.5R, The Mellen Company Inc.) and integrated thermocouples (type K, Omega). When preparing an experiment, two $Mg(OH)_2$-coated slides and, if applicable, a specific volume of water (1-5 mL) in an alumina combustion boat, were placed within the reactor. Subsequently, the reactor was pressurized with CO_2, sealed, and heated for one hour experiments, which included a temperature ramp to the reaction temperature (473 K, 573 K, or 673 K) followed by an isothermal reaction period. On average, experiments were performed with a temperature program of a 20 minute non-isothermal rise and a 40 minute isothermal

hold. After each experiment, the heating element was disconnected, gaseous contents were discharged upon cooling down to 523 K, and the reactor was purged with N_2 in order to stop the carbonation reaction. While the reactor was charged with the same amount of CO_2 for all experiments (~0.036 mol of CO_2), depending on the reaction temperature, the partial pressures of CO_2 during the experiments ranged from 1.03 to 1.45 MPa. The total pressure inside the reactor was monitored throughout the experiments and the difference between the total pressure and the CO_2 partial pressure was used to represent the H_2O pressure during the experiment.

4.2.4 Carbonation of $Mg(OH)_2$ Slurry

A pressure vessel (#U761, Pressure Products Industries, Inc.) with integrated temperature control and pressure sensor served as the reaction chamber. The internal volume within the glass reactor liner was ~300 mL, and the headspace within the sealed system was approximately 170 mL. An experiment began by mixing 8.75 g of $Mg(OH)_2$ with 300 mL deionized H_2O. The resulting 2.9 wt% slurry was sealed within the reactor, and CO_2 was then flowed through the headspace to purge the existing air. During this time, and throughout the rest of the experiment, an agitating stirrer was maintained at 700 rpm to ensure a homogeneously mixed slurry. After the initial 10 minute purging period, the reactor valves were sealed, the CO_2 pressure was increased to 1.52 MPa, and the heater was started. The experiment consisted of a 85 minute non-isothermal rise (averaged 2.3 $K \cdot min^{-1}$) followed by a 35 minute isothermal hold (average T = 478 K), and reached a maximum temperature of 486 K in 120 minutes. After the run, heat was removed and the reactor was left to cool until the internal temperature was below 373 K (approximately 100 minutes). The slurry was filtered and the solids were dried overnight

under vacuum at 353 K before being analyzed. The pH of the aqueous products was recorded as well. A blank experiment (the same as described previously, with pure H_2O and no slurry) was completed to observe the pressure changes in the reactor without the carbonation effect.

4.2.5 Product Analyses

A thermal analyzer (TA Q50, TA Instruments Inc.) was used for the approximate quantitative compositional analysis of the solid products. Multiple samples were taken from the product mixture of each experiment in order to evaluate the homogeneity of the solid products formed in sample slides. The solid samples were exposed to a nitrogen environment for calcination (N_2 flow rate: 20 $mL \cdot min^{-1}$) and the temperature was increased from 293 K to 923 K with a ramping rate of 5 $K \cdot min^{-1}$. The product composition was then estimated from the TGA curves by accounting for the mass changes associated with the thermal decomposition of the various species contained within the samples. For example, the thermal decomposition of absorbed H_2O, crystallized H_2O, hydroxide, and carbonate would all result in mass decrease at their characteristic temperatures. The derivative of the TGA signal (dTG) was integrated to calculate the weight loss associated with each decomposition step.

Since sampling at different locations on the sample slides resulted in non-homogeneity of analyzed solid products, further analysis was performed for each experiment on homogeneous mixtures of the two coated glass slides, which were obtained by scraping and grinding the solid particles with a mortar/pestle. The phase and crystallographic structure of the products were evaluated with an X-ray diffractometer (XRG 3000, Inel Inc.), where the powder X-ray diffraction (XRD) patterns were obtained

in the 2θ range of 10º to 70º at room temperature using CuKα radiation (λ = 1.5406 Å). Vibrational spectra of products were collected at room temperature using a Raman spectrometer (LabRAM ARAMIS Raman Spectrometer, Horiba JobinYvon) equipped with a microscope and a 40x UV objective. A UV laser and 1200 $gr \cdot mm^{-1}$ grating were used in these tests. The exposure time was set at 20 seconds and 4 scans were collected for each powder sample to improve signal-to-noise ratio.

4.3. Two-Step vs. One-Step Carbonation of $Mg(OH)_2$

As mentioned earlier, some literature has reported that MgO solid is effectively unreactive with gaseous CO_2 (Béarat *et al.*, 2002; Zevenhoven *et al.*, 2008). Thus, in order to verify this claim with our Mg-bearing sorbent and investigate the reaction mechanism and kinetics of each step involved (Equation 4.5 and Equation 4.6), the carbonation of $Mg(OH)_2$ was performed in a two-step mode: dehydroxylation of $Mg(OH)_2$ and carbonation of MgO. Using a TGA setup, $Mg(OH)_2$ was first calcined in a He environment to MgO as the furnace temperature was raised to 673 K, which is beyond the calcination temperature of $Mg(OH)_2$. After calcination was completed, verified by the stoichiometric mass loss, the temperature was lowered back to ambient conditions. Next, CO_2 was introduced to the TGA to allow for carbonation. As shown in the right section of Figure 4.2, the completely calcined MgO did not experience any visible mass gain, while complete carbonation would have resulted in a percent mass gain of 44.4%. Therefore, it was confirmed that at the partial pressure of CO_2 of 0.1 MPa, MgO is not reactive with CO_2. This two-stage reaction sequence was repeated for reproducibility at different reaction temperatures, heating rates, and reaction times, and in all cases

carbonation of MgO was minimal. Small weight gain at the end of each run was attributed to temperature-induced gas adsorption. As hypothesized by Butt et al. (1996), the dehydroxylation and carbonation reactions must be closely related.

Coupling the dehydroxylation and carbonation reactions at atmospheric pressure was then investigated by non-isothermal TGA experiments. Figure 4.3 shows $Mg(OH)_2$ samples subjected to a 2 $K \cdot min^{-1}$ ramp rate to 973 K in an inert He and CO_2 environment, respectively. When in the inert environment, the sample maintained a constant mass until the calcination temperature of $Mg(OH)_2$ at P_{H2O} = 0 MPa (~533 K marked as (a)) was reached, similar to the two-step case. With an identical temperature profile, but performed in a CO_2 environment, $Mg(OH)_2$ did not lose any mass until approximately 623 K, which was well beyond the calcination temperature of $Mg(OH)_2$. In fact, the thermal decomposition temperature of $Mg(OH)_2$ reacted in the CO_2 environment was very close to the calcination temperature of $MgCO_3$ at P_{CO2} = 0.1 MPa (~673 K marked as (b)). These results were similar to the those observed by Butt et al. (1996) and Lin et al. (2008), and it was hypothesized that carbonate species could be forming in the temperature range between the calcination temperature of $Mg(OH)_2$ and $MgCO_3$ where the mass was maintained. However, if $Mg(OH)_2$ was stoichiometrically reacting with CO_2 to form $MgCO_3$, there should have been significant mass gain prior to its calcination temperature, which was not observed in any of the TGA experiments. Thus, the single-step carbonation of $Mg(OH)_2$ seems to be more complex than a straight carbonation reaction.

While not direct proof of $Mg(OH)_2$ carbonation, the result from the one-step carbonation experiments demonstrated the interrelated nature of the two reactions

(Equation 4.5 and Equation 4.6). Some have suggested that the dehydroxylation-carbonation process is very much path dependent, and, therefore, reaction parameters such as reaction steps and heating rate are critical for the extent of carbonation (Béarat *et al.*, 2002; Lin *et al.*, 2008; Zevenhoven *et al.*, 2008; Kwon & Park, 2009). The presence of water vapor, as it is released through the solid $Mg(OH)_2$ matrix, may facilitate an ionic thin-film aqueous reaction leading to the carbonation of MgO sites. There has been a report on enhanced carbonation of MgO in the presence of humidified CO_2 (RH < 80%) at low temperature (T < 343 K) and atmospheric pressure (Torres-Rodríguez & Pfeiffer, 2011). The dehydroxylation dynamics (e.g., ultra-fast temperature ramping rate and vacuum condition) could also impact the morphological and crystalline structures of calcined $Mg(OH)_2$ and this may impact the subsequent carbonation of MgO (McKelvy *et al.*, 2001; Kwon & Park, 2009). However, none of these observations and speculations completely explain how $Mg(OH)_2$ carbonation is favored over MgO carbonation.

In order to further investigate this phenomenon, isothermal experiments were performed in the temperature range between the calcination temperatures of $Mg(OH)_2$ and $MgCO_3$ in different gaseous environments (pure He or CO_2) using the same TGA setup. In each experimental run, represented by a single line on Figure 4.4, the temperature of the TGA was programmed to quickly ramp at 20 $K \cdot min^{-1}$ to the desired reaction temperature where it was held for 12 hours. The results complement the findings from the non-isothermal experiments of the one-step carbonation study. In the He environment, $Mg(OH)_2$ decomposed because all the reaction temperatures were above its calcination temperature, and the decomposition rates followed kinetic theory, i.e. higher temperatures resulted in faster decomposition. The experiments in the CO_2 environment

were far more intriguing. As expected and seen in the non-isothermal experiments, in the chosen temperature range between 533 K and 593 K, the samples maintained nearly constant mass over the long experimental time. This suggested that the dehydroxylation and carbonation reactions were simultaneously occurring, which resulted in the constant mass of the samples throughout the experiments.

To assess and confirm the exact amount of carbonation that occurred for each run, at the end of the 12 hour runs the samples were collected and calcined in a furnace. The evolved gases were analyzed with the infrared CO_2 analyzer, which concluded that very little carbonation occured, only about 6% converted. In other words, $Mg(OH)_2$ in a CO_2 environment carbonates better than MgO—possibly due to the coupled dynamics between dehydroxylation and carbonation reactions. However, the extent of $Mg(OH)_2$ carbonation due to this phenomenon was not significant enough to fully carbonate $Mg(OH)_2$. Interestingly, it was also found that the presence of CO_2 suppressed the dehydroxylation of $Mg(OH)_2$. The reason for this phenomenon is uncertain at this point, given that dehydroxylation of $Mg(OH)_2$ was not suppressed in other gaseous environments such as nitrogen (N_2) or argon (Ar). The limited conversion of $Mg(OH)_2$ may be due to the formation of a diffusion limiting carbonate passivation layer but more studies are needed to evaluate additional reaction limitations (Butt *et al.*, 1996; Lin *et al.*, 2008). Some have suggested attrition via fluidization as a means of circumventing the mass transfer limitations (Fagerlund *et al.*, 2010; Fagerlund & Zevenhoven, 2011). Overall, the TGA results confirmed the infeasibility of $Mg(OH)_2$ carbonation at atmospheric pressure of CO_2.

4.4. Effect of H_2O Pressure on $Mg(OH)_2$ Carbonation

As shown in Equation 4.7, greater CO_2 pressure would allow the equilibrium shift towards the forward reaction of $Mg(OH)_2$ carbonation. Furthermore, the increased CO_2 pressure would also suppress the calcination of $MgCO_3$ given in Equation 4.6, and, as a result, $Mg(OH)_2$ carbonation can be performed at higher temperatures. Additionally, at higher temperatures, the carbonation rate should increase according to kinetic theory and provide a greater conversion of $Mg(OH)_2$ to $MgCO_3$ within the given reaction time of one hour. The extent of $Mg(OH)_2$ carbonation is defined as the percentage of total Mg in the reacted sample that was bound to carbon anhydrously. The mass change associated with anhydrous carbonate decomposition was easily distinguished from other phase decomposition temperatures, and it was used, in combination with stoichiometric ratios of Mg-bearing phases, to calculate two approximate Mg fractions (total Mg and Mg bonded to C). It should be noted that 100% conversion, as defined in this study, can only be achieved if the molar ratio of Mg:C = 1:1 as it is in magnesite ($MgCO_3$). If hydromagnesite ($Mg_5(CO_3)_4(OH)_2 \cdot 4H_2O$) is the predominant phase, the reported conversions could only achieve a maximum 80% conversion (Mg:C ratio = 5:4). Furthermore, reported conversions to anhydrous carbonate species should be used in relative comparison with the other samples in this study, as it has been shown that mass change at a given temperature may result from the decomposition of more than one phase (i.e. some CO_2 may be evolved during hydroxide decomposition) (Vágvölgyi *et al.*, 2008a).

First, $Mg(OH)_2$ carbonation was performed in the absence of steam and the results are shown in Figure 4.5 and marked as dry experiments. The dry experiments, at zero H_2O

pressure, showed that a critical CO_2 pressure must be surpassed for a given reaction temperature for carbonation of $Mg(OH)_2$ to proceed. At 473 K and 573 K, negligible carbonation was observed without H_2O present, while at 673 K, approximately 17.6% of $Mg(OH)_2$ was converted to carbonate. Each data point represents a single experiment and the error bars on Figure 4.5 were generated based on spatial variability of samples collected over the length of the glass slide.

Next, for experiments at each reaction temperature, different volumes of water were placed in the reactor to investigate the effect of increasing H_2O pressure on $Mg(OH)_2$ carbonation. As shown in Figure 4.5, $Mg(OH)_2$ reaction with CO_2 in the presence of H_2O at a given reaction temperature showed dramatic increases in carbonation conversion with increasing H_2O pressure. Conversion also increased with reaction temperature, likely due to faster reaction kinetics or changes in the thermodynamic stability of different Mg-bearing phases in the system, while the maximum carbonation temperature was limited by the equilibrium of Equation 4.6. The dependence of $Mg(OH)_2$ conversion on the H_2O pressure was greater at lower carbonation temperature, where the temperature effect on reaction kinetics was less pronounced. Initially, $Mg(OH)_2$ samples carbonated at 473 K and 573 K resulted in negligible carbonation at their particular CO_2 pressures; yet, upon the introduction of H_2O, they showed notable increases in conversion, ~33 and ~58 times respectively. As discussed earlier, the error bars in Figure 4.5 are associated with the spatial variability of product formation on the sample slide. Some solid products contained more than one Mg-bearing species (e.g., $MgCO_3$ and $Mg_5(CO_3)_4(OH)_2{\cdot}4H_2O$). This phenomenon was most pronounced for the experimental runs with excess water. Steam calculations revealed that in certain experiments at 473 K and high H_2O loading

(data points marked with * in Figure 4.5), the reactor was saturated and a liquid phase was present. This observation indicates that the presence of steam as well as the possibility of a water layer on the surface of $Mg(OH)_2$ may have led to different reaction pathways for $Mg(OH)_2$ carbonation, and, consequently, a range of Mg carbonate products.

In order to further investigate $Mg(OH)_2$ carbonation pathways, the differential thermogravimetric (dTG) traces of the solid products from each experiment were obtained. Each thermal decomposition pattern provided the information on the identification of Mg-bearing phase and the extent of $Mg(OH)_2$ carbonation. Figure 4.6 shows the example thermal decomposition patterns at T = 573 K and P_{CO2} = 1.24 MPa. As shown in Figure 4.5, $Mg(OH)_2$ carbonated in the absence of H_2O showed negligible conversion to carbonate, and it was confirmed in Figure 4.6(b), as its thermal decomposition temperature was very close to that of pure $Mg(OH)_2$ (Figure 4.6(a)). The hydroxide decomposition was shifted to slightly higher temperature, showing a doublet peak, which may be the result of a phase change within $Mg(OH)_2$. At medium water loading (P_{H2O} = 1.84 MPa), the dTG curve was distinctly different with three unique mass drops. Based on the reference temperatures, these peaks were assigned to the following approximate decomposition sequence: (i) crystallized H_2O starting to come off before 473 K, (ii) the hydroxide species starting to decompose just before 573 K (with the possibility of some CO_2 evolving in this range), and (iii) the release of CO_2 from anhydrous carbonate decomposition starting around 723 K (Vágvölgyi *et al.*, 2008a; Vágvölgyi *et al.*, 2008b). At the highest water loading (P_{H2O} = 3.71 MPa), two mass drops associated with H_2O release from hydroxide (at lower temperature) and CO_2 release from carbonate (at higher temperature) were observed. The CO_2 peak was

significantly larger, which translated into ~58% of $Mg(OH)_2$ being converted to $MgCO_3$. Interestingly, unlike in the case at P_{H2O} = 1.84 MPa, no crystallized water was detected.

To better understand the compositional changes during $Mg(OH)_2$ carbonation in the presence of steam, powder XRD was performed on the final products and the results are presented in Figure 4.7. Each plot (a-c) represents a series of experiments at a set reaction temperature and CO_2 pressure with varying H_2O pressure, and major compounds have been assigned according to XRD references (Downs, 2006). Again, the experiment conducted at 473 K with no H_2O experienced no carbonation; the pattern was effectively that of $Mg(OH)_2$ (i.e., brucite). Increasing H_2O pressure provided more carbonation and also more pattern disorder, which was associated with the presence of multiple hydrated carbonate phases including hydromagnesite and nesquehonite ($MgCO_3 \cdot 3H_2O$) and likely contributed to the larger errors in the TGA results found in the excess water loading cases at 473 K. Some of the anhydrous $MgCO_3$ peaks were also observed at P_{H2O} = 1.35 MPa. Minimal carbonation at 573 K in the absence of H_2O was confirmed by the XRD pattern in Figure 4.7(b). As H_2O pressure was increased, carbonate and hydrated carbonate peaks became visible with a relatively pure $Mg(OH)_2/MgCO_3$ product at H_2O pressure of 3.71 MPa. The lack of peaks at reaction temperature of 573 K and H_2O pressure of 1.84 MPa was likely the result of the formation of amorphous hydrated carbonate phases, since significant carbonation has already been confirmed by the TGA data (~31% conversion). At 673 K, the carbonate bands were not visible on the XRD pattern of the $Mg(OH)_2$ sample carbonated with no H_2O, and this may again likely be due to the formation of amorphous carbonate phases. At higher H_2O loadings however, the formation of

anhydrous carbonate species (i.e., magnesite) was dominant, while some minor peaks associated with unreacted $Mg(OH)_2$ were also observed.

UV-Raman analysis was employed to complement the XRD findings, observe amorphous phases, and look more closely at the carbonation mechanisms. Figure 4.8 contains UV-Raman spectra from each experimental run, with (a) depicting the overall spectrum from 200-2000 cm^{-1} and (b) and (c) showing detailed patterns at 1050-1200 cm^{-1} and 3300-3600 cm^{-1} respectively. Unreacted $Mg(OH)_2$ exhibits characteristic peaks near ~265 cm^{-1} and ~435 cm^{-1}, while characteristic peaks of magnesium carbonate species occur near ~195 cm^{-1} and ~325 cm^{-1} (Downs, 2006). The carbonate ion (CO_3^{2-}) v_4 in-plane bending mode is Raman active at ~725 cm^{-1} and its v_3 asymmetric stretching mode peaks appear at ~1430 cm^{-1}; however, most important to this study were the bands in the range of 1090-1120 cm^{-1} (Figure 4.8(b)), characteristic of the v_1 symmetric stretching mode of CO_3^{2-} (Edwards *et al.*, 2005; Downs, 2006). Depending on the carbonate compositions (i.e., magnesite, hydromagnesite and nesquehonite), the bands of the v_1 symmetric stretching mode of CO_3^{2-} were distinctly located within this range (Downs, 2006; Hänchen *et al.*, 2008; Frost, 2011).

As shown in Figure 4.8(b), pure $Mg(OH)_2$ does not have any Raman peaks in the region of 1090-1120 cm^{-1} but after each carbonation experiment the solid products started to show distinct carbonate peaks within this region. At low carbonation temperatures (473 K), the carbonate peaks appeared near ~1115 cm^{-1}, which is characteristic of the hydromagnesite phase. This result was consistent with the XRD and TGA findings. As the partial pressure of H_2O was increased to 1.35 MPa at 473 K, a small peak appeared near 1100 cm^{-1}, indicating the presence of magnesite or nesquehonite while

hydromagnesite remained as the predominant product. As the carbonation temperature was increased to 573 K, the symmetric stretching band of the carbonate Raman peaks was distinctly found as doublet, with peaks associated with both magnesite and nesquehonite (~1100 cm^{-1}) and hydromagnesite (~1115 cm^{-1}). This heterogeneity of solid product composition could explain the disordered XRD pattern shown in Figure 4.7(b). At the highest H_2O loading, the carbonated sample was confirmed to be mainly magnesite as illustrated by a single band at ~1100 cm^{-1} in Figure 4.8(b). When $Mg(OH)_2$ carbonation was performed at 673 K and high H_2O loading, only anhydrous CO_3^{2-} peak was observed, confirming that the formation of magnesite was favored at high reaction temperatures and P_{H2O}. As shown in Figure 4.8(c), the existence of hydrated species in samples carbonated at lower temperatures was confirmed by small peaks in the 3400-3550 cm^{-1} region, characteristic of crystallized H_2O (Hales *et al.*, 2008).

In summary, the comprehensive solid analyses of the reacted samples confirmed the following findings on $Mg(OH)_2$ carbonation: (i) increased H_2O pressure resulted in greater conversion of $Mg(OH)_2$ to carbonate, (ii) the predominant product phase was hydromagnesite at low temperatures, (iii) at 573 K the carbonate product was a mixture of hydrated and anhydrous carbonates, and (iv) at 673 K the formation of anhydrous carbonate species was dominant. Furthermore, at given carbonation temperatures, the increased H_2O pressure led to the favored formation of anhydrous magnesite.

4.5. Carbonation of $Mg(OH)_2$ in the Slurry Phase

The enhancement of $Mg(OH)_2$ carbonation by steam was apparent in the gas-solid high temperature and pressure carbonation experiments; accordingly, the next step was to

investigate an extreme case in a multiphase reactor with significantly more H_2O. The result follows a similar trend to those observed in the previous high pressure $Mg(OH)_2$ carbonation experiments. Carbonation in a heavily hydrated environment, at a similar temperature to the previous low temperature experiments (~473 K), resulted in an almost complete reaction between the available CO_2 and $Mg(OH)_2$. Reaction completion was verified by an approximate mass balance, where the extent of conversion was actually limited by the initial amount of CO_2 charged to the reactor. The ratio of C to Mg charged to the reactor was 0.87 (0.13 mol C to 0.15 mol Mg). CO_2 pressure after the reaction and cooling period also confirmed the carbonation reaction was CO_2 limited and all CO_2 had been converted to solid carbonate species.

The recovered solids were analyzed via TGA, XRD, and Raman with the same methodology as previous results to confirm the extent of carbonation as well as observe the carbonate phase formed during $Mg(OH)_2$ slurry carbonation. The decomposition of the solids, Figure 4.9(a), reveals two separate mass changes, a small drop around 623 K and a much larger mass change above 673 K. The secondary mass change resulted in a mass drop of 44.5%, indicating a large fraction of magnesite in the reaction product. The reaction conversion, defined as the percent of Mg bound to C anhydrously, was approximately 80.7%. XRD and Raman analyses complemented and confirmed the presence of anhydrous $MgCO_3$. Similar to the XRD patterns of Figure 4.7, the dominant peaks in Figure 4.9(b) were those of the magnesite phase with a minor presence of brucite (Downs, 2006). The Raman spectra in Figure 4.9(c) contains the characteristic peaks of magnesium carbonate species that occur near ~195 cm^{-1} and ~325 cm^{-1}, the carbonate ion (CO_3^{2-}) v_4 in-plane bending mode at ~725 cm^{-1} and its v_3 asymmetric stretching mode at

~1430 cm^{-1}, and, most importantly, the v_1 symmetric stretching mode of CO_3^{2-} at ~1100 cm^{-1} (Edwards *et al.*, 2005; Downs, 2006). The position of the v_1 symmetric stretching mode, combined with the very small OH^- stretching mode in the 3600s cm^{-1} and the absence of the characteristic crystalized H_2O peaks in the 3400-3550 cm^{-1} region, confirm the existence of a dominant magnesite phase (Hales *et al.*, 2008).

While the reaction time was significantly longer than that of the gas-solid case, due to limitations in the reactor heating rate, the results obtained in the $Mg(OH)_2$ slurry carbonation experiment also illustrated that the highly-hydrated environment can favor the formation of the anhydrous carbonate phase. Some of the enhancement in anhydrous carbonate production was likely related to the material aging time (Hänchen *et al.*, 2008); however, this effect alone may not explain a greater than two-fold increase in anhydrous carbonate conversion.

4.6. Potential Reaction Pathways

The agreement among TGA, XRD, and Raman data led to the following two major conclusions regarding the high pressure gas-solid carbonation of $Mg(OH)_2$. First, increasing H_2O pressure beyond a critical value resulted in the conversion of $Mg(OH)_2$ to anhydrous carbonates, potentially via a hydrated intermediate. Second, increasing carbonation temperature favored the formation of anhydrous carbonate because the intermediate species was unfavorable at high temperatures. These results, as well as the previously discussed relationship between dehydroxylation and carbonation of $Mg(OH)_2$, go beyond demonstrating the H_2O enhancement of $Mg(OH)_2$ carbonation and provide insight into the potential reaction pathways. The literature has suggested various H_2O

enhancement mechanisms of metal oxide and raw mineral carbonation that include preventing dehydroxylation forming unreactive MgO (Fagerlund *et al.*, 2011), accelerating fast ionic reaction between dissolved ions and CO_2 (Shih *et al.*, 1999; Torres-Rodríguez & Pfeiffer, 2011), and facilitating carbonation through a hydrated intermediate carbonate species (Kwak *et al.*, 2011; Schaef *et al.*, 2011; Loring *et al.*, 2012). Some have speculated that a threshold or a critical quantity of H_2O is required for any carbonation to occur in gas-solid reaction scheme (Shih *et al.*, 1999; Béarat *et al.*, 2002). The formation of hydrated magnesium carbonates in aqueous phase is widely recognized and is thought to be related to the highly hydrated nature of Mg^{2+} in solution (Hänchen *et al.*, 2008; Zhao *et al.*, 2010). The extreme carbonation studies performed using Mg-bearing minerals and water saturated supercritical CO_2 also demonstrated a threshold water content for complete conversion to an anhydrous $MgCO_3$ at low temperatures (< 373 K) (Kwak *et al.*, 2011; Schaef *et al.*, 2011; Loring *et al.*, 2012). These previous studies were mostly performed at relatively low carbonation temperatures, while anhydrous $MgCO_3$ formation is favored at high temperatures. Thus, the current study investigated gas-solid carbonation of $Mg(OH)_2$ in the presence of H_2O at higher carbonation temperatures (473-673 K).

The findings of the high pressure gas-solid carbonation experiments are in agreement with the hypothesis of the formation of intermediate hydrated species enhancing the overall extent of $Mg(OH)_2$ carbonation. The comprehensive solid analyses allowed more in-depth understanding of the proposed reaction pathway involving hydrated carbonate phases. The carbonation experiments at 473 K provided evidence to the production of anhydrous carbonates at higher H_2O pressures likely derived from intermediate hydrated

species, as shown in the limited amounts of anhydrous carbonate produced at low-moderate H_2O pressure. The experiments at 573 K showed that the possibility of a hydrated carbonate intermediate in the $Mg(OH)_2$ carbonation pathway could be plausible. At moderate P_{H2O}, hydrated carbonates were being formed, yet at higher P_{H2O}, $Mg(OH)_2$ was predominately converted to anhydrous magnesite. Mg's affinity for H_2O, as witnessed in various precipitation and carbonation studies reported in literature (Hänchen *et al.*, 2008; Zhao *et al.*, 2010), resulted in the formation of hydrated carbonate species under lower reaction temperatures and H_2O pressures. These results support the hypothesis that a H_2O threshold is needed to form anhydrous carbonate species (Kwak *et al.*, 2011; Schaef *et al.*, 2011; Loring *et al.*, 2012).

The slurry carbonation of $Mg(OH)_2$ was significantly above the H_2O threshold, as the slurry phase is a highly-hydrated environment. When $Mg(OH)_2$ in the slurry phase was exposed to a P_{CO2} of 1.52 MPa at 298 K and subsequently heated to 486 K over 120 minutes, most of the products were anhydrous carbonates. Zhao et al. (2010) found the carbonation of a brucite slurry to occur homogeneously in the aqueous phase at room temperature and CO_2 pressure up to 1.52 MPa and achieved complete conversion to nesquehonite in a couple of hours. The formation of anhydrous carbonates suggested that the reaction may not have proceeded through a hydrated intermediate pathway. However, it remains entirely plausible that a hydrated intermediate was formed, and that due to the large excess of H_2O, high temperature, and/or aging time, it was converted to anhydrous $MgCO_3$. The solubility of both CO_2 and $Mg(OH)_2$ is favored at lower temperatures (Park *et al.*, 2003); therefore, the temperature ramping rate could have significantly affected the reaction mechanism and product phase formed.

Schaef et al. (2011) argued that the availability of H_2O to strategically condense with OH groups of the $Mg(OH)_2$ matrix is important, as the condensation provides a reactive MgO site for subsequent carbonation reaction. This resembles the phenomenon observed during the high pressure carbonation experimental study. Thus, the following reaction steps can be described for carbonation of $Mg(OH)_2$ in the presence of H_2O: (i) critical amount of H_2O present results in the hydration of hydroxide groups, (ii) hydration enhances the reactivity of MgO sites, (iii) MgO, stabilized by surrounding H_2O molecules, can react with CO_2 to produce a hydrated carbonate species, and (iv) depending on the reaction temperature, dehydration of hydrated carbonate occurs, forming anhydrous $MgCO_3$ (Schaef *et al.*, 2011). The findings of this study are summarized in Figure 4.10 as a schematic phase diagram with three different carbonation pathways. It was experimentally proven that the two-step process (Pathway 1) involving the calcination of $Mg(OH)_2$ and subsequent carbonation of MgO was not feasible under a wide range of reaction conditions. The direct carbonation of $Mg(OH)_2$ (Pathway 2), the result of the coupled dehydroxylation and carbonation reactions was promising, though only under elevated temperature and possibly highly-hydrated conditions. The use of H_2O through a mechanism involving a hydrated carbonate intermediate (Pathway 3) can provide significant conversion under moderate reaction conditions. Ultimately, the production of anhydrous $MgCO_3$ from $Mg(OH)_2$ can be enhanced by one or a combination of increasing H_2O loading, higher carbonation temperature, and/or longer reaction time.

4.7. Summary

After exploring and verifying the limitations observed in gas-solid carbonation of $Mg(OH)_2$, the current study investigated the enhancement of carbonation with increasing temperature and H_2O pressure through systematic solid product analyses. Low pressure $Mg(OH)_2$ carbonation experienced limitations over a large temperature range, while elevated CO_2 pressures only marginally increased reactivity. In the presence of steam however, $Mg(OH)_2$ carbonation was enhanced, likely due to a shift in the carbonation pathway, which provided faster carbonation reaction kinetics. The results suggest that the high temperature carbonation of $Mg(OH)_2$ in steam is a complex process likely involving a hydrated transition state. The trend of increasing H_2O presence favoring the production of anhydrous $MgCO_3$ was supported by the slurry carbonation experiment, though other variables like temperature ramping rate and aging time could be at play. The investigation is being continued to evaluate a wider range of experimental conditions in a continuous flow reactor system, with H_2O pressures in industrially compatible ranges, in order to further evaluate the fundamental mechanisms and kinetics of H_2O enhanced carbonation of $Mg(OH)_2$. Testing of the slurry carbonation system is ongoing to evaluate optimal carbonation condtions, investigate the dependence of carbonate product phase on various reaction parameters, and determine the reaction pathway in the slurry phase.

Notation

λ	Wavelength
BET	Surface area analysis technique (Brunauer, Emmett, and Teller)
CCUS	Carbon, capture, utilization, and storage
dTG	Differential thermogravimetry
$MgCO_3$	Magnesium carbonate, Magnesite
$MgCO_3 \cdot 3H_2O$	Nesquehonite
$Mg_5(CO_3)_4(OH)_2 \cdot 4H_2O$	Hydromasgnesite
$MgCO_3 \cdot Mg(OH)_2 \cdot 3H_2O$	Artinite
MgO	Magnesium oxide
$Mg(OH)_2$	Magnesium hydroxide, Brucite
$Mg_3Si_2O_5(OH)_4$	Serpentine (Magnesium iron silicate hydroxide)
P_x	Partial pressure of species X
RH	Relative humidity
T	Temperature
TGA	Thermogravimetric Analyzer
UV-Raman	Raman spectroscopy with a ultra violet light source
XRD	X-ray diffraction
ZECA	Zero Emission Coal Alliance

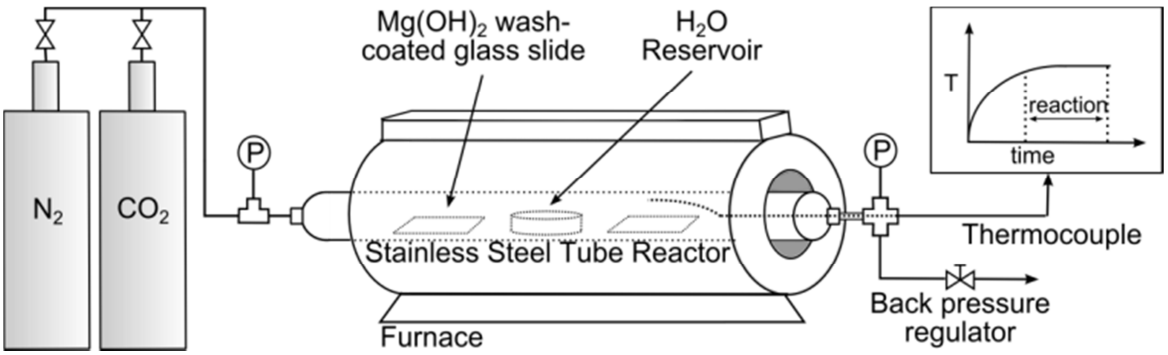

Figure 4.1: Schematic diagram of high temperature and pressure experimental setup.

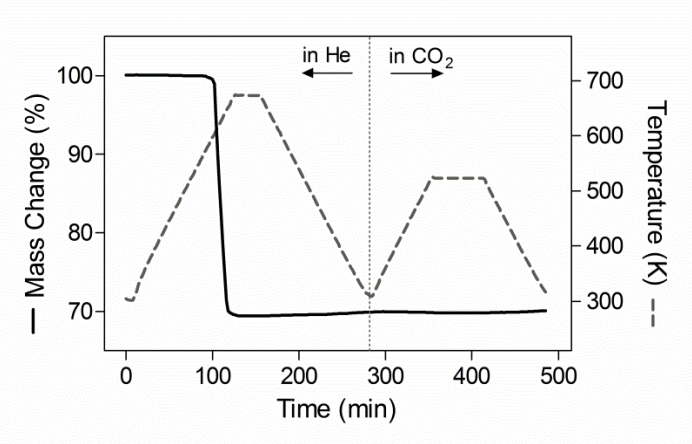

Figure 4.2: Two-step dehydroxylation and carbonation of $Mg(OH)_2$ in He and CO_2 environments in a TGA. Reaction conditions: P_{total} = 1 atm, gas flow rate = 20 mL•min^{-1}.

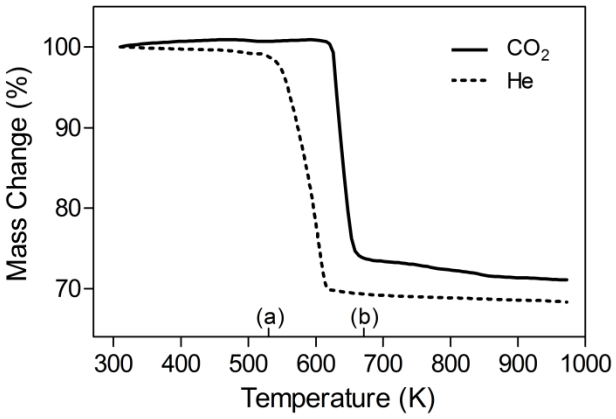

Figure 4.3: Nonisothermal, one-step dehydroxylation and carbonation of $Mg(OH)_2$ in He and CO_2 environments in a TGA. Reaction conditions: P_{total} = 1 atm, temperature ramp rate = 2 K•min^{-1}, gas flow rate = 20 mL•min^{-1}. Labels: theoretical calcination temperatures of (a) $Mg(OH)_2$ at P_{He} = 0.1 MPa and (b) $MgCO_3$ at P_{CO2} = 0.1 MPa.

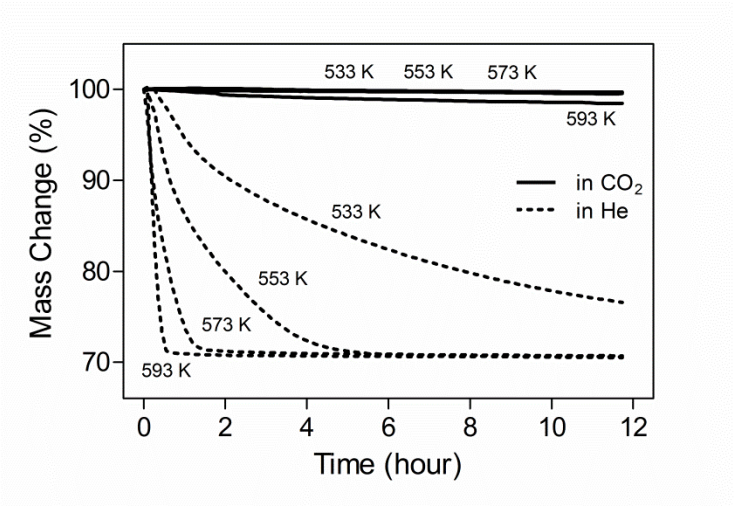

Figure 4.4: Isothermal, one-step dehydroxylation and carbonation of $Mg(OH)_2$ in He and CO_2 environments in a TGA. Reaction conditions: P_{total} = 1 atm, temperature ramp rate = 20 K•min^{-1} (before isothermal hold), gas flow rate = 20 mL•min^{-1}.

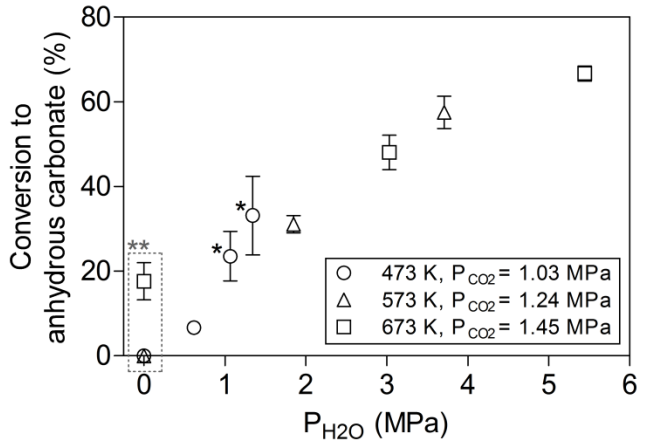

Figure 4.5: Effect of P_{H2O} on the extent of carbonation of $Mg(OH)_2$ to anhydrous carbonate (reaction time = 60 min) as a function of reaction temperature and the partial pressure of CO_2 determined via TGA decomposition. Labels: *Significant $H_2O(l)$ was present in the reactor (steam quality ~0.2-0.4) and **Dry experiments.

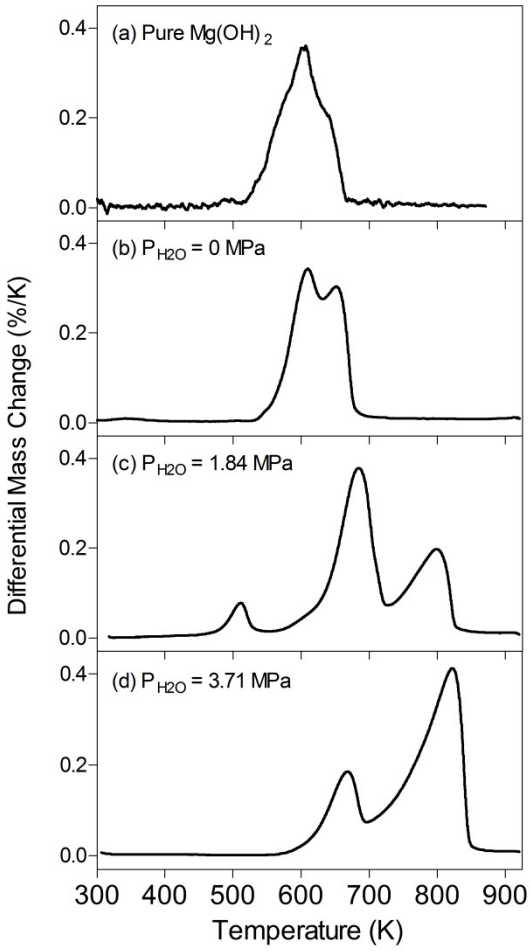

Figure 4.6: Differential mass change during the thermal decomposition of samples carbonated under different partial pressures of H_2O. Samples were reacted at 573 K and P_{CO2} = 1.24 MPa.

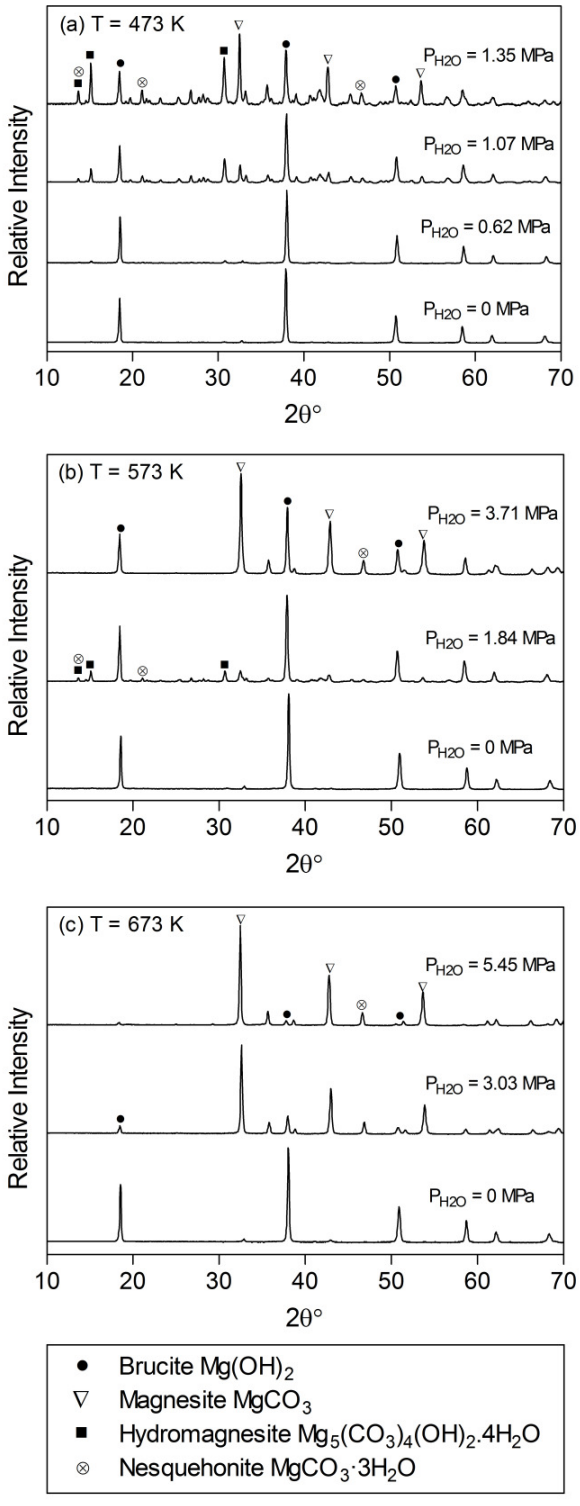

Figure 4.7: XRD patterns of $Mg(OH)_2$ samples reacted at different temperatures and partial pressures of H_2O. Reaction conditions: (a) T = 473 K and P_{CO2} = 1.03 MPa, (b) T = 573 K and P_{CO2} = 1.24 MPa, and (c) T = 673 K and P_{CO2} = 1.45 MPa CO_2.

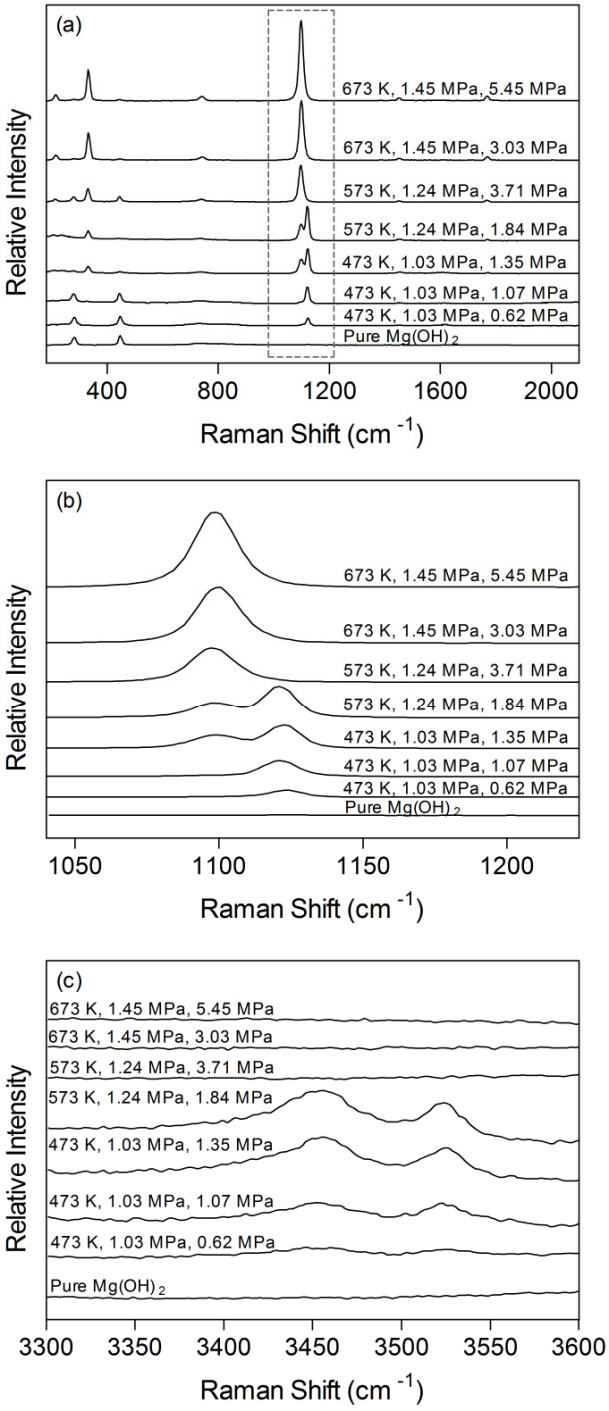

Figure 4.8: Raman spectra of $Mg(OH)_2$ samples carbonated at different reaction temperatures and partial pressures of H_2O. Graphs: (a) full spectra, (b) CO_3^{2-} symmetric stretching region, and (c) H_2O stretching region. Reaction conditions (T, P_{CO2}, P_{H2O}) are given above each spectra.

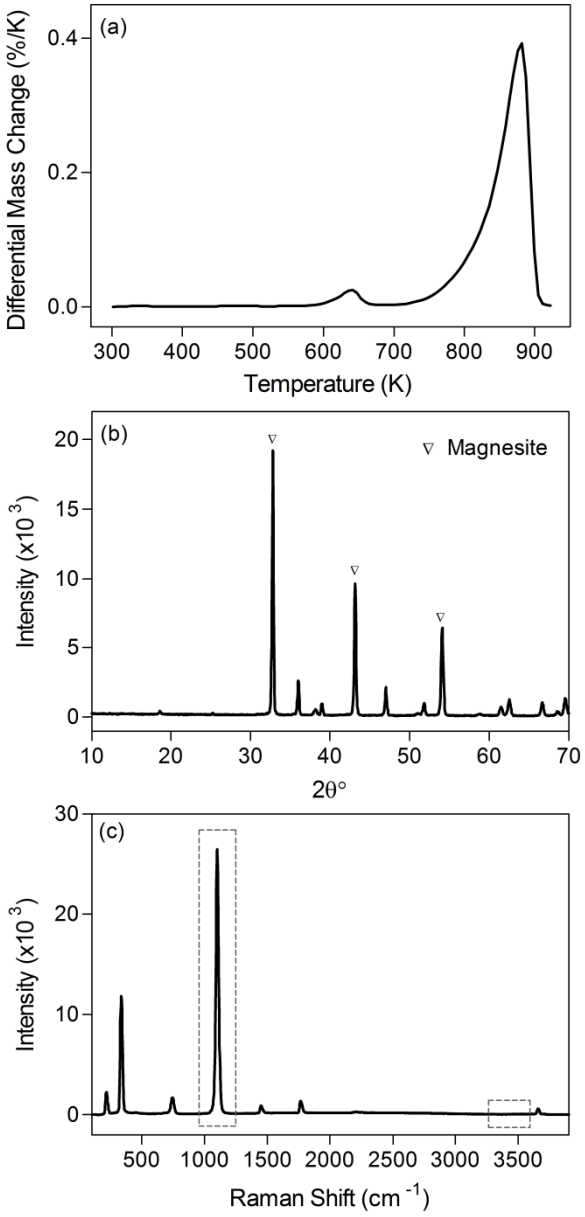

Figure 4.9: Analysis of reaction products of the slurry carbonation experiment with 8.75 g of $Mg(OH)_2$ in 300 mL H_2O. Reaction conditions: $P_{o,CO2}$ = 1.52 MPa, T_o = 298 K, T_f = 486 K, reaction time = 120 min. Graphs: (a) Differential mass change during the thermal decomposition, (b) XRD pattern, and (c) Raman spectra.

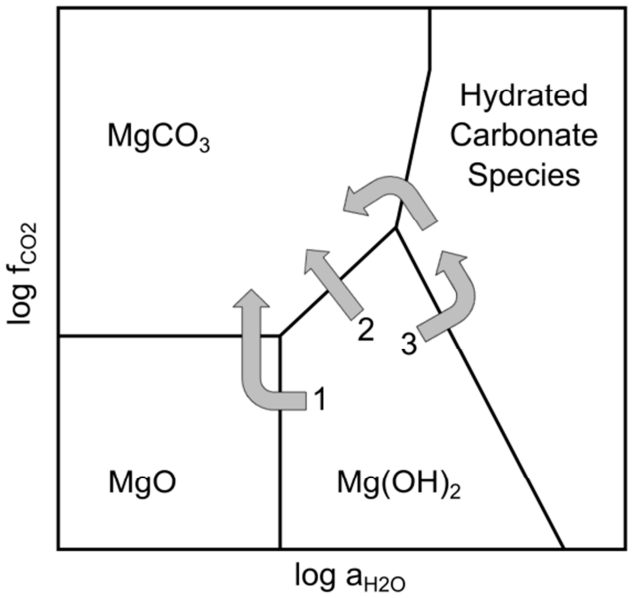

Figure 4.10: Schematic equilibrium phase diagram of $MgO-H_2O-CO_2$ system with possible carbonation pathways. Diagram produced using Geochemists Work Bench software (Release 7.0.2) (Bethke, 2008) at T = 573 K and P_{total} = 0.1 MPa (basis, magnesite activity = 1).

4.8. Supporting Information

4.8.1. Characterization of $Mg(OH)_2$ Reagent

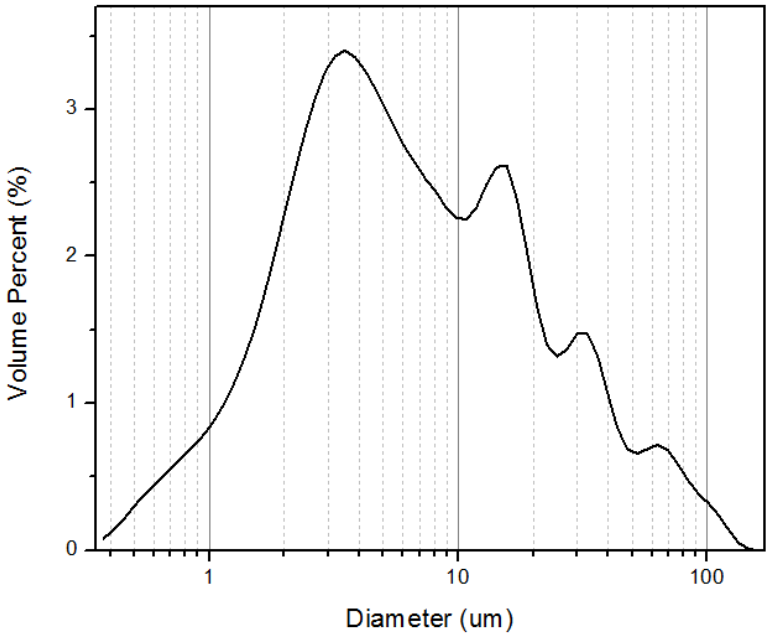

Figure 4.11 Particle size distribution according to pore diameter of reagent grade $Mg(OH)_2$ (Acros Organics) used in study. All particles are under 150 μm with the majority under 50 μm.

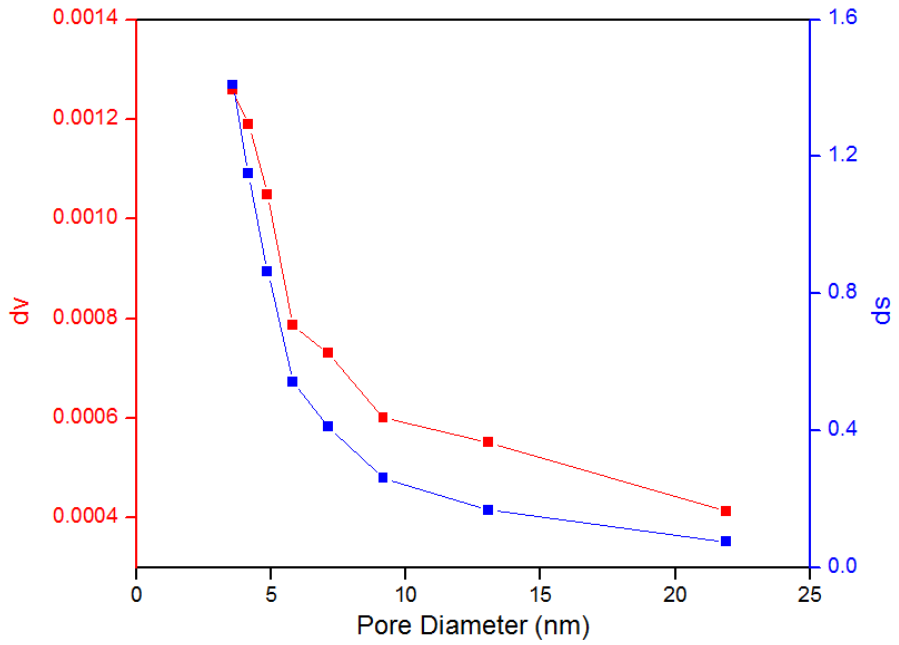

Figure 4.12 Pore size distribution of reagent grade $Mg(OH)_2$ used in study. Results presented in terms of volume ("dv") in $cm^3/nm/g$ and surface area ("ds") in $m^2/nm/g$. The sample has a BET surface area of 6.93 m^2/g, and the majority of pores are under 5 nm in diameter. Characterization data was averaged from multiple runs to ensure accuracy.

5. Investigation of the Different Carbonate Phases and their Formation Kinetics during $Mg(OH)_2$ Slurry Carbonation

The contents of this chapter are in review for publishing in the American Chemical Society's *Industrial & Engineering Chemistry Research* (Fricker & Park, 2014).

5.1. Introduction

While evidence of the relationship between anthropogenic CO_2 emissions and global climate change builds (IPCC, 2007), fossilized fuels continue to and will dominate the worldwide energy mix for decades to come (EIA, 2013). As incremental improvements are made in the efficiency sphere and carbon-free energy technologies develop and secure market share, carbon capture and storage (CCS) technologies can be deployed to mitigate greenhouse gas emissions during the transition period, which could prove to be very long. Numerous CCS technologies are under development, with much of the focus on CO_2 capture; however, capture only addresses half of the problem. After capture, CO_2 must be compressed to high pressure (~150 atm) and transported to a suitable geological formation for storage. Uncertainty in the permanence and safety of geological CO_2 storage as well as the need for costly monitoring add to the complexity of this CCS scenario.

Combined CO_2 capture and storage via carbon mineralization represents an alternative solution. Occurring naturally on geological timescales, carbon mineralization is the process by which gaseous or aqueous CO_2 reacts with solid or dissolved minerals to form safe, thermodynamically stable mineral carbonates, e.g. $MgCO_3$ and $CaCO_3$ (Lackner *et al.*, 1995). The doubt associated with the fate of geologically stored CO_2, which may form mineral carbonates or may slowly permeate

back to the surface over long times, is avoided with ex-situ mineralization schemes. In addition, combining CO_2 capture and storage has the added benefit of avoiding the energy intensive and chemically complicated sorbent regeneration operation. Carbonation with inexpensive Ca-based sorbents, derived from natural carbonate minerals (i.e. limestone), is proven to have fast kinetics and sufficient capture capacity (Feng *et al.*, 2007). However, these Ca-based sorbents start as carbonates, and therefore only represent a regenerable carbon capture solution. Further, the sorbent regeneration requires significant energy (temperatures around 900 °C) (Senthoorselvan *et al.*, 2009). In contrast, Mg-based sorbent materials derived from profuse silicate minerals or industrial wastes provide an optimal solution for combined carbon capture and storage. Unfortunately, previous studies of gas-solid carbonation of both MgO and $Mg(OH)_2$ sorbents showed slow kinetics and limited overall conversion (Butt *et al.*, 1996; Béarat *et al.*, 2002; Lin *et al.*, 2008; Zevenhoven *et al.*, 2008; Fricker & Park, 2013). Thus, steam introduction (Fricker & Park, 2013) and advanced reactor design with pressurized fluidized bed (Fagerlund *et al.*, 2012) were introduced to improve the performance of Mg-based sorbents.

The aqueous mineral carbonation field has experienced significant interest in recent history, with $Mg(OH)_2$ carbonation in the slurry phase known to be relatively fast (Botha & Strydom, 2001; Park *et al.*, 2003; Zhao *et al.*, 2010; Hövelmann *et al.*, 2012; Harrison *et al.*, 2013). The presence of a substantial H_2O phase shifts the reaction mechanism through a different pathway than dry $Mg(OH)_2$ carbonation (Fricker & Park, 2013). In the aqueous systems, especially at temperatures below the decomposition of $Mg(OH)_2$, a homogeneous carbonation reaction is expected. A

multi-step CO_2 hydration (Equation 5.1 and Equation 5.2), dissolution (Equation 5.3), and carbonation (Equation 5.4, Equation 5.5, and Equation 5.6) process has been proposed. Zhao et al. confirmed the homogeneous nature of the carbonation reaction of a $Mg(OH)_2$ slurry by measuring the dependence of the carbonation reaction rate on Mg^{2+} concentration (Zhao *et al.*, 2010). CO_2 hydration reduces pH, and therefore, would enhance the dissolution of $Mg(OH)_2$. Bicarbonate (HCO_3^-) and chloride (Cl^-) were also reported to enhance $Mg(OH)_2$ dissolution by acting as a ligand, forming surface complexes that interfere with MgO bonds and surface Mg coordination (O'Connor *et al.*, 2004; Hövelmann *et al.*, 2012).

Equation 5.1: $CO_2(aq) + H_2O \leftrightarrow H_2CO_3(aq)$

Equation 5.2: $H_2CO_3(aq) \leftrightarrow HCO_3^-(aq) + H^+(aq) \leftrightarrow CO_3^{2-}(aq) + H^+(aq)$

Equation 5.3: $Mg(OH)_2(s) + 2H^+(aq) \leftrightarrow Mg^{2+}(aq) + 2H_2O$

Equation 5.4: $Mg^{2+}(aq) + CO_3^{2-}(aq) + 3H_2O \leftrightarrow MgCO_3 \cdot 3H_2O(s)$

Equation 5.5: $5Mg^{2+}(aq) + 4CO_3^{2-}(aq) + 2OH^-(aq) + 4H_2O \leftrightarrow Mg_5(CO_3)_4(OH)_2 \cdot 4H_2O(s)$

Equation 5.6: $Mg^{2+}(aq) + CO_3^{2-}(aq) \leftrightarrow MgCO_3(s)$

Under certain reaction conditions, especially in H_2O saturated environments, different magnesium carbonate phases can be produced, including anhydrous magnesite ($MgCO_3$) and hydrated carbonate species like nesquehonite ($MgCO_3 \cdot 3H_2O$) and hydromagnesite ($Mg_5(CO_3)_4(OH)_2 \cdot 4H_2O$) (Equation 5.4, Equation 5.5, and Equation 5.6). Distinct boundaries exist where specific magnesium carbonate phases are stable; although, thermodynamic calculations show anhydrous magnesite to be the stable phase at all temperatures and CO_2 pressures (Kittrick &

Peryea, 1986). Carbonate precipitation is kinetically controlled, and hydrated carbonates form preferentially due to the high free energy required for dehydration (Sayles & Fyfe, 1973; Deelman, 2001). The difficulty in precipitating anhydrous carbonate is attributed to the highly hydrated character of Mg^{2+} in aqueous solution (Sayles & Fyfe, 1973; Hänchen *et al.*, 2008). The first hydration shell of Mg^{2+} has six water molecules (Tommaso & de Leeuw, 2010), which must be excluded in order to form anhydrous carbonate. At low temperature and CO_2 pressure, magnesite is ultimately produced according to Ostwald rule of phases, where metastable phases like nesquehonite or hydromagnesite is first formed and subsequently transformed into the stable magnesite (Deelman, 2001). Demonstrated in 1949, supersaturated (metastable) solutions were prepared by leaching MgO and $Mg(OH)_2$ with CO_2 in aqueous phase (Evans & St. Clair, 1949), though magnesite could not be precipitated due to high level of hydration even at conditions of high supersaturation (Sayles & Fyfe, 1973; Saldi *et al.*, 2009). The metastability of hydrated magnesium carbonates is of relevance to the proposed CCS process since the anhydrous carbonate is the desired product from a storage perspective. The hydrated carbonates are more soluble than magnesite (Hänchen *et al.*, 2008) and have significantly more volume and weight, and thus, higher costs will be associated with their processing and transportation. Furthermore, the formation of hydrated carbonate species will result in the loss of process water.

Various methods for mitigating the kinetic inhibition in forming anhydrous magnesite have been suggested, including: operation at temperature and CO_2 pressure conditions where hydrated carbonates are not kinetically favored, allowing longer

aging time (Hänchen *et al.*, 2008), reduction of the activity of H_2O by adding interfering ions (e.g. Cl^- and NO_3^-) (Sayles & Fyfe, 1973), or decreasing the activity of Mg^{2+} via complexation with organic compounds (e.g. monoethylene glycol) (Sandengen *et al.*, 2008). The slurry phase $Mg(OH)_2$ carbonation system for combined CCS still lacks a systematic understanding of reaction kinetics and mechanisms of the complex competing and parallel reactions, especially at high temperatures. Thus, this study combined real-time slurry sampling and detailed solid product analyses to provide insight into slurry phase $Mg(OH)_2$ carbonation. Exploring reaction temperatures higher than previously studied, this study focused on the effect of temperature, in the range 30-200 °C, on $Mg(OH)_2$ slurry carbonation kinetics and the composition of the formed magnesium carbonate phases.

5.2. Experimental

5.2.1. Methods

As depicted in Figure 5.1, a temperature-controlled, pressurized continuously stirred tank reactor (CSTR) (#U761, Pressure Products Industries, Inc.) outfitted with thermocouples (type K, Omega) and a pressure transducer (Omega) was employed as the slurry phase carbonation reactor. Experiments began by forming a 2.9 wt% slurry composed of 8.75 g of dry $Mg(OH)_2$ (reagent grade, Acros Organics) and 300 mL of deionized H_2O within the glass reactor liner. Experiments with various additives (1.4 wt% HCl, 1 M NaCl, 0.5 M $NaHCO_3$, and the combination of 1 M NaCl and 0.5 M $NaHCO_3$) included an additional step where the additive was introduced to the deionized H_2O prior to mixing with the dry $Mg(OH)_2$ particles. The reactor was

sealed, and nitrogen (N_2) was flowed through the headspace for 10 min to remove any oxygen (O_2) inside the system. During the startup time and throughout the experiment, a magnetically driven stirrer within the slurry operated at 700 rpm to ensure homogeneous mixing of solid and liquid phases.

The reaction parameters explored in this study are listed in Table 5.1. In experiments conducted at constant P_{CO2} (marked with †), CO_2 was injected at the reaction temperature. For these tests, the reactor, with gas valves sealed and $P_{o,N2}$ = 1 atm in headspace, was heated to the set reaction temperature (30-200 °C). After temperature and pressure (including the expansion of N_2 and the associated P_{H2O} at that temperature) were stabilized, a CO_2 cylinder and regulator were used to deliver the constant P_{CO2} of 15 atm. Alternatively, for the experiments conducted with a fixed CO_2 amount, CO_2 (15 atm) was injected into the headspace at reaction temperature (again after H_2O and N_2 pressure stabilization) or room temperature after the N_2 purge. Then the gas line valves were sealed to start the experiment. In the case of room temperature CO_2 injection, the reactor was heated after valves were sealed. Experiments were generally run isothermally for 120 min to allow ample time for reaction, though some experiments investigated shorter (90 min) and longer (up to 1080 min) reaction times. The results of the experiments at 30 °C, 150 °C and 200 °C with constant P_{CO2} (marked with †) are reported as the average of three replicate experiments.

The kinetics of carbonate formation from a $Mg(OH)_2$ slurry were investigated via the solids analysis of slurry samples taken at time intervals (15-30 min). Each slurry samples was filtered (particle size retention: >11 μm, GE Whatman) as soon as it was

collected to stop further reaction. The filtrate (200 μL) was diluted 50 times by combining with 9.8 mL of 2 % nitric acid for subsequent Mg^{2+} concentration analysis via an inductively coupled plasma optical emission spectrometer (ICP-OES) (ACTIVA-M, Horiba Jobin Yvon, Inc.). The concetration was calculated from average of 3 spectral lines. Error bars on quantitative analyses represent the results of multiple different slurry carbonation experiments. Solids were dried in a vacuum oven overnight, and analyzed via various techniques to determine the carbonate conversion and phase produced.

5.2.2. Solid Analysis

The carbonated solid samples were analyzed using a battery of analytical tools. First, thermogravimetric analysis (TGA) (SETSYS Evolution, Setaram Instrumentation) was performed by heating ~20 mg of sample in helium (He) (20 $mL \cdot min^{-1}$) to 650 ºC at a temperature ramping rate of 5 $ºC \cdot min^{-1}$. Various species (i.e. absorbed H_2O, crystallized H_2O, hydroxide, and carbonate) within the sample decompose at characterisic temperatures, and thus, the mass change during a thermal scan was used to quantify the different compounds in a solid sample. The derivative of the mass signal from the TGA (dTG) was examined to elucidate the different mass change events. An X-ray diffractometer (XRD) (X2, Scintag, Inc.) was used to confirm and further clarify the carbonate phases. Samples were scanned in the 2θ range from 10º to 70º with a step size of 0.05º and scan time of 0.5 s at room temperature using Cu Kα radiation. A scanning electron microscope (SEM) (S-4700 FE-SEM, Hitachi, Ltd.) was used to study the morphological structures of the carbonation products with an acceleration voltage of 5 kV.

Since the compostion of solid samples can be quite complex due to different carbonate phases and unreacted $Mg(OH)_2$, a carbon analyzer (CO_2 Coulometer, UIC, Inc.) was utilized for more accurate quantitiaive analysis of the carbon content within solid samples. The samples (~30 mg) were inserted into a furnace at 950 ºC with oxygen (O_2) flowing at 100 $mL \cdot min^{-1}$ for rapid decomposition of all carbonaceous species. The evolved gases were introduced to an electrochemical titration assembly which generates hydroxide to neutralize the CO_2. The carbon analyzer then outputed a mass of carbon contained within the sample. Finally, the percentage of a solid that was a particular carbonate phase was calculated using the carbon percentage and stoichiometry derived from qualitative TGA and XRD analyses.

5.3. Effect of Reaction Temperature on $Mg(OH)_2$ Slurry Carbonation

Unlike $Mg(OH)_2$ carbonation in the gas-solid system, which experiences slow kinetics and limited overall conversion (Butt *et al.*, 1996; Béarat *et al.*, 2002; Lin *et al.*, 2008; Zevenhoven *et al.*, 2008; Fricker & Park, 2013), slurry phase carbonation is relatively rapid and proceeds nearly to complete reaction between the available CO_2 and $Mg(OH)_2$ (Zhao *et al.*, 2010). Mass balances on the preliminary experiments with fixed initial CO_2 quantities showed that the overall conversion was limited by the CO_2 amount rather than the dissolution of $Mg(OH)_2$. Subsequent tests at constant P_{CO2} (excess CO_2 case) resulted in nearly complete conversion of $Mg(OH)_2$ to carbonate species.

The effect of reaction temperature dominated the kinetics and product phases of $Mg(OH)_2$ slurry carbonation as it relates to the metastability of the various hydrated carbonate species. The SEM images of Figure 5.2 reveal the very distinct

morphologies of the magnesium carbonates with different hydration levels. Solids were needle shaped at 30 ºC, rosette at 150 ºC, and cubic for carbonation at at 200 ºC. Figure 5.3(a) contains dTG traces for the solids recovered from the reactor after 90 min at each reaction temperature. The formation of nesquehonite (N†-120) at 30 ºC was confirmed given its charactersitc mass change regimes (Vágvölgyi *et al.*, 2008b; Ren *et al.*, 2013). First, the crystalized H_2O of nesquehonite begins to decompose (T < 100 ºC). The positioning of the three connected peaks in the dehydration zone is related to the difference in bonding capacity from one crystallized H_2O molecule to the next (Ren *et al.*, 2013). After H_2O was driven off, the remaining, structurally-weakened carbonate decomposed to CO_2 at temperatures above 300 ºC. Some argued that the minor dTG peak at 460 ºC (circled) was the result of the release of crystallized H_2O that was effectively trapped within the carbonates (Ren *et al.*, 2013). Hydromagnesite (HM†-120) was observed in the sample carbonated at moderate reaction temperature (~150 ºC), which led to two signature mass losses at ~230 ºC and ~400 ºC (Sawada *et al.*, 1978; Ren *et al.*, 2013). On the other hand, anhydrous magnesium carbonate, magnesite, was characterized by the single mass loss which peaked at 600 ºC (M†-120) indicating the absence of bulk crystalized H_2O or hydroxide.

To confirm the qualitative dTG observations, XRD patterns of the samples are included in Figure 5.3(b), where each carbonate phase has a characteristic pattern associated with its crystal structure. The sample produced at 30 ºC (N†-120) has peaks at 13º, 23º, and 29º, which are consistent with the nesquehonite phase (Downs, 2006). The sample carbonate at 150 ºC (HM†-120), the pattern shows the

charateristic peaks of hydromagnesite at 15º, 31º, and 14º (Downs, 2006). The sample reacted at the highest reaction temperature, 200 ºC (M†-120), produced magnesite as confrimed by its charactersitic XRD pattern having peaks at 33º, 43º, and 54º (Downs, 2006).

5.4. Effects of Reaction Time and Injection Temperature on $Mg(OH)_2$ Slurry Carbonation

Before examining the kinetics and mechanisms of the formation of nesquehonite, hydromagnesite, and magnesite from a $Mg(OH)_2$ slurry more closely, a series of tests at 150 ºC were performed to investigate the effect of reaction time (HM*-90, HM*-120, and HM*-180), CO_2 injection temperature (HM*-120 and HM-120), aging time (HM-1080), and CO_2 concentration (i.e. fixed CO_2 amount versus constant CO_2 pressure) (HM-120 and HM†-120) on the type of carbonate phase formed. Some have noted that reaction time influenced metastability of carbonate phases, particularly for very long aging time cases. Starting from dissolved magnesium and carbonate, hydromagnesite transitioned to magnesite in 5-15 hours under a CO_2 pressure of 3 bar and temperature of 120 ºC (Hänchen *et al.*, 2008). Essentially, given enough aging time, the thermodynamically stable phase, magnesite, will be favored over metastable phases, nesquehonite and hydromagnesite. Fluctuations between dissolution and precipitation, and thus, fluctuations in the solution pH bring the system to equilibrium over long periods of time (Deelman, 2001). Also, since the solubility of CO_2 and $Mg(OH)_2$ are higher at lower temperatures, a compounded effect on $Mg(OH)_2$ dissolution would be expected (Park *et al.*, 2003). Thus, the CO_2 injection temperature may have influenced the type of carbonate species formed initially,

which could in turn influence the reaction mechanism and phase formed for relatively short reaction time cases.

The dTG traces given in Figure 5.4, all show the two charactersitc mass drops of hydromagnesite, with the peak at ~400 °C and a smaller mass drop at ~230 °C (labeled HM on Figure 5.4(a)). Within the limits of parameter control and at the experimental conditions examined, the reaction time, CO_2 injection temperature, aging time, and CO_2 concentration appeared to have limited influence on the type of carbonate product phase. It should be noted that five of the six tests (HM*-90, HM*-120, HM*-180, HM-120, and HM-1080) were conducted with a fixed initial amount of CO_2, and therefore, an additional mass change event was observed, peaking at ~360 °C, which was the result of the dehydroxylation of unreacted $Mg(OH)_2$ (labeled B on Figure 5.4(a)). The carbonate sample produced at constant P_{CO2} (HM†-120) exhibited clean hydromagnesite decomposition mass change features, consistent with a highly pure material. Even when the reactor was held at 150 °C for 18 hours (HM-1080), the transition of hydromagnesite to magnesite was not witnessed in the $Mg(OH)_2$ slurry system. This dissimilarity from the literature (Hänchen *et al.*, 2008) could relate to the use $MgCl_2$ as magnesium source instead of $Mg(OH)_2$. Overall, the reaction temperature appeared to the most important factor affecting the formation of different carbonate phases in the $Mg(OH)_2$ slurry carbonation system as the formation of only metastable hydromagnesite was observed at 150 °C under the range of reaction time, CO_2 injection temperature, and CO_2 concentration conditions investigated in this study. Thus, the subsequent in-depth studies were performed for 120 min with constant CO_2 injected at reaction temperature to ensure complete

reaction and standardize the analysis. In order to independently investigate the formation of the dominant three magnesium carbonate species, low (30 °C), medium (150 °C), and high (200 °C) temperatures were selected for the rest of the study.

5.5. Kinetics and Mechanisms of Nesquehonite Formation from a $Mg(OH)_2$ Slurry

As previously discussed, low temperature $Mg(OH)_2$ slurry carbonation (N†-120), repeated three times, all resulted in the formation of only nesquehonite, magnesium carbonate with 3 moles of crystalized H_2O per mole $MgCO_3$. The formation of needle-like nesquehonite from aqueous solution at ambient temperature and atmospheric CO_2 pressure has been well documented in the past (Langmuir, 1965; Park & Fan, 2004; Zhang *et al.*, 2006; Hänchen *et al.*, 2008). Some even reported producing nesquehonite from aqueous solutions at temperatures up to 52 °C and at atmospheric CO_2 pressure (Davies & Bubela, 1973). But these studies were performed using Mg^{2+} solutions. Similar results were obtained when the starting material was $Mg(OH)_2$ in the slurry phase, where Mg^{2+} must have first been dissolved before carbonate precipitated. In the $Mg(OH)_2$ slurry carbonation system, a wide range of temperature (up to 65 °C) and P_{CO2} (15 atm at ambient temperature) conditions have been reported to produce nesquehonite (Botha & Strydom, 2001; Park *et al.*, 2003; Zhao *et al.*, 2010; Harrison *et al.*, 2013). Similarly, mineral tailing slurries containing brucite as the most active fraction carbonated to nesquehonite as well at 21 °C (Pronost *et al.*, 2011). While it is understood that the nesquehonite phase dominates at temperature and pressure conditions near ambient, the kinetics and mechanisms have not be studied completely.

As shown in Figure 5.5(a-1), the reaction between $Mg(OH)_2$ slurry and CO_2 was initially slow at 30 °C. The fraction of nesquehonite in the recovered solids stayed relatively low (the majority of the solids were $Mg(OH)_2$), until about 45 min into the reaction when the carbonation reaction took off. The lag time was likely related to the slower carbonation kinetics at the low reaction temperature and the solubility of nesquehonite under acidic conditions (i.e. Log K of proton enhanced dissolution equals 4.996, compared to magnesite's 2.294, at 25 °C) (Marini, 2007). The nucleation of a new phase may have delayed solid formation as well. After 45 min, the carbonation rate rapidly increased, and by 75 min, nearly all the solids were nesquehonite (near complete conversion marked with a dotted line). In a MgO slurry carbonation system, a similar jump in carbonation rate was witnessed, where they claimed that the increased precipitation rate was attributed to the release of H^+ when the magnesium bicarbonate solution decomposed to form nesquehonite (see Equation 5.7) (Smithson & Bakhshi, 1973).

Equation 5.7: $Mg^{2+}(aq) + 2HCO_3^-(aq) + 3H_2O$

$$\leftrightarrow MgCO_3 \cdot 3H_2O(s) + H^+(aq) + HCO_3^-(aq)$$

The continued release of H^+ ensured continued $Mg(OH)_2$ dissolution and maintained saturation levels. Similar parallel reactions seemed to occur in this study.

Most of the experimental data were quite reproducible, except that there was higher variability at the transition point (~60 min) for both solid Figure 5.5(a-1) and liquid Figure 5.5(a-2) analyses. As the reaction progressed, $Mg(OH)_2$ dissolution was occurring and Mg^{2+} concentration increased until the precipitation of nesquehonite dominated, pulling more Mg^{2+} out of solution than the dissolution could supply. Note

that under the experimental conditions, $Mg(OH)_2$ in equilibrium with 15 atm of CO_2, the solids would dissolve entirely, resulting in a Mg^{2+} concentration of 0.5 M. The high Mg^{2+} concentration was not achieved because dissolution was slow, which was likely the result of slow CO_2 hydration reactions and the faster nesquehonite precipitation reaction (as compared to $Mg(OH)_2$ dissolution). These parallel reactions resulted in a relative sharp change at 60 min (marked by dashed line). It is important to notice that after complete conversion of $Mg(OH)_2$ to $MgCO_3 \cdot 3H_2O$ (after 75 min, again marked with the dotted line), the Mg^{2+} concentration in the solution phase began to increase. This effect was driven by the solubility of nesquehonite, which was exacerbated as pH continued to be reduced in the reactor (e.g. a PHREEQC simulation showed nesquehonite's solubility to increase from 0.007 M to 0.266 M in the presence of 15 atm of CO_2) (De Visscher *et al.*, 2012).

The XRD time series patterns of the carbonated solids shown in Figure 5.6(a) echoed the quantitative analyses in Figure 5.5(a-1) and (a-2). Initially main peaks of brucite, at 38°, 18°, and 51°, dominated the XRD pattern. At 45 min, the beginnings of nesquehonite peaks at 13°, 23°, and 31° were observed (Downs, 2006). The sample taken at 60 min, when carbonation began to take place rapidly, still contained a significant amount of the brucite phase, though nesquehonite peaks were beginning to grow significantly. Going further, at 75 min the nesquehonite pattern was entirely recognizable with small residual peaks from the brucite phase, and by 90 min, only minimal brucite remained within the sample.

5.6. Kinetics and Mechanisms of Hydromagnesite Formation from a $Mg(OH)_2$ Slurry

Generally, hydromagnesite forms at temperatures above nesquehonite's stability. Some found nesquehonite to act as a precursor for the formation of sheet-like hydromagnesite (Hövelmann *et al.*, 2012), and numerous literature sources documented the transition temperature at approximately 52-60 °C in aqueous systems (Davies & Bubela, 1973; Fernández *et al.*, 2000; Botha & Strydom, 2001; Zhang *et al.*, 2006). Temperature may be the dominant driving force for the formation of hydromagnesite; however, the pH effect can also be significant. For example, high purity hydromagnesite was formed at 30 °C from a Mg-bearing solution derived from serpentine at low CO_2 pressure (1 atm) by increasing the pH to 9 via NaOH addition. Increasing the pH to 10 however resulted in the formation of large quantities of brucite (Teir *et al.*, 2007). Though possible to be formed at such low temperatures, hydromagnesite's metastability extends to significantly high temperatures given the material is thermally stable to 150 °C at least. Hänchen et al. found hydromagnesite to form at 120 °C and P_{CO2} of 3 bar (Hänchen *et al.*, 2008). Some observed a less common hydrated carbonate phase, dypingite ($Mg_5(CO_3)_4(OH)_2 \cdot H_2O$), in the temperature range of 23-40 °C (Pronost *et al.*, 2011; Hövelmann *et al.*, 2012), and others have shown its role in the transition between nesquehonite and hydromagnesite (Davies & Bubela, 1973; Hopkinson *et al.*, 2012).

To investigate the kinetics and mechanisms of Hydromagnesite formation, $Mg(OH)_2$ slurry carbonation experiments were performed at 150 °C (HM†-120). The carbonation rate, given as the growth of the hydromagnesite phase in Figure 5.5(b-1), was quite rapid. In the first 15 min of reaction, hydromagnesite represented 75% of

the sample mass (with the rest coming from $Mg(OH)_2$). Within 60 min $Mg(OH)_2$ was completely converted to hydromagnesite (dotted line). Again, the Mg^{2+} concentration experienced a relative maximum (marked by the dashed line), albeit a small broad peak. Figure 5.5(b-2) illustrates how the Mg^{2+} concentration was first growing, as $Mg(OH)_2$ was dissolved, and once conversion to hydromagnesite was near to completion, the concentration dropped due to the competition with precipitation. Subsequently the Mg^{2+} concentration rose again as the hydromagnesite approached equilibrium with the CO_2 rich solution derived from the excess CO_2 in the head space of the reactor. It is important to notice the relative scale as compared with Figure 5.5(a-1). The reduced solubility of hydromagnesite compared with nesquehonite must have been driven by the increased CO_2 solubility at low temperature (and thus lower pH) since hydromagnesite is generally the more soluble of the hydrated carbonates (e.g. Log K of proton driven dissolution is 4.996 and 30.854 for nesquehonite and hydromagnesite respectively at 25 °C and 1.013 bar total pressure) (Marini, 2007). The result was an increase in Mg^{2+} concentration at a slower rate than was observed in the study of 30 °C carbonation (N†-120).

The XRD pattern time series from the $Mg(OH)_2$ slurry carbonation test at 150 °C, given in Figure 5.6(b), show the transition between brucite and hydromagnesite with the latter dominating the former after 30 min of reaction. The brucite peaks at 38°, 18°, and 51° were present in the 15 min sample, though already smaller than the characteristic hydromagnesite peaks at 31°, 15°, and 14° (Downs, 2006). This result supported the carbon analyzer data given that only 25% of the sample was composed of $Mg(OH)_2$ after 15 min of reaction.

5.7. Kinetics and Mechanisms of Magnesite Formation from a $Mg(OH)_2$ Slurry

The most thermodynamically stable magnesium carbonate species is cube-like, anhydrous magnesite, $MgCO_3$. The metastability of hydrated carbonate phases can be altered by changing temperature, reaction time, or solution species concentration, which in turn leads to the faster formation of magnesite (Hänchen *et al.*, 2008). For instance, at CO_2 pressure of 3 bar and 120 °C, Hänchen et al. first produced hydromagnesite, which subsequently transitioned to magnesite over 5-15 hours (Hänchen *et al.*, 2008). At a P_{CO2} of 100 bar and 95 °C the critical saturation index for magnesite formation was between 0.25 and 1.14, and seeding the system resulted in faster nucleation of magnesite (Giammar *et al.*, 2005). Many examples in the literature show low temperature precipitation of magnesite in the range ~60-120 °C; however these studies utilized a very high P_{CO2}, and therefore, elevated levels of Mg^{2+} and CO_3^{2-} supersaturation (Deelman, 2001; Giammar *et al.*, 2005; Hänchen *et al.*, 2008). The co-precipitation of magnesite and hydromagnesite has also been observed in some instances (Hänchen *et al.*, 2008). As noted in the carbonation of dissolved serpentine at 150 bar of CO_2 pressure and temperatures in the rang 150-185 °C, direct aqueous carbonation can avoid or minimize a hydromagnesite intermediate, though these experiments utilized a buffer of 0.64 M $NaHCO_3$ and 1 M NaCl, which may have also impacted the experimental outcome (Wolf *et al.*, 2004).

In this study, slurry phase $Mg(OH)_2$ was carbonated at 200 °C (M†-120) to produce magnesite. Figure 5.5(c-1) and Figure 5.5(c-2) show the time series of the magnesite content embodied in the recovered solids as well as the Mg^{2+} concentration in solution. In Figure 5.5(c-1), the carbonation rate was observed to be slightly slower

than that of hydromagnesite formation at 150 °C. After 15 min of reaction, magnesite comprised ~60% of the sample (the rest being unreacted $Mg(OH)_2$). However, the chemical reaction reached completion faster in the magnesite formation experiment as the percentage leveled out at 90% magnesite after 45 min of reaction (dotted line), compared to ~60 min in the hydromagnesite case and ~80 min in the nesquehonite case. The conversion restriction may have been attributed to mass transfer limitations reducing the supply of Mg^{2+} as the $Mg(OH)_2$ particles were coated with $MgCO_3$ precipitates that formed a passivation layer. The slow $Mg(OH)_2$ dissolution combined with the fast carbonation kinetics at high temperature likely enabled conditions where $Mg(OH)_2$ reactant was encapsulated with magnesite. A comparable mass transfer limitation was observed in the gas-solid carbonation of $Mg(OH)_2$ (Butt *et al.*, 1996) and in the slurry phase carbonation of $Mg(OH)_2$ under acidified, and therefore fast kinetic, conditions (Zhao *et al.*, 2010). Limited conversion was also witnessed in the slurry carbonation of $Mg(OH)_2$ in a bubble column with relatively mild mixing condition at 15 atm CO_2 pressure and 160 °C, and in this case, the conversion of $Mg(OH)_2$ to carbonate was significantly lower (32% conversion was towards nesquehonite) (Park *et al.*, 2003). These phenomena were not observed in the studies of nesquehonite and hydromagnesite formation likely due to increased $Mg(OH)_2$ dissolution rates at lower temperatures and the lower pH driven by enhanced dissolution of CO_2.

The unreacted internal core was either MgO or a mixture of $Mg(OH)_2$ and MgO based on dehydroxylation and calcination tests in the TGA. In the liquid phase, the Mg^{2+} concentration depicted in Figure 5.5(c-2) was significantly lower than the

previous carbonation tests at 30 °C and 150 °C due to the decreased CO_2 solubility at high temperature and magnesite's low solubility. As witnessed in the previous studies, a peak in Mg^{2+} concentration (marked by the dashed line) was attributed to the parallel dissolution of $Mg(OH)_2$ and carbonate forming reactions. After the maximum conversion to magnesite was achieved (marked by a dotted line), the Mg^{2+} concentration exhibited a slow decline to nearly zero. As compared to the previous lower temperature studies (Figure 5.5(a-2) and Figure 5.5(b-2)), the Mg^{2+} concentration profile after carbonation reaction in the presence of excess P_{CO2} decreased slightly instead of increasing. The difference was attributed to low magnesite solubility as well as low CO_2 solubility at elevated temperature.

From the XRD in Figure 5.6(c), the general trend was similar to the hydromagnesite formation experiments in that the brucite peaks were generally replaced with magnesite peaks at 33°, 43°, and 54° as the reaction proceeded. It is possible that MgO was present in small quantities, though not very visible on XRD. MgO has characteristic peaks at 43° and 63° (Downs, 2006). The peak at 43° would be dwarfed by the magnesite peak at that location, while a slight peak at 63° did exist in some of the patterns. Another takeaway from the XRD was the presence of hydromagnesite in the 15 min sample. Though short lived, the presence of hydromagnesite supported the hypothesis that magnesite formation in the $Mg(OH)_2$ slurry carbonation system moved through a hydrated intermediate which possibly facilitated the reaction. The formation of hydromagnesite as an intermediate could explain why the unreacted core was MgO, since the hydrated carbonate formation could siphon the hydroxide from $Mg(OH)_2$.

5.8. Fate of Magnesium in $Mg(OH)_2$ Slurry Carbonation at Different Temperatures

A summary of the temperature effect on the carbonation of $Mg(OH)_2$ in the slurry phase is given in Figure 5.7 as the fraction of magnesium within the system that was present in different states. As mentioned previously, $Mg(OH)_2$ carbonation at different temperatures resulted in the formation of different metastable and stable carbonate phases, with nesquehonite preferred at 30 °C (N†-120), hydromagnesite at 150 °C (HM†-120), and magnesite at 200 °C (M†-120). The fraction of Mg present as aqueous Mg^{2+} ions decreased with temperature increased, consistent with the increased solubility of carbonates at lower temperature which was driven by the excess CO_2 and improved CO_2 dissolution at low temperature. The experiments at 200 °C each resulted in incomplete conversion to magnesite with a remaining unreacted fraction of magnesium bearing MgO or $Mg(OH)_2$. In all cases, the magnesium carbonate produced was a pure phase, not a mixture of carbonate phases, after 120 min.

5.9. Effect of Additives on $Mg(OH)_2$ Slurry Carbonation

As discussed earlier the affinity between H_2O and Mg^{2+} results in the formation of metastable hydrated carbonate species. To promote the production of anhydrous carbonate at temperatures where it is not known to form, various techniques have been proposed. Thus, the effect of various additives on aqueous carbonation kinetics and their ability to preferentially form the magnesite phase was investigated at 150 °C where the dominant carbonate species was hydromagnesite. First, the use of an acid (e.g. HCl) to promote $Mg(OH)_2$ dissolution was suggested. Zhao et al. found that an

acidified $Mg(OH)_2$ slurry experienced fast initial kinetics, due to rapidly producing Mg^{2+}, however this effect was followed by low overall conversion potentially due to fast kinetics resulting in quicker formation of carbonate passivation layers (Zhao *et al.*, 2010). The addition of bicarbonate also increased the carbonation rate by overcoming rate-limiting CO_2 hydration reactions as well as enhancing $Mg(OH)_2$ dissolution via the ligand effect of HCO_3^- (Hövelmann *et al.*, 2012). Another approach is to reduce the activity of H_2O by adding salts (e.g. NaCl) and polymers (e.g. monoethylene glycol) (Sayles & Fyfe, 1973; Möller, 1989; Sandengen *et al.*, 2008). This interruption in the hydration shell of Mg^{2+} could lead to the direct formation of magnesite at lower temperatures and pressures by allowing close direct interaction between CO_3^{2-} and Mg^{2+}. NaCl also effected the carbonation system by contributing Cl^-, which complexed with Mg^{2+} and aided in $Mg(OH)_2$ dissolution (O'Connor *et al.*, 2004), though its presence does reduce CO_2 solubility (Duan *et al.*, 2006). But most of these studies were performed at either low temperatures (room temperature with P_{CO2} = 15 atm) (Zhao *et al.*, 2010) or low P_{CO2} (P_{CO2} = 1 atm for reaction temperature in the range 23-126 °C) (Sayles & Fyfe, 1973; Hövelmann *et al.*, 2012).

In this study, four different additives were evaluated for the carbonation of a $Mg(OH)_2$ slurry at 150 °C with CO_2 limited conditions: 1.4 wt% HCl (HM-120-HCl), 1 M NaCl (HM-120-NaCl), 0.5 M HCO_3^- (HM-120-$NaHCO_3$), and 1 M NaCl + 0.5 M HCO_3^- (HM-120-NaCl/$NaHCO_3$). Since a fixed amount of CO_2 was initially charged to the reactor, the experiment labeled "No Additive" (HM-120) experienced a limited conversion of ~80% to hydromagnesite in terms of $Mg(OH)_2$. But the conversion was

~100% in terms of CO_2. Figure 5.8(a) contains the dTG traces of each experiment after 90 min of reaction. Any mass changes above ~460 °C corresponded to the decomposition of anhydrous magnesium carbonate species. The main weight drops for all samples (peaking at ~400 °C) and smaller mass drop at ~230 °C, were characteristic hydromagnesite decompositions. The samples with added NaCl or HCO_3^- added all exhibited some magnesite, and the sample produced in the presence of both NaCl and HCO_3^- showed the most significant magnesite formation. Interestingly, the sample produced under acidic conditions had a unique mass change profile, though XRD analysis confirmed the dominance of hydromagnesite in the sample.

The dTG results were confirmed by the total carbon analysis. Carbon percentage in solids was used since some additives resulted in the formation of both hydromagnesite and magnesite. Complete conversion to hydromagnesite would translate to 10.1% carbon in the sample (dashed line in Figure 5.8(b)), but anything above ~8% carbon (the roughly 80% conversion to hydromagnesite experienced by the base case) was an improvement. Despite the literature findings, the acidified case experienced slower kinetics, though it reached almost 100% conversion to hydromagnesite. This could mean that system was not necessarily carbonate limited as the base case suggested, and perhaps there was some passivation layer formation. NaCl allowed for some magnesite to form, likely by disrupting the hydration shell of Mg^{2+}. The overall kinetics in terms of solid carbon percent were effectively unaltered, and mass transfer limitations probably caused the limited overall conversion. The experiments with bicarbonate experienced faster kinetics and higher overall

conversion, due to the presence of aqueous carbonate species and additional carbon in a carbon-limited batch system, respectively. Both cases formed magnesite, as evidenced by the increase in carbon percentage beyond the theoretical limit of hydromagnesite. The synergistic effect of NaCl and HCO_3^- produced the most magnesite, and therefore, the highest overall conversion to carbon containing solids.

5.10. Summary

In general, anhydrous carbonate is desired in terms of carbon efficiency as well as carbon storage permanence. It has been argued that the formation of magnesite required high reaction temperature. In this study, various parameters were investigated to determine reaction kinetics and type of carbonate species formed as slurry phase $Mg(OH)_2$ reacted with CO_2. The $Mg(OH)_2$ slurry carbonation system is governed by the metastability of the hydrated magnesium carbonates. As illustrated in Figure 5.9, the effect of temperature on carbonate phase formation was significant. By setting the temperature, it was possible to selectively produce a specific carbonate phase, though kinetics and equilibrium Mg^{2+} concentration varied also with temperature. At low temperature (30 °C), nesquehonite formed with relatively slow reaction kinetics, and a significant fraction of nesquehonite was dissolved after reaction by the excess P_{CO2}, which lowered the pH. At moderate temperatures (~150 °C) and under a variety of experimental parameter changes, including reaction time, CO_2 injection temperature, aging up to 18 hours, and CO_2 concentration (fixed amount of CO_2 or constant CO_2 pressure), the metastable hydromagnesite phase was produced very quickly. In this temperature regime, it was also found that solution

additives can stimulate the formation of stable, anhydrous magnesite. The combination of 0.5 M bicarbonate and 1 M NaCl resulted in the most favorable carbonation conditions due to enhanced carbonation rate, dissolution rate, and/or interference with the ability of H_2O to incorporate within the carbonate crystal. At high temperature (200 °C) magnesite was produced quite rapidly, with some evidence of a hydromagnesite intermediate. Further evaluation of additives to sustainably drive formation of magnesite at even lower temperatures would be interesting for future study.

Notation

CCS	Carbon capture and storage
B	Magnesium hydroxide, Brucite ($Mg(OH)_2$)
N	Nesquehonite ($MgCO_3 \cdot 3H_2O$)
HM	Hydromagnesite ($Mg_5(CO_3)_4(OH)_2 \cdot 4H_2O$)
M	Magnesium carbonate, Magnesite ($MgCO_3$)
HCO_3^-	Bicarbonate ion
$NaHCO_3$	Sodium bicarbonate
NaCl	Sodium Chloride
HCl	Hydrochloric Acid
CSTR	Continuously stirred tank reactor
TGA	Thermogravimetric Analyzer
dTG	Differential thermogravimetry
XRD	X-ray diffraction
cps	Counts per second (XRD)
ICP-OES	Inductively coupled plasma optical emission spectrometer
SEM	Scanning Electron Microscope
T	Temperature
P_x	Partial pressure of species X
$P_{o,x}$	Initial partial pressure of species X

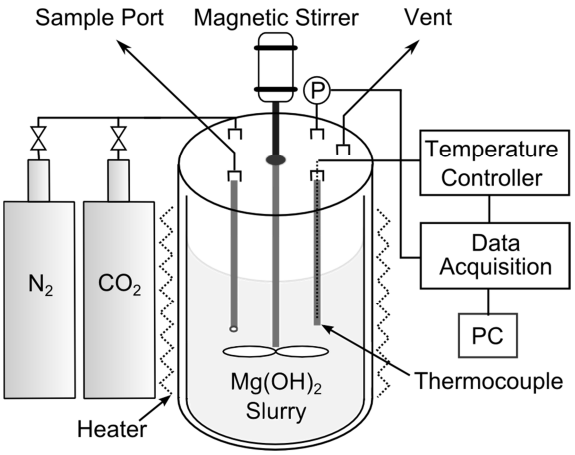

Figure 5.1: Schematic diagram of the CSTR for high temperature and pressure carbonation of $Mg(OH)_2$ slurry.

Table 5.1: Reaction conditions for $Mg(OH)_2$ slurry carbonation. Fixed experimental variables: 8.75 g $Mg(OH)_2$, 2.9 wt% $Mg(OH)_2$ slurry concentration, and initial CO_2 amount (unless noted by †). Beginning of Sample ID signifies the phase formed (nesquehonite (N), hydromagnesite (HM), and magnesite (M)). The number in the Sample ID indicates the reaction time.

Sample ID	Reaction Temperature (ºC)	Temperature at CO_2 injection (ºC)	Reaction Time (min)	Additives
N†-120	30	30	120	-
HM*-90	140	25	90	-
HM*-120	140	25	120	-
HM*-180	140	25	180	-
HM†-120	150	150	120	-
HM-120	150	150	120	-
HM-1080	150	150	1080	-
HM-120-HCl	150	150	120	1.3 wt% HCl
HM-120-NaCl	150	150	120	1 M NaCl
HM-120-$NaHCO_3$	150	150	120	0.5 M $NaHCO_3$
HM-120-NaCl/$NaHCO_3$	150	150	120	1 M NaCl/0.5 M $NaHCO_3$
M†-120	200	200	120	-

* Injection at 25 ºC instead of given reaction temperature
† Constant P_{CO2} throughout experiment (15 atm), experiment repeated three times

(a) 30 ºC

(b) 150 ºC

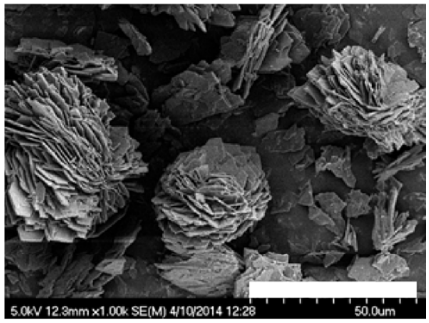

(c) 200 ºC

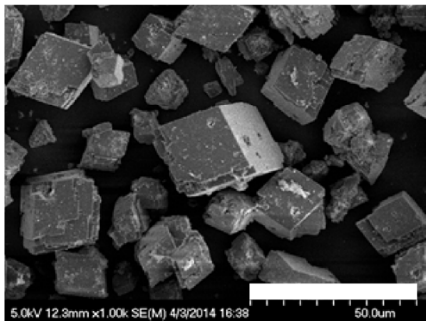

Figure 5.2: SEM images of solid products from $Mg(OH)_2$ slurry carbonation at (a) 30 ºC (N†-120), (b) 150 ºC (HM†-120), and (c) 200 ºC (M†-120).

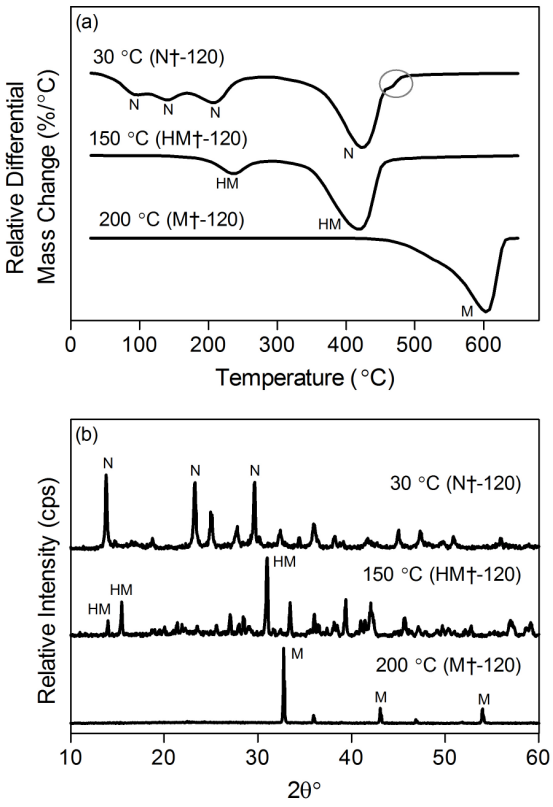

Figure 5.3: The effect of reaction temperature, in the range 30-200 ºC, on the product phase formed during slurry phase carbonation of $Mg(OH)_2$ for 90 minutes with a constant P_{CO2} = 15 atm: (a) dTG traces and (b) XRD patterns. Labels on XRD patterns correspond with characteristic peak positions for nesquehonite (N), hydromagnesite (HM), and magnesite (M).

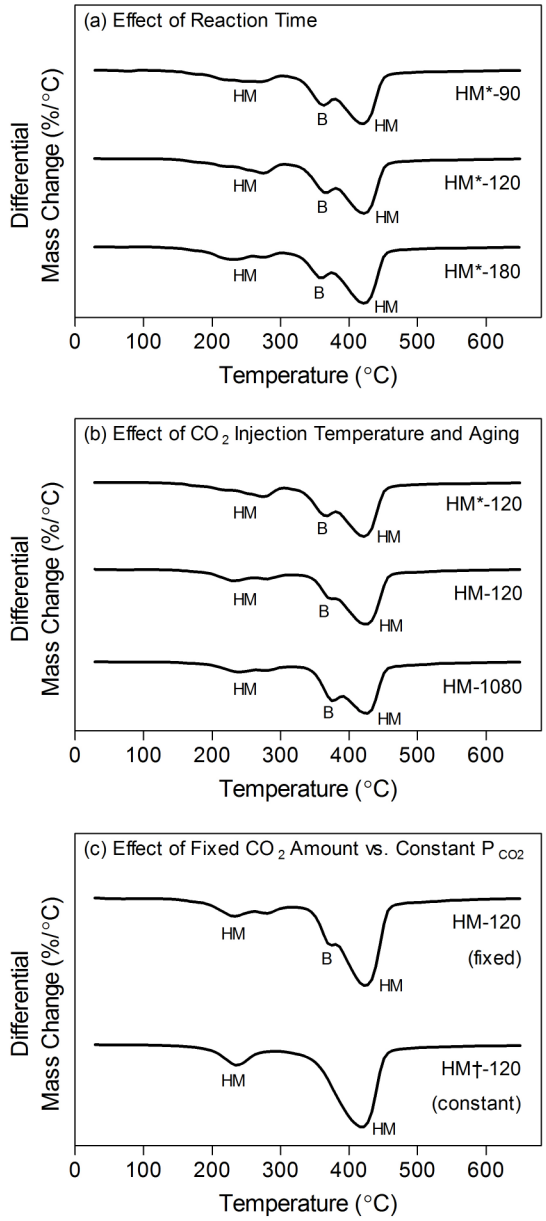

Figure 5.4: Effects of (a) reaction time, (b) CO_2 injection temperature and aging, and (c) fixed CO_2 amount vs. constant P_{CO2} on the formation of hydromagnesite at 150 ºC.

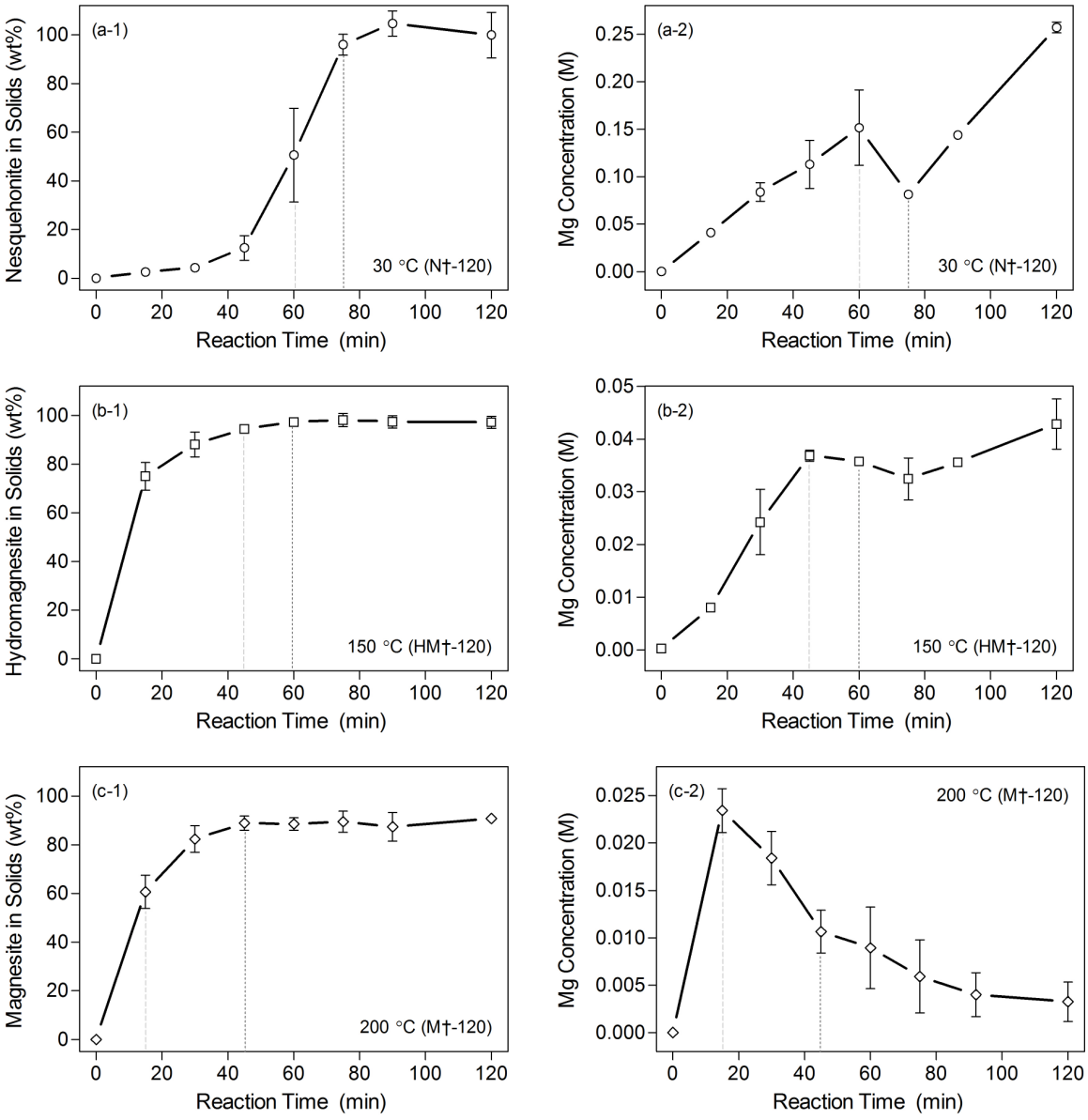

Figure 5.5: Reaction progress in $Mg(OH)_2$ slurry carbonation with constant P_{CO2} = 15 atm at low temperature (30 ºC, N†-120), medium temperature (150 ºC, HM†-120), and high temperature (200 ºC, M†-120): (a-1, b-1, c-1) fraction of carbonate phase in recovered solids and (a-2, b-2, c-2) concentration of Mg^{2+} in liquid phase.

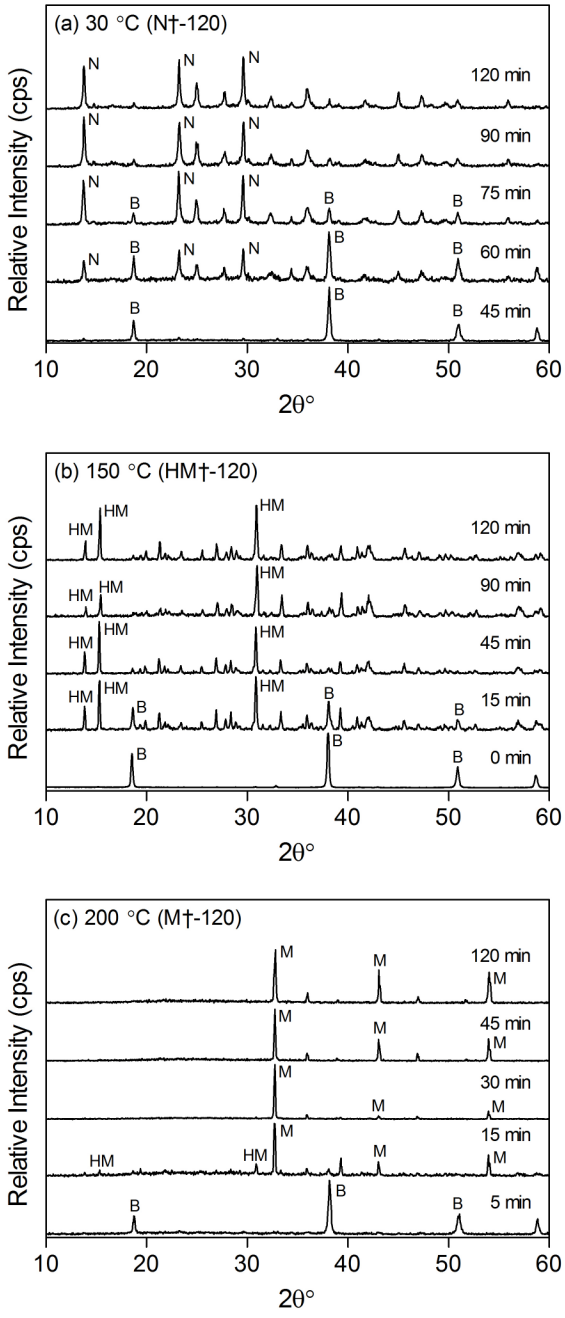

Figure 5.6: XRD pattern time-series depicting the formation of carbonate phases (nesquehonite-N, hydromagnesite-HM, and magnesite-M) during $Mg(OH)_2$ slurry carbonation with constant P_{CO2} = 15 atm CO_2 at (a) 30 ºC, (b) 150 ºC, and (c) 200 ºC.

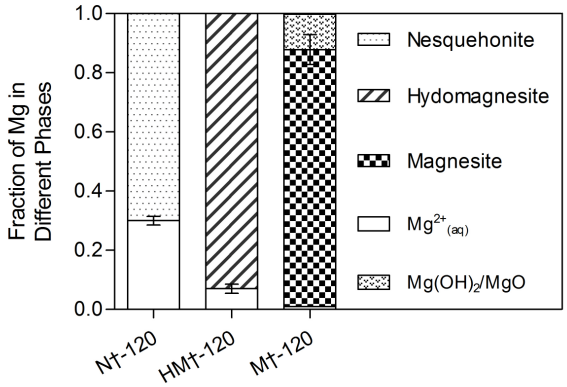

Figure 5.7. Fate of magnesium in both the liquid and solid phase during the slurry phase carbonation of $Mg(OH)_2$. Representative fractional composition obtained after 120 minutes (T = 30, 150, 200 °C and constant P_{CO2} of 15 atm).

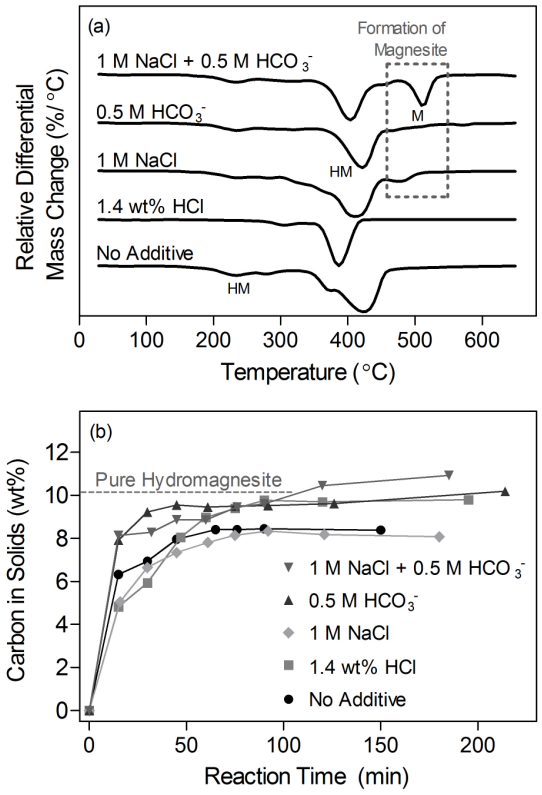

Figure 5.8: Effect of additives on $Mg(OH)_2$ slurry carbonation performed at 150 °C with a fixed amount of CO_2 in system ($P_{o,CO2}$ = 15 atm): (a) dTG traces of solid samples taken at 90 min and (b) fraction of carbonates in the recovered solids as a function of time.

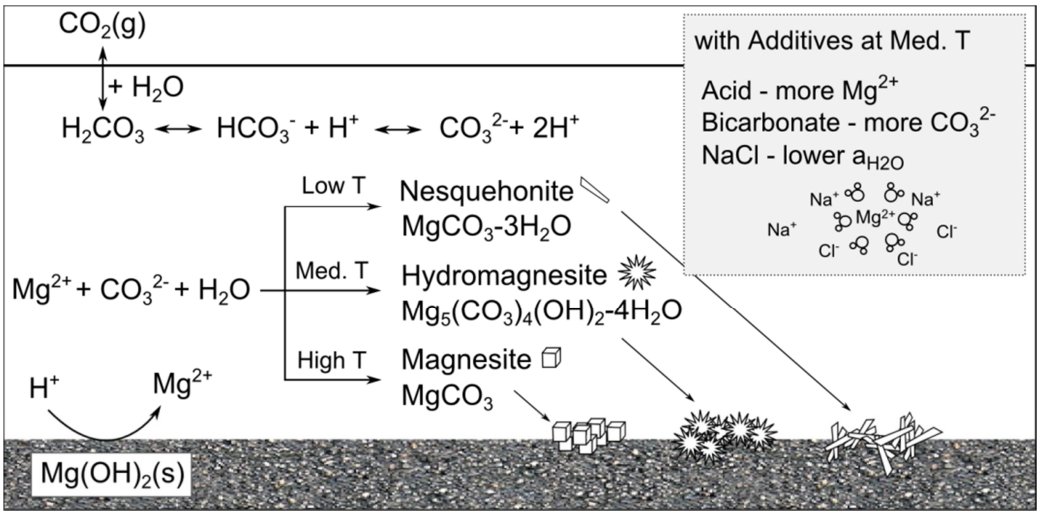

Figure 5.9: Summary of slurry phase $Mg(OH)_2$ carbonation.

5.11. Supporting Information

5.11.1. Solubility Modeling

Table 5.2: Solubilities of $Mg(OH)_2$ and nesquehonite obtained via geochemical modeling package PHREEQC. Fixed parameters: T = 30 °C, P_{CO2} = 15 atm, pH_i = 7, water amount = 0.3 kg, equilibrium phase = 0.15 mol $Mg(OH)_2$ or nesquehonite.

	Input	**Output**		
Simulation Purpose	**Initial M_{Mg} (mol/kg)**	**Final M_{Mg} (mol/kg)**	**Dissolved Mg (mol)**	**pH_f**
$Mg(OH)_2$ Solubility	0.00016 *	0.4999	0.15	7.476
Nesquehonite Solubility	0.007 **	0.2661	0.08	7.245

* from $K_{SP,Mg(OH)2} = 1.5 \times 10^{-11}$
** (De Visscher *et al.*, 2012)
i = initial, f = final

6. Directed Precipitation of Hydrated and Anhydrous Magnesium Carbonates for Carbon Storage

The contents of this chapter are to be submitted for publishing in the Royal Society of Chemistry's *Physical Chemistry Chemical Physics*. KJF assisted with literature review and literature modeling, performed slurry carbonation experiments, analyzed recovered liquids and solids, and assisted in writing manuscript (Swanson *et al.*, 2014).

6.1. Introduction

Carbon mineralization is a thermodynamically stable and environmentally benign CO_2 storage method. Significant research has been focused on the accelerated dissolution and carbonation of magnesium silicate minerals using captured CO_2. Recently, an indirect mineral carbonation scheme has been proposed where Mg-bearing sorbent ($Mg(OH)_2$) is produced from silicate minerals for subsequent carbonation, which can be integrated into various energy conversion processes. The use of Mg-bearing sorbents, slurries, or liquids is attractive because it can allow to both capture and store CO_2 without the need for the sorbent/solvent regeneration, thus creating a comprehensive CO_2 mitigation solution.

For large-scale carbonation of Mg-bearing materials to be a viable industrial process, the kinetics of anhydrous magnesium carbonate ($MgCO_3$, magnesite) precipitation must be significantly accelerated. Magnesite is the most stable and efficient carbon storage medium of the magnesium carbonates due to highest Mg efficiency, lowest process water requirement, and great chemical stability suitable for long-term storage. In the case of the indirect carbon mineralization scheme, the aqueous carbonation of $Mg(OH)_2$ is relatively fast but the solid products are generally hydrated magnesium carbonate, e.g. nesquehonite

($MgCO_3 \cdot 3H_2O$) or hydromagnesite ($Mg_5(CO_3)_4(OH)_2 \cdot 4H_2O$), rather than anhydrous magnesite which is desired. The phases of magnesium carbonate that can be formed during carbon mineralization are summarized in Table 6.1 (Raade, 1970; Hänchen *et al.*, 2008; Vágvölgyi *et al.*, 2008a; Vágvölgyi *et al.*, 2008b). In general, the hydrated magnesium carbonates have a higher solubility, making them less effective for long-term storage of CO_2. In addition, the hydrated carbonates include added weight of water and possibly hydroxide, making them less efficient in terms of both transportation cost and stoichiometric utilization of Mg. Therefore, the combined CO_2 capture and storage schemes forming hydrated carbonate species may be less robust and likely cost more to operate over time.

The thermodynamics of these potential carbonate products have been extensively investigated in the literature, and it is well established that the anhydrous carbonate, magnesite, is the most stable and has the lowest solubility product under most reaction conditions (Kittrick & Peryea, 1986; Hänchen *et al.*, 2008; Krupka *et al.*, 2010; Schaef *et al.*, 2011). As shown in Figure 6.1, magnesite has the lowest equilibrium Mg^{2+} concentration as compared with the metastable carbonate species. Brucite ($Mg(OH)_2$) can potentially have a lower solubility, though only at high temperatures and very low CO_2 fugacity. Despite the fact that magnesite is the most stable magnesium carbonate phase over all relevant reaction conditions, it is seldom the main product reported in the literature. Instead the metastable hydrated magnesium carbonate species are known to form readily and persist for long periods of time.

The formation of magnesium carbonate phases becomes more complicated if the sources of Mg^{2+} or bicarbonate and carbonate ions are varied as well as other reaction

parameters. Table 6.2 and Table 6.3 list a large number of studies on the formation of different magnesium carbonate phases, where the Mg was derived from a magnesium salt (Davies & Bubela, 1973; Sayles & Fyfe, 1973; Ming & Franklin, 1985; Kittrick & Peryea, 1986; Kloprogge *et al.*, 2003; Giammar *et al.*, 2005; Zhang *et al.*, 2006; Dong *et al.*, 2008; Hänchen *et al.*, 2008; Vágvölgyi *et al.*, 2008a; Vágvölgyi *et al.*, 2008b; Cheng & Li, 2009; Ferrini *et al.*, 2009; Ballirano *et al.*, 2010; Cheng & Li, 2010; Krupka *et al.*, 2010; Sutradhar *et al.*, 2011) or hydroxide (Smithson & Bakhshi, 1973; Botha & Strydom, 2001; Park *et al.*, 2003; Mitsuhashi *et al.*, 2005; Xiong & Lord, 2008; Zhao *et al.*, 2010; Schaef *et al.*, 2011; Hopkinson *et al.*, 2012; Harrison *et al.*, 2013). As reported, magnesite was rarely reported as the main product and the data is widely scattered (to be discussed in detail in a latter section). Generally, the formation of magnesite with adequate rates required relatively high temperatures (> 100 °C), significant CO_2 partial pressure (~100 bar), and/or long reaction times (Möller, 1989; Botha & Strydom, 2001; Hänchen *et al.*, 2008; Xiong & Lord, 2008; Hopkinson *et al.*, 2012; Fricker & Park, 2013). The metastable hydrated phases tend to form first and, given enough time, will slowly transform into the anhydrous magnesite (Hänchen *et al.*, 2008). At lower reaction temperature and CO_2 pressure, magnesite formation was promoted with longer reaction times (~300-900 min) (Smithson & Bakhshi, 1973; Hänchen *et al.*, 2008), the addition of salts (e.g. $NaNO_3$ or NaCl) to interfere with the attraction between Mg and water molecules in its hydration shell (Sayles & Fyfe, 1973), or the addition of polymers to reduce the ambient water activity (Sandengen *et al.*, 2008).

In this study, $Mg(OH)_2$ was selected as the Mg-bearing material for indirect CO_2 capture and storage. The relevant reactions of $Mg(OH)_2$ carbonation include CO_2

dissolution and hydration to carbonate and bicarbonate ions (Equation 6.1), Mg^{2+} production by proton enhanced $Mg(OH)_2$ dissolution (Equation 6.2), and magnesium carbonate precipitation (Equation 6.3).

Equation 6.1: $CO_2(aq) + H_2O \leftrightarrow HCO_3^-(aq) + H^+(aq) \leftrightarrow CO_3^{2-}(aq) + 2H^+(aq)$

Equation 6.2: $Mg(OH)_2(aq) + 2H^+(aq) \leftrightarrow Mg^{2+}(aq) + 2H_2O$

Equation 6.3: $Mg^{2+}(aq) + CO_3^{2-}(aq) \leftrightarrow$ Magnesium Carbonate(s)

Among different carbonate phases, magnesite is possibly the most studied one, with both the precipitation and dissolution rate kinetics being widely investigated, although some of the studies were performed under simulated natural weathering conditions (mild reaction conditions) (Pokrovsky & Schott, 1999; Pokrovsky *et al.*, 1999; Saldi *et al.*, 2009; Saldi *et al.*, 2010; Bénézeth *et al.*, 2011; Saldi *et al.*, 2012). The dissolution and precipitation rates of brucite ($Mg(OH)_2$ have also been investigated (Pokrovsky & Schott, 2004; Pokrovsky *et al.*, 2005), however, only at conditions close to room temperature. Work on the precipitation kinetics of hydrated magnesium carbonates were even more limited (Cheng & Li, 2010). Thus, the relationship between the formation kinetics of various magnesium carbonate phases is not well understood.

The difficulty in precipitating magnesite is likely caused by a combination of slow nucleation and crystal growth rates for magnesite when compared with the hydrated carbonates. Magnesite nucleation is known to be rate-limiting, requiring adequate time and critical level of supersaturation (between 0.25 and 1.14) for significant formation of $MgCO_3$ (experiments conducted at CO_2 pressure of 100 bar and 95 °C) (Giammar *et al.*, 2005). In order to overcome the kinetic limitations in the formation of magnesite, this

study investigated the use of seed particles (both magnesite and alumina) to direct the precipitation of magnesite under industrially relevant conditions. Examples of seeded Mg carbonation systems are limited in the literature. Faster nucleation rates and shorter induction times have been observed in some seeded magnesite precipitation systems (Sheila & Khangaonkar, 1989; Giammar *et al.*, 2005). Furthermore, the use of seeds in the precipitation of calcium carbonate have been found to provide precise control over product particle morphology (Donnet *et al.*, 2005).

In this study, magnesium carbonates were produced from the reaction of a $Mg(OH)_2$ slurry with CO_2 gas in a pressurized batch reactor. The reaction parameters that affect the type of carbonate phase formed as well as the rate with which they form were explored. In particular, the effect of seed particles with different chemistries (i.e. existing carbonate phase versus inert dissimilar phase) on the formation of magnesite was investigated. The available surface area for the growth of this desirable phase was considered. As illustrated in Figure 6.2, it is expected that the absence of magnesite seed particles or the presence of inert seed particles will lead to the growth of a hydrated metastable phase of magnesium carbonates, while seeding with magnesite particles will lead to the growth of additional magnesite.

6.2. Materials and Methods

6.2.1. Seed Particles

A single batch of magnesite seed particles were synthesized within the high pressure continuously stirred tank reactor (CSTR) (Pressure Products Industries, Warminster, PA)

depicted in Figure 6.3. A slurry of hydromagnesite (30 wt%) prepared in deionized H_2O was contained within a glass liner inside the CSTR. CO_2 was introduced into the reactor headspace at a pressure of 30 atm and was held constant throughout the synthesis procedure. After pressurization, the CSTR was heated to 200 °C at approximately 3.4 °C/min and held there for 4 hr. After the reactor was cooled, the slurry was filtered (2.5 μm filter) and the recovered solids were dried under vacuum at 70 °C overnight. The average diameter of the resulting magnesite seed particles was ~2-4 μm and they had a surface area equal to 1.24 m^2/g.

Figure 6.4 shows SEM images of the three solids used in this study. Figure 6.4(a) displays $Mg(OH)_2$ that was used as a source of magnesium ions. The alumina particles (CT1200, Alamatis, Leetsdale, PA) used as an inert seeding material are shown in Figure 6.4(b). The alumina particles were selected for their similar morphology (surface area: 1.11 m^2/g) to the magnesite seed particles. It should be noted that the mean diameter of the primary particles in the alumina used was ~1.4 μm, and the structures shown in the SEM image were actually agglomerates that were expected to disperse in solution. Figure 6.4(c) shows the magnesite seed particles synthesized above.

6.2.2. Seeded Carbonation of $Mg(OH)_2$ in Batch Reactor

$Mg(OH)_2$ carbonation in the slurry phase was investigated in a CSTR described previously (Figure 6.3). Within the reactor, a 300 mL glass liner was placed to contain the reaction materials and the slurry was stirred vigorously at 700 rpm. The $Mg(OH)_2$ slurry concentration was held constant at 2.9 wt% throughout all experiments, which comprised 8.75 g dry $Mg(OH)_2$ (Acros Organics, Geel, Belgium) dispersed in 300 mL

deionized H_2O. Seeded experiments included either 5.34 g of anhydrous magnesite ($MgCO_3$) particles, which translated to 30 mol% of the total solids in the slurry, or 5.97 g of alumina particles (manufactured). The mass of alumina particles was chosen to match the surface area of the magnesite seeds. After sealing the CSTR, but prior to experimentation, high-purity nitrogen (N_2) was used to purge the reactor headspace for 10 min. The reactor was heated to the reaction temperature (80-150 °C), and once pressure was stable, the experiment was initiated by opening a valve connected to a 15 atm carbon dioxide (CO_2) source. The valve remained open throughout the experiment (120 min) in order to maintain a constant CO_2 pressure. A data acquisition board connected with internal thermocouples and a pressure transducer (Omega, Stamford, CT) provided an online record of the experimental conditions.

A slurry sampling system was constructed from valves and a dip tube to extract small (approximately 2 mL each) slurry samples from the bulk fluid. Samples were taken at 15 min intervals at most to ensure no significant alteration of liquid contents over the entire experimental run. After passing through an 11 μm filter to recover solids, liquid filtrate (200 μL) was combined with 2 wt% nitric acid to stop further reactions. The Mg^{2+} concentration was measured via an inductively coupled plasma optical emission spectrometer (ICP-OES) (ACTIVA-M, Horiba Jobin Yvon, Inc.)**.** Solids recovered as filter cake were dried overnight at 70 °C under vacuum before a series of subsequent analyses by thermogravimetric analysis (TGA), X-ray diffraction (XRD), and carbon analysis (CA).

6.2.3. Solid Characterization

Starting materials and solid products were imaged with a field emission scanning electron microscope (S-4700 FE-SEM, Hitachi, Ltd.) using an acceleration voltage of 5 kV to investigate the morphology. Product phases were identified from XRD patterns obtained using CuKα radiation (λ = 1.5406 Å) (XRG 3000, Inel Inc.). Solid products were also analyzed by TGA (SETSYS Evolution, Setaram Instrumentation) and CA (CO_2 Coulometer, UIC, Inc.) in order to determine the conversion of $Mg(OH)_2$ into different magnesium carbonate phases, mainly either hydromagnesite (HM) or magnesite (M). More details regarding the conversion calculation methodology can be found in Section 6.5.

6.3. Aqueous Carbonation of Magnesium Literature

At the outset of this study, an extensive literature review was performed to identify the optimal conditions for magnesite formation. The literature was categorized into studies that used a salt of magnesium as the magnesium source, and those that began with magnesium hydroxide slurry. Those that started with a magnesium salt were much more diverse in terms of reaction parameters: starting material, temperature, and carbon source. These studies are summarized in Table 6.2, where they have been ordered according to the phase of magnesium carbonate produced: hydromagnesite (Zhang *et al.*, 2006; Hänchen *et al.*, 2008; Vágvölgyi *et al.*, 2008a; Cheng & Li, 2010), lansfordite (Ming & Franklin, 1985), magnesite (Hänchen *et al.*, 2008) and nesquehonite (Davies & Bubela, 1973; Ming & Franklin, 1985; Kloprogge *et al.*, 2003; Zhang *et al.*, 2006; Dong *et al.*, 2008; Hänchen *et al.*, 2008; Vágvölgyi *et al.*, 2008b; Cheng & Li, 2009; Ferrini *et al.*,

2009; Ballirano *et al.*, 2010; Krupka *et al.*, 2010; Sutradhar *et al.*, 2011). The group of studies that started with magnesium hydroxide were slightly less variable in reaction conditions, but the same four carbonate products were reported: hydromagnesite (Möller, 1989; Botha & Strydom, 2001; Xiong & Lord, 2008; Hopkinson *et al.*, 2012), lansfordite (Smithson & Bakhshi, 1973), magnesite (Sayles & Fyfe, 1973; Schaef *et al.*, 2011), and nesquehonite (Smithson & Bakhshi, 1973; Park *et al.*, 2003; Mitsuhashi *et al.*, 2005; Zhao *et al.*, 2010; Schaef *et al.*, 2011; Hopkinson *et al.*, 2012; Harrison *et al.*, 2013) (Table 6.3). While there are likely more reports of magnesium carbonate precipitation in the literature, this search was limited to those that were most relevant and contained sufficient data for modeling the reaction conditions.

In an attempt to reconcile the differences in experimental conditions that were used in each of the above referenced studies so that they could be compared on a consistent basis, the reaction conditions of each experiment was modeled using the geochemical modeling package, PHREEQC (Parkhurst & Appelo, 2013). When pure CO_2 gas was bubbled through a solution, the partial pressure was assumed to be 101.325 kPa, while those that did not use CO_2 directly were assumed to take place in the presence of 400 ppm CO_2. From the PHREEQC simulations, a maximum saturation index was calculated for each experimental condition reported. Given in Equation 6.4, the saturation index (Ω) is defined as the logarithm of the ion activity product (IAP) divided by the solubility product constant (K_{SP}) of the phase of interest, in this case magnesite. On this scale, $\Omega = 0$ for a saturated solution, $\Omega > 0$ for a supersaturated solution, and $\Omega < 0$ for an undersaturated solution.

Equation 6.4: $\Omega = \log(\frac{IAP}{K_{SP}})$

The results of the PHREEQC simulations are given in the last column of Table 6.2 and Table 6.3, in addition to being represented graphically in Figure 6.5. Those experiments starting with a magnesium salt are shown in Figure 6.5(a), and those starting with magnesium hydroxide are in Figure 6.5(b). It should be noted that, in recreating these experiments via simulations, the kinetics associated with precipitation could not be considered. All of the experiments were modeled as an equilibrium system, so the saturation index calculated for each experiment was the maximum that could be achieved given the reagents and reaction conditions used.

The comparison of literature experiments in Figure 6.5 illustrates a few general trends in the magnesium carbonate literature. When it was formed, lansfordite only appeared at low temperatures. Nesquehonite was quite common in general, and was usually formed at moderate temperatures. Hydromagnesite appeared to be the next most common phase, and formed over roughly the same range of temperatures. Finally, magnesite tended to only form at higher temperatures. There does not appear to be any relationship between saturation index and the phase formed, beyond a rough correlation between temperature and the saturation index of the experiments performed using dissolved magnesium salts. The lack of distinct trends in Figure 6.5 illustrates that formation of magnesium carbonates is complicated and path dependent.

6.4. Effect of Seed Particles on Batch $Mg(OH)_2$ Slurry Carbonation System

In the slurry, $Mg(OH)_2$ particles acted as both Mg source for carbon mineralization as well as a solid surface for hosting carbonate precipitation. The ionic carbonation reaction

was driven by heterogeneous CO_2 solvation and $Mg(OH)_2$ dissolution in the slurry phase. While magnesite formation required high temperatures to overcome the formation of hydrated magnesium carbonates, the CO_2 solvation and therefore $Mg(OH)_2$ dissolution (favored at low pH and high concentration of HCO_3^-) were favored at low temperature. Thus, the overall $Mg(OH)_2$ carbonation would be limited by various reactions depending on the reaction conditions. The $Mg(OH)_2$ slurry carbonation system has been investigated broadly, and it is generally understood that for a given CO_2 pressure, the reaction temperature is the most dominating factor determining the type of carbonate phase produced (Fricker & Park, 2014). The predominant carbonate species which form in the slurry carbonation system can be ordered according to the temperature at which they form from lowest to highest, as such: nesquehonite, dypingite, hydromagnesite, and magnesite (Smithson & Bakhshi, 1973; Botha & Strydom, 2001; Park *et al.*, 2003; Mitsuhashi *et al.*, 2005; Xiong & Lord, 2008; Zhao *et al.*, 2010; Pronost *et al.*, 2011; Schaef *et al.*, 2011; Hopkinson *et al.*, 2012; Hövelmann *et al.*, 2012; Harrison *et al.*, 2013).

Figure 6.6(a-1) shows the XRD pattern of the solids recovered from a $Mg(OH)_2$ slurry carbonation experiment operated at 150 °C and 15 atm CO_2 for 120 min. The product was nearly pure hydromagnesite (~94% conversion) and exhibited the characteristic crystallographic peaks of hydromagnesite at 31°, 15°, and 14° in order of decreasing intensity (Downs, 2006). Hydromagnesite was expected to form at temperatures above those favored by nesquehonite, typically higher than 50 °C in similar aqueous systems (Davies & Bubela, 1973; Botha & Strydom, 2001; Zhang *et al.*, 2006; Cheng & Li, 2010). Its stability range in slurry systems appeared to extend to at least

150 °C (at P_{CO2} = 15 atm) (Fricker & Park, 2014), which is not surprising considering others have formed hydromagnesite at 120 °C and 3 bar CO_2 (Hänchen *et al.*, 2008). Since the solubility of $Mg(OH)_2$ at 150 °C is limited, it was expected that a significant amount of $Mg(OH)_2$ particles existed during the formation of hydromagnesite. The solid $Mg(OH)_2$ in the system must have acted as a seeding surface for carbonate precipitation, improving its kinetics. Figure 6.6(a-2) displays the morphology of the solid product, where the disordered sheet-like particles were associated with the hydromagnesite phase.

In an experiment at the same reaction temperature, but with the inert alumina seed particles present to provide additional surface area for precipitation, the carbonate product was quite similar. Figure 6.6(b-1) illustrates that the solids formed were predominantly hydromagnesite, with some additional XRD lines originating from the alumina seed material. The SEM image, given in Figure 6.6(b-2), shows the sheet-like structure of hydromagnesite, which appeared to be attached to the surface of a seed particle. Unlike the case without inert seed particles (Figure 6.6(a-2)), where there was competition for the $Mg(OH)_2$ surface between $Mg(OH)_2$ dissolution and hydromagnesite precipitation reactions, the carbonate particles produced with Al_2O_3 seeds were more structured.

In contrast, a similar experiment performed with 30 mol% magnesite seed particles produced solids of an entirely different form and chemistry. The XRD pattern of solids recovered after 120 min in the magnesite-seeded experiment (Figure 6.6(c-1)) revealed the dominant peaks of magnesite (33°, 43°, and 54° in order of decreasing intensity) (Downs, 2006). The products in the magnesite-seeded experiment at 150 °C contained no hydromagnesite. In addition, the SEM image (Figure 6.6(c-2)) exposed a product

morphology that was quite unlike both the unseeded and inert seeded products. It is clearly a cubic morphology, typical for magnesite, but larger than the starting material (Figure 6.4(c)).

The apparent effect of the magnesite seeds on $Mg(OH)_2$ slurry carbonation was likely the result of surface chemistry phenomena. In the case with no additional seeds, hydromagnesite nucleated, either homogeneously or on $Mg(OH)_2$ particles, and grew due to the kinetic inhibition of forming anhydrous carbonate at 150 °C and 15 atm of CO_2 pressure. Inert seeds, of similar morphology to magnesite seed particles, provided an insoluble surface for carbonates to nucleate and grow on. Again, metastable hydromagnesite nucleated due to its faster kinetics as compared with $MgCO_3$. However, when magnesite seed particles were present, the kinetically inhibited nucleation step was avoided, and thus, $MgCO_3$ growth was enabled. The concept of disjoining pressure, while typically referred as a repulsive force in reactive mineral cracking (Kelemen *et al.*, 2013) and cement fracturing (Espinosa-Marzal & Scherer, 2010), can be used to understand the seeding effect of similar and dissimilar seeding materials. Disjoining pressure is derived from the contributions of its individual forces: van der Waals, electrostatic double layer, and structural forces (Karoussi & Hamouda, 2007). Given the similar liquid phases compositions, heavy mixing of the slurry, and the similarity in morphology between inert and magnesite seeds, the van der Waals and structural forces were likely negligible in this study. Therefore, the double layer electrostatic forces, namely the potential difference between the precipitation event and the surface, likely influenced the seeding effect.

6.5. Effect of Temperature on Magnesite-Seeded $Mg(OH)_2$ Slurry Carbonation

The ability to produce magnesite at 150 °C utilizing magnesite seed material in a system that otherwise produced hydromagnesite was significant; thus, further in-depth study was performed to investigate the range of reaction temperature where this effect would sustain (80-150 °C). Slurry samples were taken throughout the carbonation reactions to collect both aqueous and solid samples, providing insight into the reaction mechanism. Qualitative TGA decomposition of collected samples was used in combination with XRD data to confirm the existence of a single carbonate phase, either hydromagnesite or magnesite. Carbonation reaction conversion was then calculated from accurate quantitative measurements of carbon content within the recovered solid products using CA. The mass fraction of a carbonate phase in the solid sample was calculated from the mass fraction of carbon and stoichiometry. The remainder of the solids were assumed to be $Mg(OH)_2$. Then, the total solid mass in the slurry at each given reaction time was calculated from an Mg mass balance using the mass fractions obtained from solid samples and the initial total mass. From the total mass and mass fraction of carbonate phases estimated at each given reaction time, the absolute amounts of each solid phase were calculated (e.g. $m_{HM,t}$ and $m_{M,t}$). Equation 6.5 and Equation 6.6 were used subsequently to calculate the conversion of $Mg(OH)_2$ to hydromagnesite (HM) and magnesite (M), respectively, as a function of time. The conversion calculation utilized the initial masses of the reactants and products (e.g. $m_{Mg(OH)2,t=0}$, $m_{HM,t=0}$, and $m_{M,t=0}$) in combination with the molar masses of reactants and products (e.g. $M_{Mg(OH)2}$, M_{HM}, and M_M).

Equation 6.5: $$X_{HM,t} = \frac{m_{HM,t} - m_{HM,t=0}}{m_{Mg(OH)2,t=0} \cdot \frac{M_{HM}}{5 \cdot M_{Mg(OH)2}}}$$

Equation 6.6: $$X_{M,t} = \frac{m_{M,t} - m_{M,t=0}}{m_{Mg(OH)2,t=0} \cdot \frac{M_{M}}{M_{Mg(OH)2}}}$$

In the experiments where multiple carbonate phases were formed, the carbon percentage alone was not enough to calculate the conversion. In order to distinguish between the two carbonates, hydromagnesite and magnesite, TGA decomposition curves of each sample where examined and compared. Crystallized H_2O, hydroxide, and carbonate decomposed at different temperatures, depending on the composition of the solid sample (Sawada *et al.*, 1978; Vágvölgyi *et al.*, 2008a; Vágvölgyi *et al.*, 2008b). Figure 6.7 shows the typical data from the carbonate product recovered during magnesite-seeded $Mg(OH)_2$ carbonation at 80 °C: (a) the thermal decomposition curves (TG), and (b) derivative mass change (dTG). For example, the dTG of the 15 min carbonation sample leveled off at 260 °C, which allowed for the distinction between mass loss due to the decomposition of crystallized H_2O within hydromagnesite (prior to 260 °C) and after due to the decomposition of hydroxide in $Mg(OH)_2$. Similarly, the leveling off at 440 °C enabled the differentiation between mass losses due to the calcination of hydromagnesite and magnesite, before and after respectively.

Next, the corresponding TG mass percent at all significant temperatures was noted, and mass percent differences were calculated for each step. Stoichiometry can relate the mass percent difference for a specific decomposition event to a mass percent of that phase in the total solids. For example, the mass change percent was estimated to be 15.5% for the decomposition of carbonate from $MgCO_3$ in the 120 min carbonation

sample. Stoichiometry then dictated that the sample was 29.7 wt% anhydrous $MgCO_3$. The carbon content data complemented and clarified that obtained via thermal decomposition analysis. Specifically, the decomposition curves of hydroxide in $Mg(OH)_2$ and the hydroxide and carbonate in hydromagnesite in the dTG plot were found to be slightly overlapped. Thus, the deconvolution of the dTG curves should be carefully performed to provide an accurate estimation of the chemical composition of the carbonated products. In this study, the characteristic temperature (from dTG) and consequently the mass change (from TG) were iterated and checked until the calculated carbon content was equivalent to the total carbon mass percentage obtained from CA. This method was possible since the carbon content was the sum of carbon in hydromagnesite and/or magnesite, and magnesite's decomposition curve had significant separation to accurately estimate from the TG/dTG data. Again, as in the case with single carbonate phases, the conversions were obtained using Equations 2 and 3.

The systematic solid analysis is depicted in Figure 6.8 as the conversion of $Mg(OH)_2$ to (a) magnesite and to (b) hydromagnesite. The slurry carbonation experiments at 150 °C provided a clear example of the effect magnesite seeds have on the formation of carbonate phases. Nearly 95% of the $Mg(OH)_2$ was converted to magnesite experiment after 75 min. Whereas 94% of the $Mg(OH)_2$ was converted to hydromagnesite after 60 min without additional seeds, and nearly 100% in 45 minutes in the inert seeded experiment. At the lower temperatures, 80 °C and 120 °C, the $Mg(OH)_2$ was converted to a mixture of magnesite and hydromagnesite during magnesite-seeded experiments. As depicted in the conversion plots (Figure 6.8(a) and (b)), more $Mg(OH)_2$ was converted to magnesite at 120 °C than 80 °C, with the conversion of 24% versus 5% respectively. In

Figure 6.8(b), the rate of hydromagnesite formation was shown to increase with reaction temperature. Interestingly, some of the hydromagnesite produced at 120 °C was converted to magnesite after 60 min of reaction time, possibly the result of aging effects. Due to the kinetic limitations in forming Magnesite at T < 150 °C, for a given set of experimental conditions there was a specific time limit that must be passed before magnesite would form. In the liquid phase, the concentration of Mg^{2+} increased as temperature decreased due to increased CO_2 and hydroxide solubilities. At 80 °C, almost 18% of total Mg within the system existed in the aqueous phase, rather than forming solids.

Figure 6.9 combines the solid and liquid analysis data to follow the overall fate of Mg during $Mg(OH)_2$ slurry carbonation experiments. In the aqueous phase at 150 °C, Mg^{2+} concentration was always higher in the experiments with no additional seed and inert seeds. The higher solubility of hydromagnesite was likely the cause of the increased Mg^{2+} concentrations in the non-magnesite seeded test at 150 °C. At 150 °C but with no additional seed and inert seeds, Figure 6.9(a) and (b), fast, though incomplete, conversion of $Mg(OH)_2$ to hydromagnesite was observed with almost 10% of the Mg inaccessible for carbon storage due to hydromagnesite's solubility. It should be noted that there was more error inherent in the conversion estimates from the inert seeded experiments due to the difficulty in determining the percent alumina in the solid samples collected over the course of the experiment. Kinetically, the reactions with no additional seed and inert seeds resulted in faster carbonation, which was likely due to the faster speed of hydromagnesite nucleation and growth.

Magnesite-seeded $Mg(OH)_2$ carbonation at 150 °C, Figure 6.9(c-1), showed gradual conversion of $Mg(OH)_2$ to magnesite, with very minimal Mg in the aqueous phase and a high overall conversion. The rate of magnesite formation was slower than that of hydromagnesite growth at 150 °C (Figure 6.9(a) and (b)). The experiments at reduced temperatures produced mixtures of hydromagnesite and magnesite from $Mg(OH)_2$. Figure 6.9(c-2) obtained at 120 °C shows significant hydromagnesite growth from the $Mg(OH)_2$ slurry, while moderate amounts of magnesite were also observed, particularly at longer reaction time. Lastly, Figure 6.9(c-3) shows that minimal production of magnesite was observed at 80 °C with a significant amount of Mg dissolved within the aqueous phase at the end of reaction. As the reaction temperature decreased, the dissolved Mg fraction increased due to the greater CO_2 solubility at lower temperature, which in turn reduced pH. These observations suggested that there could be a few different limitations to the precipitation rate of magnesite from the $Mg(OH)_2$ slurry. At an early stage when there is little to no dissolved Mg, the overall reaction could be limited by the dissolution rate of $Mg(OH)_2$, but later in the reactions when there is abundant dissolved Mg present, the system appeared to be limited by the precipitation rate and the solubility of the carbonate products.

6.6. Summary

The conversion of magnesium salts and hydroxide to anhydrous magnesium carbonate is a kinetically challenging reaction. The persistence of metastable magnesium carbonate species (e.g. hydromagnesite) would reduce the overall efficiency of a carbon mineralization process due to the weight gain and solubility increase as hydrated

magnesium carbonates are formed. In this study, it was shown that this difficulty can be significantly reduced by avoiding the relatively slow nucleation of magnesite. Reactions seeded with magnesium carbonate particles led to direct crystal growth on the seed particles, yielding the formation of magnesite under reaction conditions that, though thermodynamically suitable for magnesite formation, favor hydrated magnesium carbonate formation. In the high pressure $Mg(OH)_2$ slurry carbonation system at 150 °C, the presence of magnesite seeds bypassed the formation of metastable species entirely. It was also shown that it was possible to grow magnesite crystals below 100 °C and with low CO_2 partial pressures, something that was previously thought far more difficult. In a practical application, directed magnesite formation could be deployed by introducing a slip stream of magnesite products into the carbon mineralization reactor.

Table 6.1: Commonly observed magnesium carbonate and hydroxide phases

Phase	Formula
Brucite	$Mg(OH)_2$
Lansfordite	$MgCO_3 \cdot 5H_2O$
Nesquehonite	$MgCO_3 \cdot 3H_2O$
Hydromagnesite	$Mg_5(CO_3)_4(OH)_2 \cdot 4H_2O$
Magnesite	$MgCO_3$

Table 6.2: Literature data on the conversion of dissolved magnesium to solid magnesium carbonates

Data Point (Fig. 5)	Carbonate Produced	Magnesium Source	Carbon Source	CO_2 Pressure (atm)	Temperature (°C)	Max. Magnesite Saturation Index*	Reference
1	Lansfordite	$Mg(HCO_3)_2$	CO_2	$3.91x10^{-4}$	4	3.7	Ming 1985
2	Nesquehonite	$MgCl_2 \cdot 6H_2O$	Na_2CO_3	$3.91x10^{-4}$	10	3.8	Cheng 2009
3	Nesquehonite	$Mg(HCO_3)_2$	CO_2	$3.91 x10^{-4}$	10	3.8	Ming 1985
4	Nesquehonite	$MgCl_2 \cdot 6H_2O$	CO_2	1.00	20	3.5	Ballirano 2010
5	Nesquehonite	$MgCl_2 \cdot 6H_2O$	CO_2	1.00	20	3.9	Ferrini 2009
6	Nesquehonite	$MgCl_2 \cdot 6H_2O$	Na_2CO_3	$3.91 x10^{-4}$	25	3.8	Kloprogge 2003
7	Nesquehonite	$MgCl_2 \cdot 6H_2O$	Na_2CO_3, CO_2	$9.90 x10^{-1}$	25	3.9	Hanchen 2008
8	Nesquehonite	$MgCl_2 \cdot 6H_2O$	Na_2CO_3	$3.91 x10^{-4}$	40	4.3	Cheng 2009
9	Nesquehonite	$MgCl_2 \cdot 6H_2O$	Na_2CO_3	$3.91 x10^{-4}$	40	4.6	Dong 2008
10	Nesquehonite	$Mg(NO_3)_2$	HCO_3^-	$3.91 x10^{-4}$	45	4.3	Vágvölgyi 2008
11	Nesquehonite	$Mg(HCO_3)_2$	CO_2	$3.91 x10^{-4}$	60	5.5	Davies 1973
12	Nesquehonite	$Mg(NO_3)_2$	K_2CO_3	$3.91 x10^{-4}$	75	5.0	Zhang 2006
13	Nesquehonite	$Mg(NO_3)_2$	$(NH_4)_2CO_3$	$3.91 x10^{-4}$	130	5.3	Sutradhar 2011
14	Hydromagnesite	$Mg(NO_3)_2$	Na_2CO_3	$3.91 x10^{-4}$	45	4.3	Vágvölgyi 2008
15	Hydromagnesite	$MgCl_2 \cdot 6H_2O$	Na_2CO_3	$3.91 x10^{-4}$	50	4.6	Cheng 2010
16	Hydromagnesite	$Mg(NO_3)_2$	K_2CO_3	$3.91x10^{-4}$	80	4.0	Zhang 2006
17	Hydromagnesite	$MgCl_2 \cdot 6H_2O$	Na_2CO_3	$3.91 x10^{-4}$	90	5.1	Cheng 2010
18	Hydromagnesite	$MgCl_2 \cdot 6H_2O$	Na_2CO_3, CO_2	2.97	120	5.6	Hänchen 2008
19	Magnesite	$MgCl_2 \cdot 6H_2O$	Na_2CO_3, CO_2	99	120	4.3	Hänchen 2008
20	Magnesite	$MgCl_2 \cdot 6H_2O$	Na_2CO_3, CO_2	2.97	120	5.6	Hänchen 2008

*Maximum saturation index achievable under experimental conditions reported. Saturation index a measure of degree of supersaturation, defined as the base 10 logarithm of the ion activity product divided by the solubility product constant.

Table 6.3: Literature data on the conversion of brucite to solid magnesium carbonates

Data Point (Fig. 5)	Carbonate Produced	Carbon Source	CO_2 Pressure (atm)	Temperature (°C)	Max. Magnesite Saturation Index*	Reference
1	Lansfordite	CO_2	3.91×10^{-4}	9	4.5	Smithson 1973
2	Nesquehonite	CO_2	15.0	20	5.9	Park 2003
3	Nesquehonite	CO_2	1.00×10^{-1}	25	2.4	Harrison 2013
4	Nesquehonite	CO_2	5.00×10^{-1}	25	2.8	Harrison 2013
5	Nesquehonite	CO_2	1.00	25	2.9	Harrison 2013
6	Nesquehonite	CO_2	3.91×10^{-4}	28	3.6	Smithson 1973
7	Nesquehonite	CO_2	1.00	35	5.6	Mitsuhashi 2005
8	Nesquehonite	CO_2	3.91×10^{-4}	38	3.1	Smithson 1973
9	Nesquehonite	CO_2	81.2	50	6.8	Schaef 2011
10	Nesquehonite	CO_2	1.00	58	3.3	Hopkinson 2011
11	Nesquehonite	CO_2	1.00	70	5.5	Mitsuhashi 2005
12	Nesquehonite	CO_2	15.0	70	6.1	Zhao 2010
13	Hydromagnesite	CO_2	5.02×10^{-2}	22.5	5.5	Xiong 2008
14	Hydromagnesite	CO_2	1.00	25	2.4	Hopkinson 2011
15	Hydromagnesite	CO_2	1.00	65	4.7	Brotha 2001
16	Magnesite	CO_2	81.2	75	6.4	Schaef 2011

*Maximum saturation index achievable under experimental conditions reported. Saturation index a measure of degree of supersaturation, defined as the base 10 logarithm of the ion activity product divided by the solubility product constant.

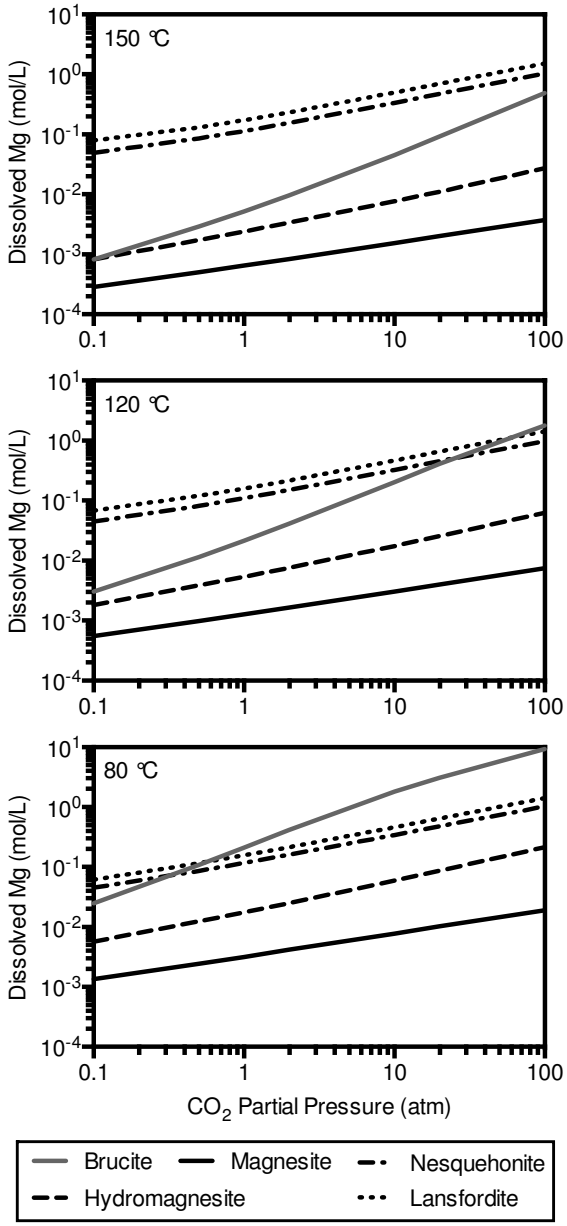

Figure 6.1: Solubilities of pure magnesium carbonates and hydroxide as a function of temperature and CO_2 pressure created using PHREEQC along with the Lawrence Livermore National Laboratory Database (llnl.dat).

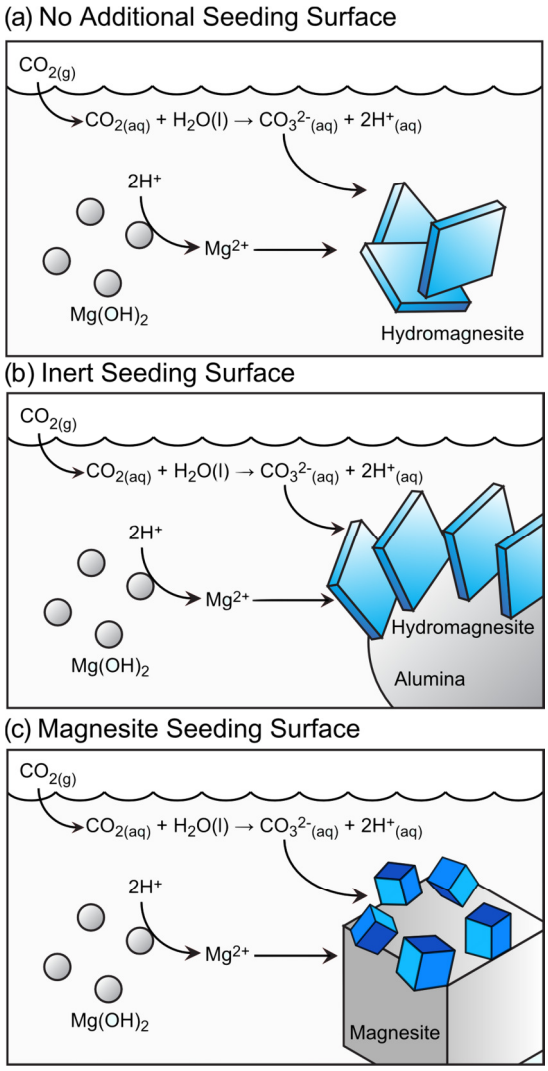

Figure 6.2: Schematic description of hypotheses related to seeded magnesium carbonate synthesis, including (a) homogeneous nucleation of hydromagnesite from brucite, (b) heterogeneous nucleation of hydromagnesite on the surface of an inert seeding particle, and (c) the growth of magnesite onto the surface of existing magnesite seeds.

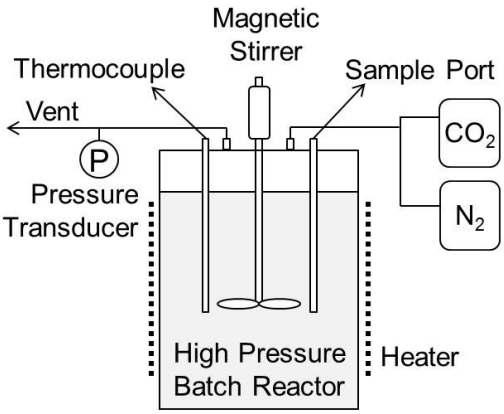

Figure 6.3: Schematic of experimental apparatus for $Mg(OH)_2$ slurry carbonation.

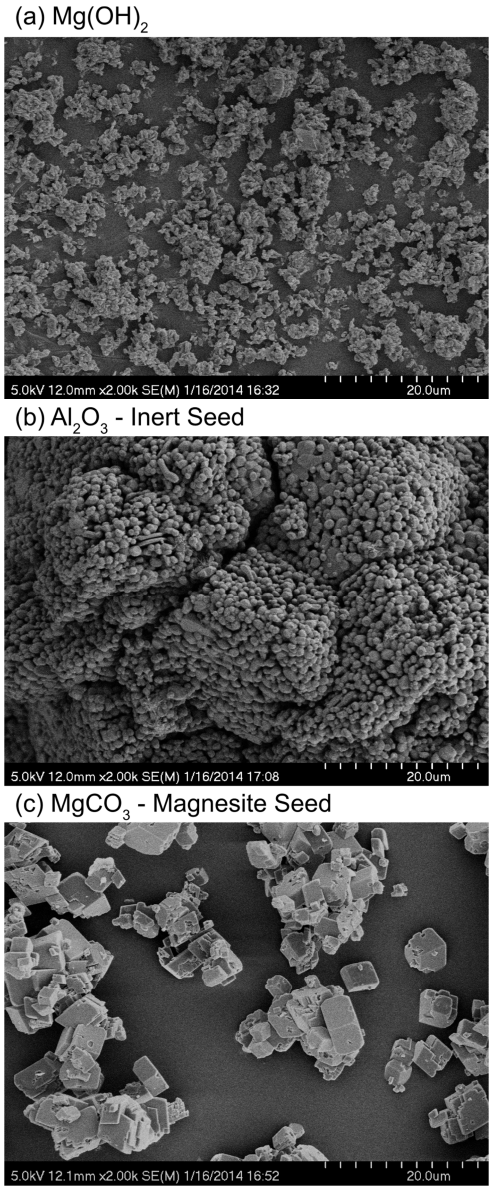

Figure 6.4: SEM Images of starting materials: (a) $Mg(OH)_2$ as Mg^{2+} source, (b) aggregates of Al_2O_3 particles used as inert seeds, and (c) magnesite ($MgCO_3$) seed particles.

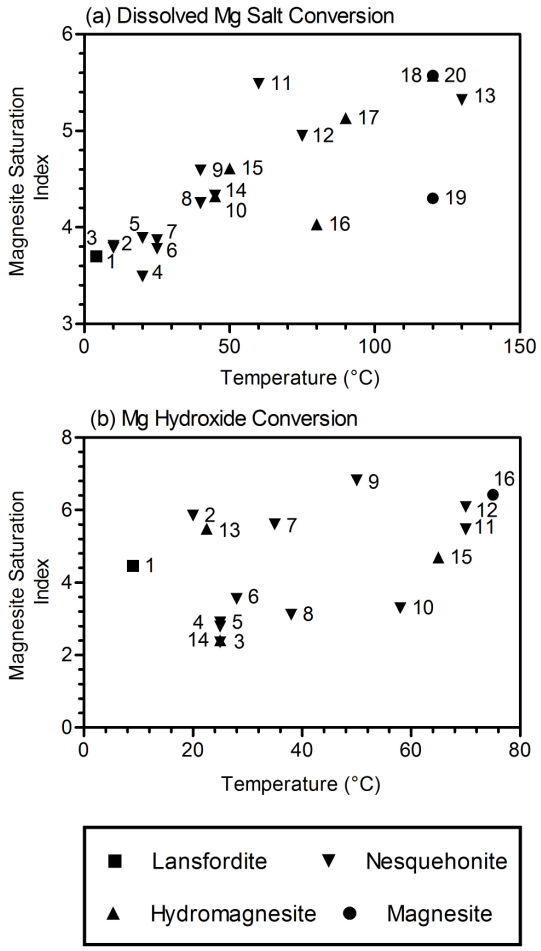

Figure 6.5: Summary of literature data versus simulated magnesite saturation index at various reaction temperatures. Different magnesium carbonate phases are indicated by the symbol, and numbers refer to studies listed in Tables 2 and 3.

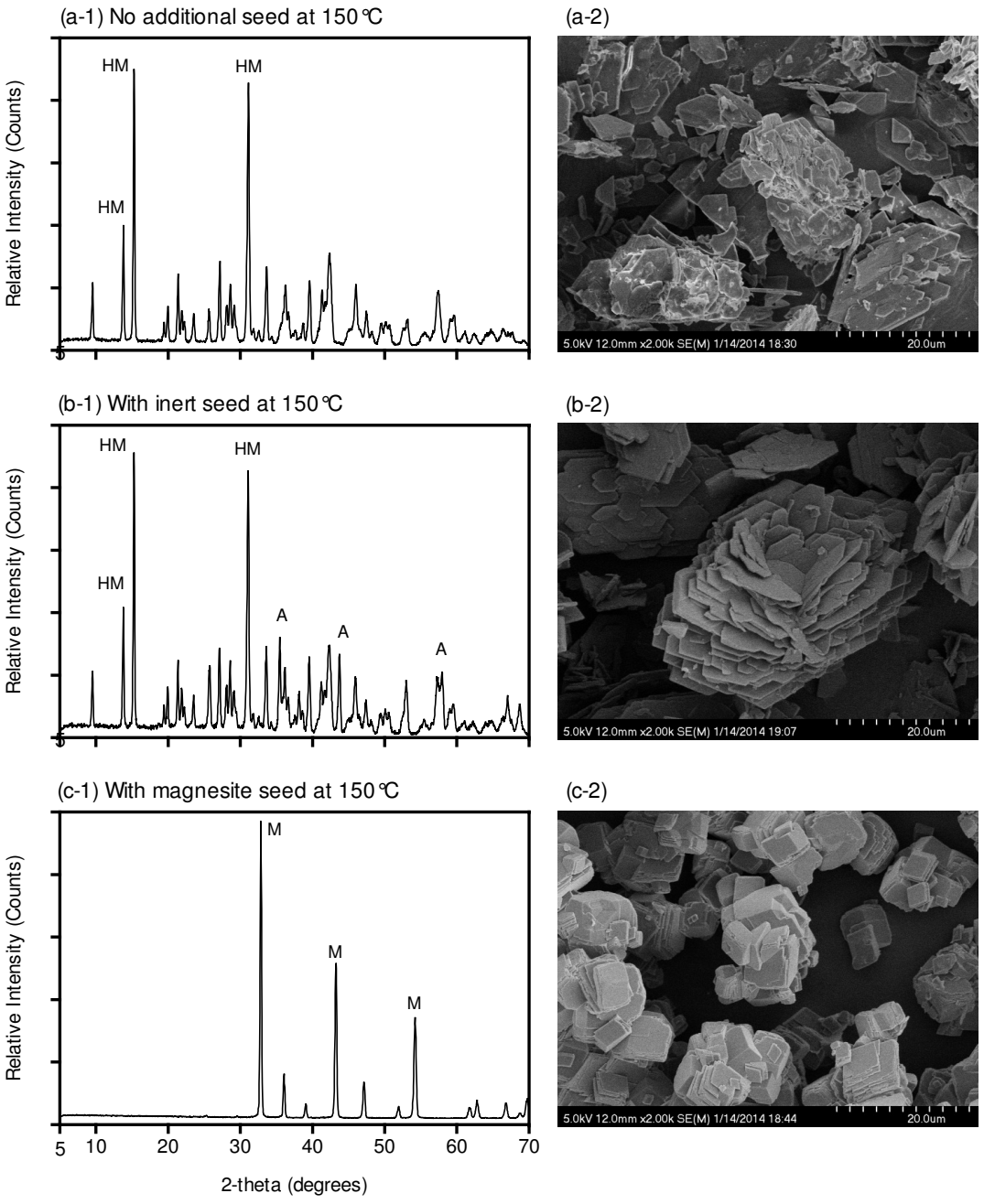

Figure 6.6: Effect of seeds on $Mg(OH)_2$ slurry carbonation at 150 °C after 120 min of reaction. Products analyzed with (1) XRD and (2) SEM. XRD labels: alumina (A), hydromagnesite (HM), and magnesite (M).

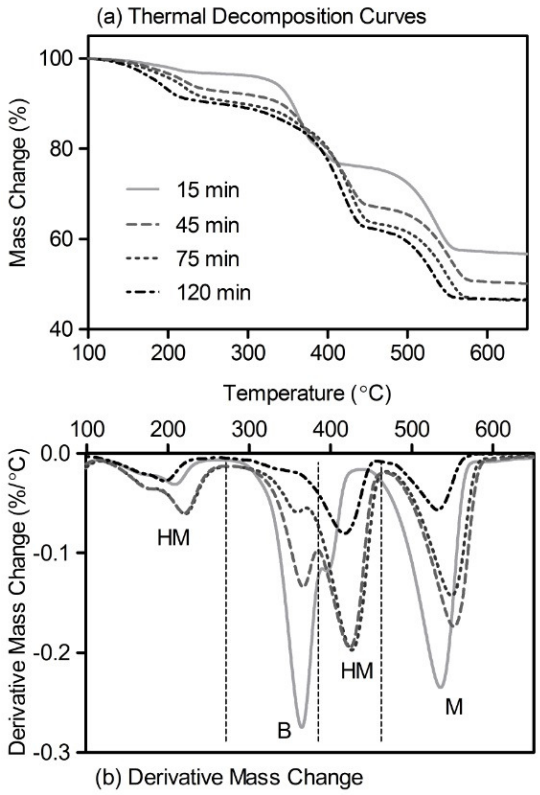

Figure 6.7: Example of TGA decomposition data used to distinguish between carbonates in $MgCO_3$-seeded carbonation of $Mg(OH)_2$ at 80 °C with samples taken at various reaction times (noted in legend): (a) raw thermal decomposition curves and (b) differential mass change.

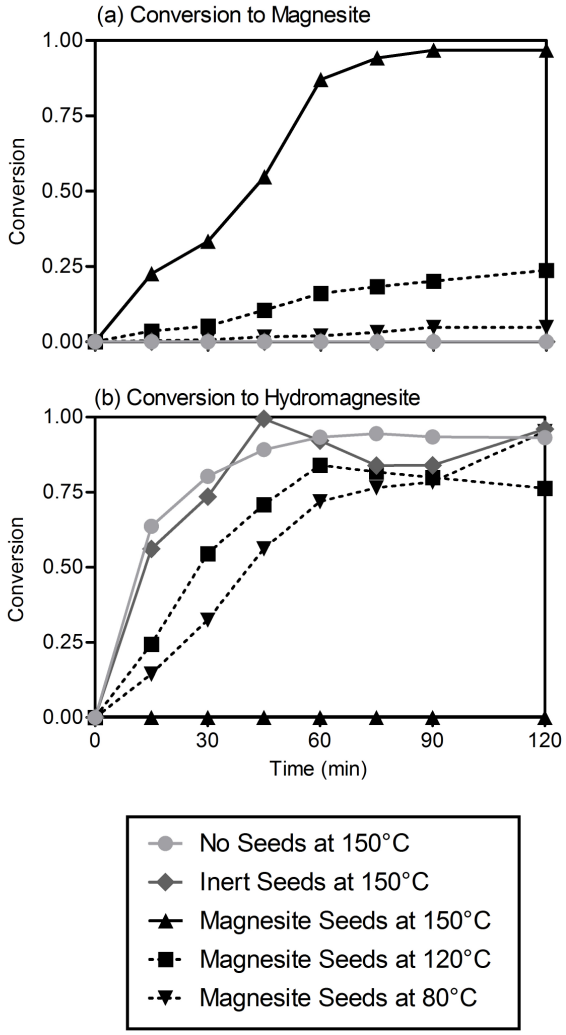

Figure 6.8: Effect of temperature on magnesite-seeded $Mg(OH)_2$ slurry carbonation compared to no seed and inert seed cases at 150 °C: (a) conversion of $Mg(OH)_2$ to anhydrous $MgCO_3$ and (b) conversion of $Mg(OH)_2$ to hydromagnesite.

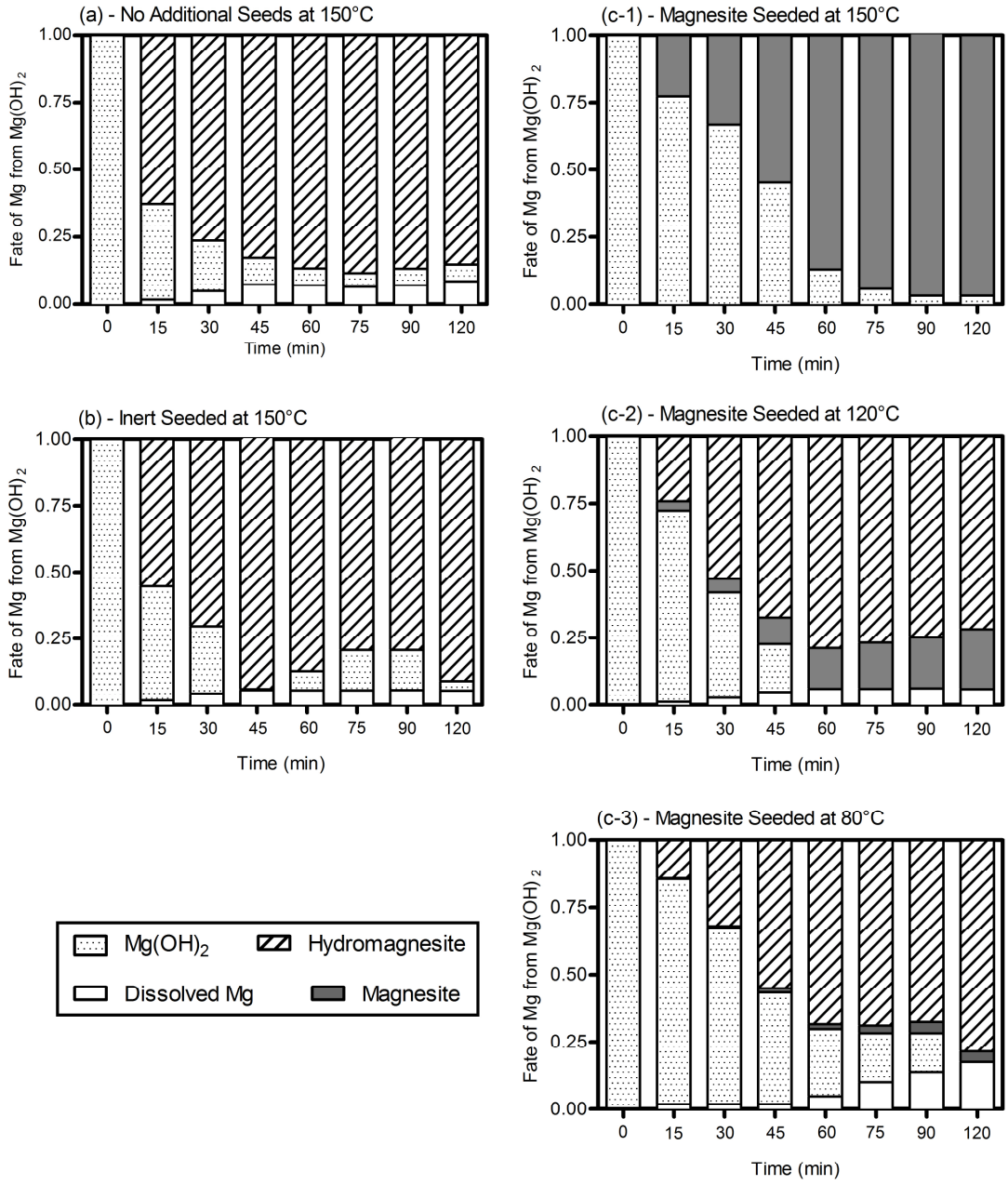

Figure 6.9: Distribution of Mg from $Mg(OH)_2$ across three solid phases and dissolved phase: (a) at 150 °C with no seed particles, (b) at 150 °C with inert seeds, (c-1) at 150 °C with magnesite seed, (c-2) at 120 °C with magnesite seed, (c-3) at 80 °C with magnesite seed.

6.7. Supporting Information

6.7.1. Saturation Index and Crystal Growth

Precipitation of a new solid phase in a closed system involves three steps (Vehkamäki, 2006). The first is the formation of a supersaturated solution. Supersaturation can be described by the saturation index (Ω), calculated as the logarithm of the ion activity product (IAP) divided by the solubility product constant of the phase in question (Equation 6.4). On this scale, a saturated solution has an $\Omega = 0$, a supersaturated solution $\Omega > 0$, and an undersaturated solution an $\Omega < 0$. The second step in precipitation is the formation of stable crystals of the new phase, also referred to as nucleation. Often nucleation in an experimentally relevant period of time will require the solution be significantly supersaturated, and moderately supersaturated solutions are sometimes referred to as metastable (Stumm, 1992). The final step of precipitation is the growth of these newly nucleated crystals of the new phase. In this stage, the soluble components of the new phase are consumed as the sizes of the new crystals grow.

The kinetics of crystal growth are most generally explained by an empirical rate law given in Equation 6.7, where k is the rate constant, omega is the saturation index, and n is the reaction order, which is often found to be two (Stumm, 1992). However, this is generally found to be an over simplification, as the precipitation rate is not just determined by solution supersaturation. Precipitation kinetics are most accurately described by fitting a surface speciation model to experimentally derived rates.

Equation 6.7: $$R = k(\Omega - 1)^n$$

6.7.2. Modeling the Seeded Production of Magnesite

The conversion of magnesium hydroxide to carbonate was modeled in using a combination of the geochemical simulation software PHREEQC and published precipitation rates for magnesite (Donnet *et al.*, 2005; Parkhurst & Appelo, 2013). The thermodynamic database used in PHREEQC was llnl.dat. While this database contains thermodynamic data for a wide range of reactions, those of interest to this study are shown below. The first is the dissolution of CO_2 into the aqueous phase, calculated by a conventional Henry's law relationship, and the hydration reaction of CO_2 with water to dissociate into bicarbonate and carbonate ions (Equation 6.1). The protons from carbonate dissociation react with magnesium hydroxide to yield dissolved magnesium ions (Equation 6.2), and these combine with the carbonate ions to form magnesite ($MgCO_3$) (Equation 6.3). Since there is limited information on the precipitation kinetics of hydromagnesite (the secondary phase formed in the experiments above) it is ignored in these simulations. Instead, magnesite precipitation was modeled using the BET surface area normalized reaction rate recently published by Saldi et. al. (Equation 6.8), where k^-_{Mg} is a rate constant, K_{OH} and K_{CO3} are equilibrium constants, and the a_i terms are solution phase activities of the species I (Zhang *et al.*, 2006; Hänchen *et al.*, 2008; Vágvölgyi *et al.*, 2008a; Cheng & Li, 2010; Saldi *et al.*, 2012).

$$r_{\mathrm{Mg}} = k^{-}_{\mathrm{Mg}} \left(\frac{K_{\mathrm{CO_3}} K_{\mathrm{OH}}}{K_{\mathrm{CO_3}} K_{\mathrm{OH}} + K_{\mathrm{OH}} a_{\mathrm{CO_3^{2-}}} + K_{\mathrm{CO_3}} a_{\mathrm{OH^-}}} \right)^{n} \left(1 - \Omega^{n}_{\mathrm{Mg}}\right)$$

Equation 6.8:

This system was simulated for the three cases of 150 °C, 120 °C, and 80 °C in the presence of 30 mol% magnesite seeds. As was noted at the end of the last section, the

experimental data indicated that brucite dissolution rates appear to be limiting the precipitation at early times in these reactions. Since a dissolution rate equation for brucite has not been published at high temperature, brucite solubility was manually restrained to achieve a similar effect. The brucite saturation index was set to -2.25 for 80 °C, -1.3 for 120 °C, and -0.22 for 150 °C. While using the brucite saturation index as a fitting parameter is not ideal, the values required to yield a representative trend in the simulations results are reasonable and follow the expected relationship; as the reaction temperature increases, the dissolution rate of brucite will increase and it will approach equilibrium with the surrounding solution. It should also be noted there is currently no method to decouple the limitations in brucite dissolution rate from limitations in the CO_2 hydration rate, another reaction that is known to be slow. For the purposes of this discussion, the two limitations will simply be referred to as brucite dissolution, under the assumption that the actual limitation is like a combination of factors.

The results of these simulations are given in Figure S1(a) as the conversion to magnesite over time for the three temperatures, illustrating that the highest temperature reaches near complete conversion fastest, followed in order by the two lower temperatures. Figure S1(b-d) shows the distribution of Mg between the three phases tracked in the simulation, brucite, magnesite and dissolved Mg. Across all of the conditions, the amount of dissolved Mg is much lower than observed in the experiments. This is likely caused by two phenomena: the brucite dissolution limitation discussed above and the formation of Hydromagnesite as a dissolved magnesium sink. The simulations also show that while, in a best-case scenario, the conversion to magnesite should be complete at both 120 °C and 150 °C, the best that can be expected at 80 °C is

~20% conversion. In light of these results, it is clear that the conversion of magnesium hydroxide to magnesite is possible, and is primarily limited by the precipitation rate of the magnesite, while also facing secondary limits of brucite dissolution and hydrated phase formation.

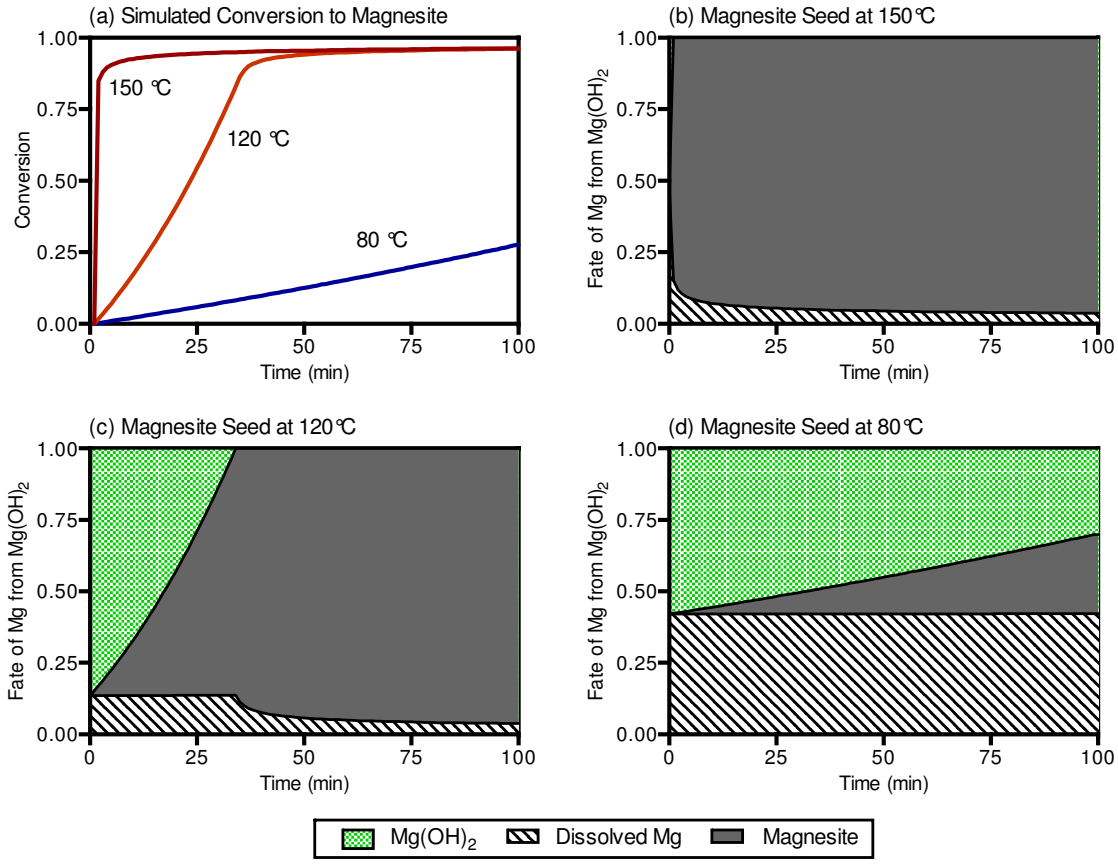

Figure 6.10: Modeling of $Mg(OH)_2$ slurry system seeded with 30 mol% magnesite particles. (a) Experimental conversion of $Mg(OH)_2$ to magnesite in seeded experiments at 150°C, 120°C and 80°C, (b-d) Simulated fate magnesium in at 150°C, 120°C and 80°C, respectively.

7. Enhanced Water Gas Shift Reaction in the Presence of a $Mg(OH)_2$ Slurry in a High Pressure Aqueous System

The contents of this chapter are to be submitted for publishing in Elsevier's International Journal of Hydrogen Energy (Fricker & Park, 2014).

7.1. Introduction

The industrial revolution was fueled by carboneous material, and it will continue to dominate our energy supply mix into the foreseeable future. Technological innovation in the use of carboneous fuels can increase the material efficiency and minimize detrimental environmental impacts. Traditional energy conversion systems, e.g. upgrading petroleum to gasoline or combustion of coal for electricity production via steam, were developed in a time where efficiency and environmental impacts were less understood. Modern energy conversion systems utilize a synthesis gas (syngas) intermediate, adding to the efficiency of the energy recovery. Syngas, a mixture of hydrogen (H_2) and carbon monoxide (CO) primarily, is produced via thermochemical gasification of any carboneous feedstock, including synthetic and biogenic wastes. Integrated gasification combined cycle (IGCC) power plants burn the syngas in gas turbines for more efficient electricity generation. Looking beyond electricity, syngas can be upgraded into nearly any synthetic hydrocarbon fuel or chemical given specific reactor conditions and catalysts.

Most downstream processes operate best at a specific H_2/CO ratio, which is typically higher than the ratio found in the freshly produced syngas. Depending on the gasification conditions and reactor arrangement, CO composition in syngas can range from 17.4% (moving bed gasifier) to 60.3% (entrained flow gasifier) by mole (Stultz & Kitto, 1992).

Therefore, the water gas shift reaction (WGSR) is employed to boost the H_2 levels in the syngas through the reaction of CO with water vapor (H_2O) (Equation 7.1). Being slightly exothermic ($\Delta H° = -41.1$ kJ/mol), a balance between the kinetics and thermodynamics of the WGSR is necessary for industrial application. The highest conversion is possible at lower temperatures where the reaction is kinetically limited. To bypass these limitations, two separate reactors in series with different catalysts have been used. First the high temperature shift (HTS) reactor at around 400 °C with an iron and chromium based catalyst for fast kinetics, and second, a larger low temperature shift (LTS) reactor with a copper and zinc based catalyst, operated around 200 °C to achieve the highest conversion to H_2 possible with only a fraction of a percent of CO remaining (Lloyd *et al.*, 1989).

Equation 7.1: $CO(g) + H_2O(g) = CO_2(g) + H_2(g)$

Generally, CO_2 is a byproduct of carboneous energy conversion systems, and, in the case of syngas production and upgrading, CO_2 is produced during both gasification and WGSR. In fact, processes which produce synthetic chemicals and fuels—technologies known as X-to-liquids where X can be coal, biomass, waste, etc.—are known for their high carbon footprint, which is mainly attributed to the complex nature of those unit operations (Marano & Ciferno, 2001; Schrag, 2009). By capturing CO_2 where generated, hydrogen production can be enhanced according to Le Chatelier's equilibrium principle, thus improving the overall sustainability of the process. A thermodynamic model of the system, Figure 7.1, illustrates the effect of CO_2 removal (by MgO carbonation) on the equilibrium concentration of equimolar gaseous reactants ($P_{CO,i} = P_{H2O,i} = 10$ atm). Theoretically, integrated carbonation with the WGS reaction can sustain hydrogen production near 100% until the decomposition temperature of $MgCO_3$ is reached. The

decomposition temperature is dependent on the P_{CO2} within the system. The enhanced hydrogen yield offers the potential to eliminate the requirement of the larger and inherently more costly, LTS reactor. More details regarding the thermodynamic model can be found in the following Experimental section.

Previously, the enhanced water gas shift reaction (eWGSR) was investigated using materials like calcium oxide, hydrotalcite, and mixed metal oxides to capture CO_2 (Harrison, 2008). In each case however, the sorbent acted solely to separate the CO_2, and therefore, the sorbent required energy intensive regeneration and the separated CO_2 needed disposal. Using a sorbent derived from profuse Mg-silicate minerals, whose capacity far exceeds current and future CO_2 production (Lackner *et al.*, 1995), is a combined carbon capture and storage solution. CO_2 reacts with the sorbent to form stable and permanent magnesium carbonate which can be stored in confidence without long term monitoring. Previous work by the authors has demonstrated the limitations of gas-solid $Mg(OH)_2$ carbonation and investigated the phenomena involved with slurry phase $Mg(OH)_2$ carbonation at moderate CO_2 pressures (Fricker & Park, 2013; Fricker & Park, 2014). The improved kinetics and potential for nearly complete conversion found with slurry carbonation were a better fit with the eWGSR system. Dissolution (Equation 7.2) and hydration (Equation 7.3) of CO_2 will occur after its production by the WGSR, forming bicarbonate, carbonate and hydrogen ions in solution. Acidic conditions favor dissolution of $Mg(OH)_2$ (Equation 7.4), and subsequently carbonate and dissolved Mg^{2+} will react to precipitate anhydrous magnesium carbonate (Equation 7.5). Due to the reaction temperature, the existence of metastable hydrated carbonate phases was not an issue (Fricker & Park, 2014).

Equation 7.2: $CO_2(g) = CO_2(aq)$

Equation 7.3: $CO_2(aq) + H_2O = H_2CO_3(aq) = HCO_3^- + H^+ = CO_3^{2-} + H^+$

Equation 7.4: $Mg(OH)_2(s) + 2H^+ = Mg^{2+} + 2H_2O$

Equation 7.5: $Mg^{2+} + CO_3^{2-} = MgCO_3(s)$

Beyond decarbonizing the process and enhancing H_2 production, the slurry vapor pressure can provide the H_2O required by the WGSR. In a pressurized H_2O system, the WGSR experienced kinetic enhancement due to the pressure effect and enhanced product formation due to excess H_2O (Elliott & Sealock, 1983). Further, $MgCO_3(aq)$, a product in the eWGSR system, has demonstrated moderate homogeneous catalytic activity in an aqueous WGSR (Elliott & Sealock, 1983). Other ancillary benefits of a high pressure aqueous WGSR system include (1) scrubbing other compounds like sulfides with various solution additives, (2) liquid phase heat transfer, (3) catalytic tar cracking by alkaline solution, and (4) hot gas quenching without catalyst deactivation (Sealock *et al.*, 1985).

Rarely are catalyst and WGSR not mentioned together, especially at the low reaction temperature of this study. Platinum was chosen for its high activity because the purpose of this study is to understand the effect of magnesium carbonation on the WGSR. Interestingly, magnesium was rarely been applied for its CO_2 capture capabilities (Hassanzadeh & Abbasian, 2010; Choi *et al.*, 2013; Zhang *et al.*, 2013). Rather, magnesium compounds are referenced throughout WGSR literature as a dopant for catalysts, providing morphological enhancements and improved thermal properties (Boudjemaa *et al.*, 2009; Nishida *et al.*, 2009). To the author's knowledge, the integration of $Mg(OH)_2$ slurry phase carbonation with the WGSR has not been investigated

elsewhere. The carbonation reaction was anticipated to enhance the hydrogen yield through an eWGSR process. Unexpectedly, the presence of a bulk $Mg(OH)_2$ slurry also complicated the system through a side reaction between CO and the basic solution to produce formate ions. Thus, the following study explored the complex phenomena involved in the inherently complex multi-phase reaction system of low temperature WGSR with integrated $Mg(OH)_2$ slurry carbonation.

7.2. Experimental

7.2.1. Thermodynamic Model

The following is an explanation of the thermodynamic equilibrium modeling effort behind Figure 7.1 with initial $P_{CO} = P_{H2O} = 10$ bar (assumed). First, the equilibrium expression for the WGSR (Equation 7.6) was simplified due to equimolar conditions (Outotec). Then, the conversion of CO to CO_2 was calculated using Equation 7.7.

$$\textbf{Equation 7.6: } K_{WGSR} = \frac{P_{H2}\,P_{CO2}}{P_{H2O}\,P_{CO}} = \frac{P_{CO}X\;P_{CO}X}{P_{CO}(1-X)\;P_{CO}(1-X)} = \frac{X^2}{(1-X)^2}$$

$$\textbf{Equation 7.7: } X_{WGSR} = \frac{\sqrt{K_{WGSR}}}{1+\sqrt{K_{WGSR}}}$$

Next, the fraction of CO_2 that would react to form carbonate was calculated using $K_{Carb.}$ (Equation 7.8 and Equation 7.9) (Outotec).

$$\textbf{Equation 7.8: } K_{Carb.} = \frac{1}{P_{CO2}} = \frac{1}{P_{CO2}(1-X)}$$

$$\textbf{Equation 7.9: } X_{Carb.} = 1 - \frac{1}{K_{Carb.}P_{CO2}}$$

A new WGS conversion ($X_{WGS,n1}$) was calculated by substituting the new P_{CO2} into WGS equilibrium expression (Equation 7.10), which has been simplified to (Equation 7.11). The root of Equation 7.11 which is between 0 and 1 was taken as the conversion.

Equation 7.10: $$\mathbf{K_{WGSR} = \frac{P_{H2}(1+X)\,P_{CO2}(1+X)}{P_{H2O}(1-X)\,P_{CO}(1-X)}}$$

Equation 7.11: $$\mathbf{(P_{H2}P_{CO2} - K_{WGSR}P_{H2O}P_{CO})\,X_{WGSR,n1}^{2}} + (2P_{H2}P_{CO2} + 2K_{WGSR}P_{H2O}P_{CO})\,X_{WGSR,n1} + (P_{H2}P_{CO2} - K_{WGSR}P_{H2O}P_{CO}) = 0$$

Next, the fraction of remaining reactants (CO and H_2O) which can be converted to H_2 was calculated with $X_{WGS,n1}$. This extra amount was added that to the initial WGS H_2 yield. At this point a new P_{CO2} was calculated, by combining $X_{Carb.}$ with $X_{WGS,n1}$ and the partial pressures of the remaining reactants. This process was iterated several times, by calculating a new WGS conversion based on the calculated partial pressure of reactants and products. Iteration stopped when the calculated difference between successive P_{CO2} values was less than 1 bar, though it should be noted that most of the difference values were far below with some at lower temperatures at less than 10^{-18}. The conversion data for Figure 7.1 are derived from Equation 7.12 and Equation 7.13 for WGSR/eWGSR and carbonation respectively.

Equation 7.12: $$\mathbf{X_{WGSR,plot} = \frac{P_{H2,f}}{P_{CO,i}}}$$

Equation 7.13: $$\mathbf{X_{Carb.,plot} = \frac{P_{H2,f} - P_{CO,f}}{P_{H2,f}}}$$

7.2.2. Materials and Methods

The WGSR was performed in the headspace of a temperature controlled, high pressure batch reactor (#U761, Pressure Products Industries, Inc.) depicted in Figure 7.2. The lower portion of the reactor was a reservoir (300 mL) for the bulk aqueous phase for supplying the required H_2O, as well as containing the carbon capture media, $Mg(OH)_2$, in certain experiments. The reactor was equipped with temperature (type K, Omega) and pressure (Omega) data acquisition capabilities. Gas could be sampled from the headspace and liquid from the bulk solution via a manual sampling rig. During experiments, the aqueous phase was mixed well by a magnetic stirrer set to 700 rpm. In experiments which utilized a catalyst, the material was contained in a basket made of 304 stainless steel mesh 400, which was fixed in the reactor headspace. Those experiments used a 0.5 wt% platinum on alumina (Pt/Al_2O_3) catalyst (Sigma-Aldrich Co.) due to its high activity for the WGSR at relatively low temperature. A mass of 10.1 g of 3.2 mm pellets were placed in the catalyst basket. More details about the catalyst can be found in Table 7.1. The catalyst was characterized by BET analysis (NOVA-win 2002 BET analyzer, Quantachrome Corporation).

The reactor was operated in batch mode due to safety concerns. When beginning an experiment, the reactor was first filled with either deionized H_2O (WGSR) or a $Mg(OH)_2$ slurry (eWGSR). In eWGSR experiments, the slurry was formed by combining 10 g of dry $Mg(OH)_2$ (95% pure, Acros Organics) with 300 mL of deionized H_2O to form a 3.3 wt% slurry. After being sealed, nitrogen (N_2) flowed through the headspace for 15 min or more to purge the reactor of oxygen (O_2). Meanwhile, the temperature of the reactor was

raised to ~85 °C. Upon temperature stabilization, CO was delivered into the headspace, achieving a P_{CO} of ~8.5 atm. After sealing, the temperature ramp to reaction temperature was initiated. The timer for the experiment started when the internal temperature reached 100 °C. On average, the temperature rose at 2.4 °C·min^{-1} to an isothermal hold at a temperature of ~210 °C, and by the end of the 120 min reaction time reached a maximum value of 215-218 °C depending on the experiment.

Four experimental cases were explored in this study. The control with neither slurry nor catalyst was referred to as "WGSR." When slurry is present without catalyst, the experiment was called "eWGSR." The catalytic WGSR and eWGSR were named "WGSR-Pt" and "eWGSR-Pt" respectively.

7.2.3. Analytical Methods

A 1/16 in line with valves on both ends connected the headspace of the reactor to a gas analyzer (3000 Micro GC, Inficon, Inc.). A portion of the line consisted of a 1/4 in water trap contained in an ice water bath to prevent H_2O from entering the GC. After 120 minutes of reaction, the line was filled by opening the valve on the reactor side. Upon closing, the line was discharged by opening the valve on the GC side, which flushed the internal GC column with the gases from the headspace. The line filling and emptying procedure was repeated 3 times before a gas measurement was analyzed. Multiple gas samples were analyzed to ensure accurate results. The GC data provided molar concentrations of gaseous components (N_2, O_2, CO, CH_4, CO_2, H_2, C_2H_4, and C_2H_6) in the headspace other than H_2O at the end of reaction.

At the same time, liquid slurry samples (approximately 10 mL) were removed via the liquid sampling port and rig. After filtration (particle size retention: >11 μm, GE Whatman), solids dried overnight under vacuum at 70 °C before analysis by thermogravimetric analysis (TGA) (SETSYS Evolution, Setaram Instrumentation) and X-ray diffraction (XRD) (X2, Scintag, Inc.) to determine the presence of magnesium carbonate and quantify the conversion. In the TGA, ~20 mg solid samples were heated to 650 °C (at a rate of 5 °C·min^{-1}) in helium (He) flowing at 20 mL·min^{-1}. The mass changes at temperatures corresponding to the decomostion of $Mg(OH)_2$ and $MgCO_3$ phases were used in combination with reaction stoichiometry to quantify the carbonate content of the solids. With the XRD, a step size of 0.05º and scan time of 0.5 s was used to collect the diffraction pattern for each sample in the range 10-70º.

The liquid fraction of the slurry was also collected and analyzed for aqueous specifies produced as a result of side reactions. Samples were diluted 50 times before ion exclusion chromatography (IC) analysis (861 Advanced Compact IC, Metrohm AG). Components were separated with a Metrosep Organic Acids 250/7.8 column using a 0.5 mM H_2SO_4 eluent and 20 mM LiCl suppressor. The IC provided the capability to quantify formate ion concentration and identify carbonate ions

7.3. Effect of Platinum Catalyst and $Mg(OH)_2$ Slurry on WGSR

In the unique reactor system for WGSR used in the current study, initial tests investigated whether the reaction required catalyst. Figure 7.3 contains the fractional conversion of CO in all four reaction scenarios after 120 min. A logarithmic scale

provides a better view of the instances of very low conversion, which occurred in the experiments without platinum catalyst. The WGSR experienced a CO conversion of only 0.614%, whereas the eWGSR resulted in a conversion of 15.2% of the initial CO amount. The presence of the slurry had the effect of converting CO, though the efficacy of slurry phase $Mg(OH)_2$ as a WGSR catalyst will be explored further in a subsequent section. The experiments with the catalyst present experienced dramatically different CO conversions. WGSR-Pt and eWGSR-Pt both converted over 99.9% of the CO. Both effectively converted the entire CO amount in 120 min—the difference was considered insignificant.

Differences arose when the conversion was investigated in terms of the gaseous products, H_2 and CO_2. Since H_2O was far in excess of CO, the product conversion was normalized to the initial CO molar amount. Figure 7.4(a) contains the conversion of CO to H_2, again on a logarithmic scale to improve the appearance of the low conversion values. As was expected, the WGSR converted a small amount of CO to H_2, less than a hundredth of a percent in fact. The eWGSR test also showed a very low conversion to H_2 at 0.0166%, which was in disagreement with the CO depletion found in Figure 7.3. The components involved in the WGSR are all one to one from a molar standpoint (Equation 7.1). If the depletion of CO was caused solely by the WGSR, the amount of hydrogen production should have been at the X marks on the plot. The disagreements continued when looking into the catalyzed reactions. The conversion to H_2 equaled 25.9% in WGSR-Pt and 44.1% in eWGSR-Pt. The presence of the slurry did enhance the conversion of CO to H_2, by around 70%, though the H_2 production appeared limited. As noted, when conversion to H_2 was compared with the depletion of CO, some inconsistencies surfaced. First, the eWGSR test experienced some loss of CO, however

extremely low production of H_2. Second, the catalyzed experiments both converted the entire amount of CO, though this should result in the formation of significant hydrogen. Discussion on these issues will resume in a following section.

The conversion of CO into CO_2 is presented in Figure 7.4(b). Again, the X marks represent the potential CO_2 yield given the amount of CO depleted during reaction. The data was difficult to interpret since a certain amount of CO_2 will dissolve into the bulk fluid in each experiment. The WGSR converted a fraction of a percent of the CO to CO_2 with the eWGSR producing more CO_2 at 2.60%. The lack of hydrogen production in the eWGSR combined with the disappearance of CO and formation of CO_2 pointed to an alternative reaction mechanism. WGSR-Pt converted 17.2% and eWGSR-Pt converted 12.6% of the initial CO to CO_2. The reduced amount of CO_2 present in eWGSR-Pt is likely the result of more CO_2 being pulled into the aqueous phase due to the basic solution and ultimately reaction to form carbonates.

Taking a closer look into the solids recovered from the experiments with slurry phases revealed the existence of carbonate in eWGSR-Pt. Figure 7.5(a) displays the thermal decomposition of the materials compared against the starting material, $Mg(OH)_2$. The solids from eWGSR exhibited a slight shift in decomposition temperature to a higher temperature, possibly due to phase restructuring during reaction or the formation of a passivation layer delaying dehydroxylation. On the other hand, the eWGSR-Pt sample experienced a mass change consistent with $MgCO_3$ decomposition (Fricker & Park, 2013). The XRD patterns in Figure 7.5(b) confirmed the existence of $MgCO_3$ in the eWGSR-Pt solids given its peaks at 33º, 43º, and 54º (Downs, 2006). Quantification from

the TGA data showed that CO_2 represented 9% of the recovered solids mass, which means that 17.2 wt% of $MgCO_3$ was present in that material.

7.4. Resolving the Molar Imbalance

Still though, the imbalance between CO depletion and product formation was no resolved. Elliott et al. (1983) found OH^- producers (specifically alkali and alkaline carbonates) to catalyze a high pressure aqueous WGS System (Elliott & Sealock, 1983). They proposed the following mechanism which is driven by hydroxide ions in solution (Elliott *et al.*, 1983): CO reacted with hydroxide ions in solution to create formate ions (HCO_2^-) (Equation 7.14), formate ions reacted to form carbonate ions and formaldehyde (H_2CO) (Equation 7.15), and formaldehyde decomposed to release H_2 (Equation 7.16).

Equation 7.14: $CO(g) + OH^-(aq) = HCO_2^-(aq)$

Equation 7.15: $2HCO_2^-(aq) = CO_3^{2-}(aq) + H_2CO(l)$

Equation 7.16: $H_2CO(l) = H_2(g) + CO(g)$

Elliot et al. (1983) also discovered that the activity of the basic solution as a catalyst for WGSR was related to the stability of the formate complexes in solution. The complexes with higher stability provided lower WGSR activity because the formate is held in solution, unable to convert to formaldehyde and H_2. Hence, Equation 7.15 was a limiting step in the aqueous process. The disparity between CO consumption and product formation in eWGSR, WGSR-Pt and eWGSR-Pt can be explained by the production of HCO_2^-. The CO was likely converted to CHO_2^- in the basic solution and subsequently

complexed to form soluble magnesium formate ($Mg(HCO_2)_2$), which was held in solution. For reference, the stability of solid magnesium formate hydrate ($Mg(HCO_2)_2 \cdot 2H_2O$), synthesized from formic acid and MgO, was shown to be as high as ~400 °C in a TGA (Dollimore & Gupta, 1979).

To investigate this hypothesis, the separated liquid from slurry samples was analyzed by IC. Figure 7.6(a) shows the spectra for each experiment. Formate ions were found under each of the experimental conditions, with significant amounts observed in eWGSR and eWGSR-Pt. Those tests displayed almost 10 times the concentration of formate. As expected, the existence of dissolved Mg^{2+} and OH^- favored the formation of significant quantities of formate. The formate remained in solution and limited the conversion of CO into the desired WGSR products. The existence of a carbonate peak was observed, though quantification of the carbonate concentration was not possible. Figure 7.6(b) contains the results of the conversion of CO into HCO_2^-. In both WGSR and WGSR-Pt, minimal formation of formate was observed at 1.88% and 2.27% conversion of CO to formate respectively. Conversely, in the experiments with slurry present, 21.9% and 19.2% of the CO were converted to formate in eWGSR and eWGSR-Pt. The presence of more formate in eWGSR is likely caused by a larger CO driving force. In eWGSR-Pt, CO participated significantly in the gas phase WGSR, so there was less available for formate creation. Knowing about the large amounts of HCO_2^- led to an explanation about the existence of CO_2 in the eWGSR with no H_2 formation, which was possibly due to another reaction pathway involving the breakdown of HCO_2^-. The disproportionate disappearance of CO in WGSR-Pt may be the result of the formation of other soluble organic compounds unable to detect by the IC column, bicarbonate, or other species. It

should be noted that subsequent steps after HCO_2^- formation may or not be the same as Equation 7.15 and Equation 7.16, other aqueous reactions/decompositions may be responsible for an enhanced effect on H_2 conversion and other reaction outcomes.

In the current system, two WGSR processes were happening simultaneously: conventional, catalytic gas-phase reaction in headspace (Route 1) and aqueous reaction of CO with OH- (Route 2), which may or may not yield H_2 eventually (Elliott *et al.*, 1983). These processes are labeled on Figure 7.7, which also contains a number of other potential reaction mechanisms achievable in the $Mg(OH)_2$ slurry WGSR/carbonation system. The aqueous, homogeneously catalyzed water gas shift process (Route 3) has been investigated in the past, even accidentally at times. For example, Shabaker observed diminished CO in an aqueous methanol/ethylene glycol reforming process over supported Pt catalysts which was attributed to the WGSR (Shabaker, 2003). The field of homogeneous WGSR catalysis focused on soluble catalytic complexes typically containing ruthenium, rhodium, or carbonyl (Ungermann *et al.*, 1979; King *et al.*, 1980; Ishida *et al.*, 1986; Laine & Crawford, 1988). One proposed mechanism involved the bonding of the metal (catalyst) to CO, which subsequently reacted with hydroxide to form the metal formate. The metal formate released CO_2 as it converted to the metal hydride, which decomposed to release H_2 gas and afterward the metal is available for another loop (Ungermann *et al.*, 1979). More recently, homogeneous catalysis of the WGSR was achieved with supported ionic liquids (Werner *et al.*, 2010).

7.5. Methods for Alleviating Formate Accumulation within the System

A survey of the literature revealed numerous methods for recovering the hydrogen that was accumulating in dissolved formate. The schematic in Figure 7.7 includes three potential routes to facilitate the breakdown of formate into the desired products, H_2 and CO_2. Homogeneous catalysis (Route 4) via ruthenium and rhodium based catalysts has shown promise for recovery of hydrogen from formate/formic acid (Enthaler *et al.*, 2010; Boddien *et al.*, 2011; Czaun *et al.*, 2011). Boddien et al. also observed iron complexes which function in the conversion of formate to H_2 (Boddien *et al.*, 2011). A biological pathway (Route 5) to H_2 from formate utilizing formate hydrogenlyase (FHL) enzyme has been demonstrated (Yoshida *et al.*, 2005; Fan *et al.*, 2009; Kim *et al.*, 2010). Sawers found the biological conversion to take place in two steps, where first formate is converted to CO_2 and H^+, and second H^+'s combine to form H_2 (Sawers, 2005). Lastly, a heterogeneous catalyst system (Route 6) was used in 1996 by Onsager et al. to decompose potassium formate in water at 70-140 °C forming H_2. The catalyst, 5-10% palladium (Pd) on activated carbon, achieved a turnover rate of 10^4 mol H_2/mol Pd (Onsager *et al.*, 1996). In any case, the CO_2 should dissolve and mineralize (7) with Mg^{2+} in solution derived from $Mg(OH)_2$ (Fricker & Park, 2014).

7.6. Summary

The platinum catalyst was effective and necessary to enable significant WGSR. A closer examination of the disappearance of CO and the formation of H_2 and CO_2 revealed an inconsistency, which led to the realization surrounding the creation of formate in

solution. By producing formate, the efficacy of the WGSR at producing hydrogen was reduced. Nonetheless, the eWGS-Pt experiment produced the largest hydrogen yield, likely due to the equilibrium shift cause by the aqueous carbonation reaction to form $MgCO_3$. The existence of the bulk aqueous phase certainly complicated the catalytic gas phase WGSR. Future work aims to investigate the methods for facilitating the decomposition of formate in solution to yield H_2. By tuning the gas-liquid-solid equilibria, various high pressure aqueous WGS reactor arrangements can be envisioned, such as a bubble column or spray tower reactor.

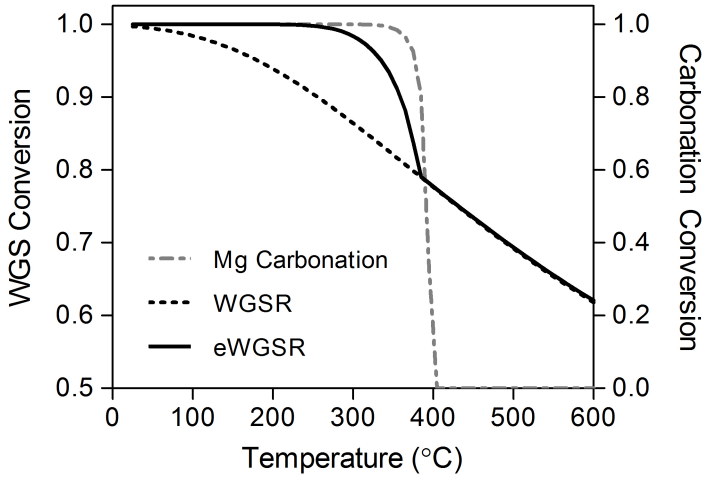

Figure 7.1: Thermodynamic equilibrium model of effect of carbonation on WGS reaction. WGS conversion defined as fraction of CO converted to H_2 and carbonation conversion defined as fraction of CO_2 converted to $MgCO_3$. Equilibrium constants generated with HSC Chemistry (Outotec). $P_{CO,i} = P_{H2O,i} = 10$ atm.

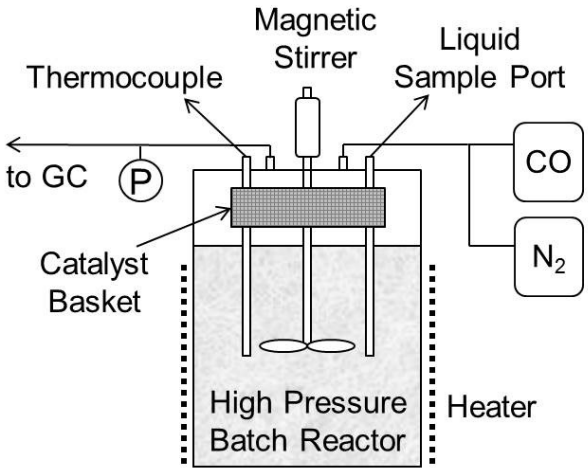

Figure 7.2: Schematic of high pressure batch reactor.

Table 7.1: Catalyst characterization

	Surface Area (m^2/g)	**Active metal**	**Loading (% wt.)**	**Quantity in basket (g)**	**Quantity active (g)**	**Surface (m^2)**
Pt/Al_2O_3	93	Platinum	0.5	10.1	0.051	940

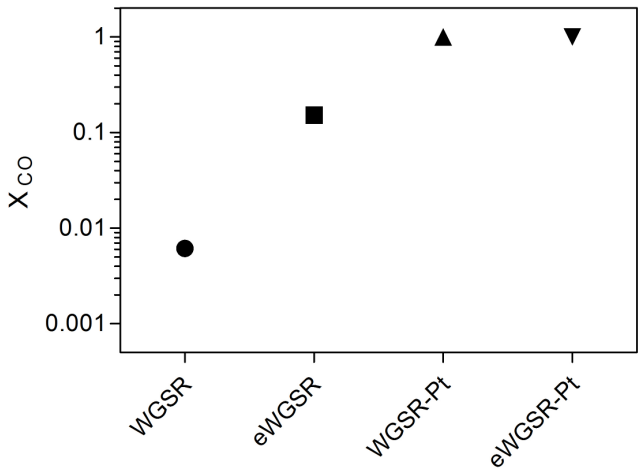

Figure 7.3: Effect of platinum catalyst and slurry on the depletion of CO.

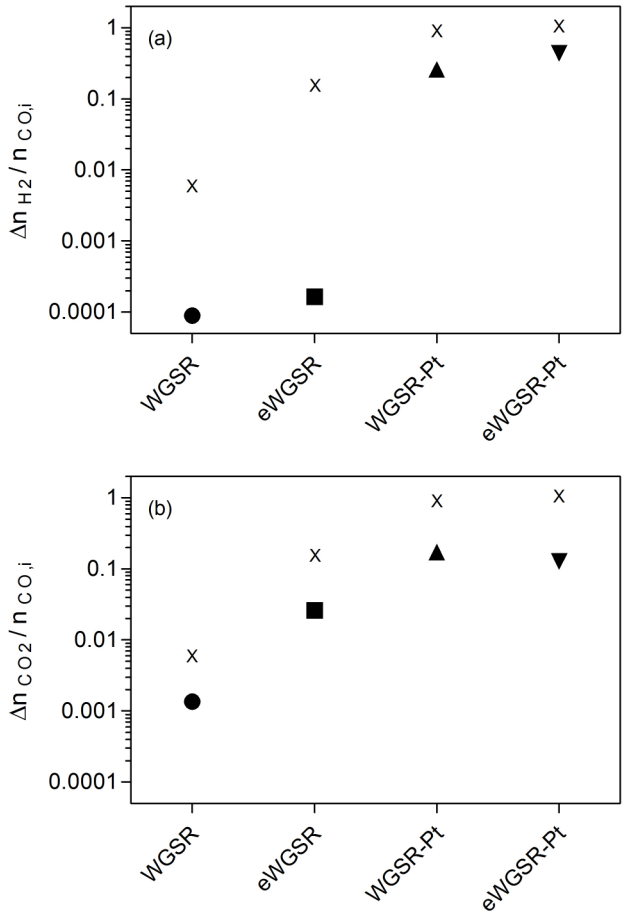

Figure 7.4: Effect of platinum catalyst and slurry on the production of H_2 (a) and CO_2 (b) normalized to the initial moles of CO. H_2 and CO_2 yields calculated from CO depletion figures are marked with X.

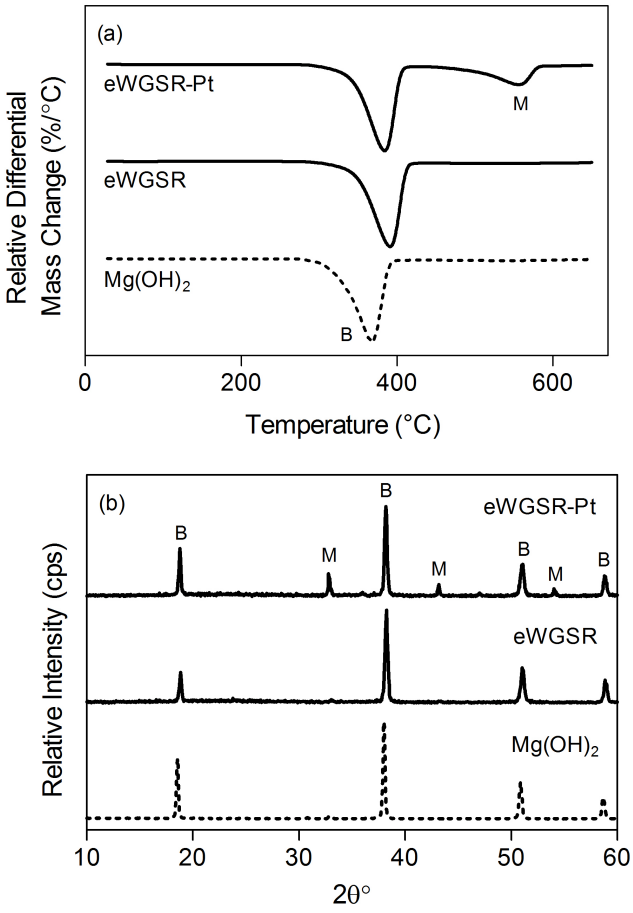

Figure 7.5: Analysis of the solids recovered from eWGSR experiments compared against the reagent $Mg(OH)_2$. Graphs: thermal decomposition in TGA (a) and X-ray diffraction (b). Labels: brucite/$Mg(OH)_2$ (B) and magnesite/$MgCO_3$ (M).

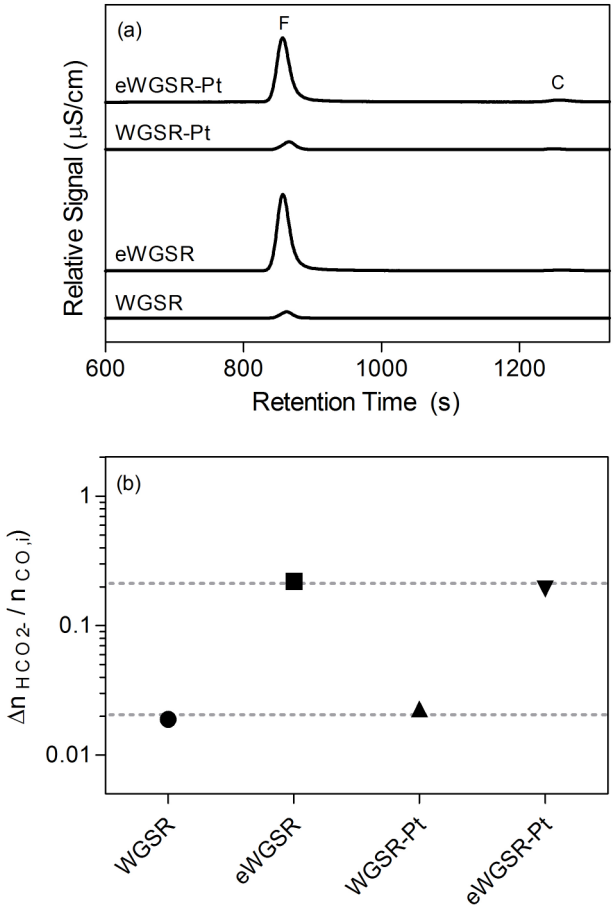

Figure 7.6: Liquid fraction of slurry analyzed via ion chromatography (IC). Samples diluted 50x prior to analysis. Graphs: IC output (a) and production of HCO_2^- normalized to the initial moles of CO. Labels: formate/ HCO_2^- (F) and carbonate/CO_3^{2-} (C).

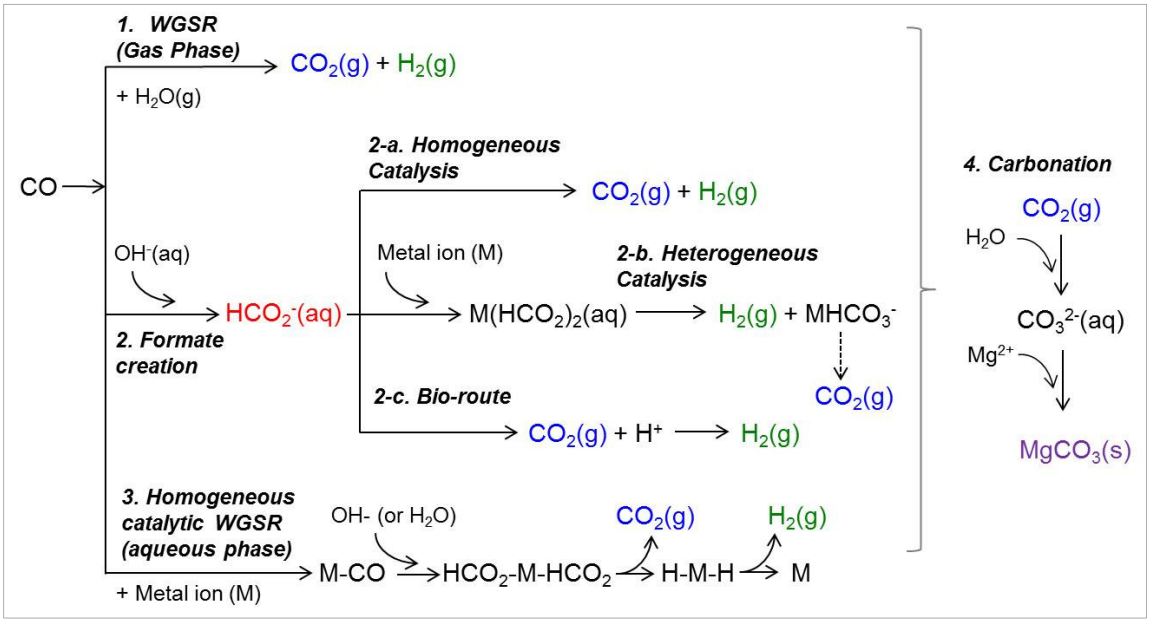

Figure 7.7: Proposed reaction mechanisms in conventional and aqueous WGSR integrated with CO_2 mineralization. Routes: (1) conventional gas-phase WGSR, (2) formate production (Elliott *et al.*, 1983), (3) homogeneous aqueous WGSR (Ungermann *et al.*, 1979; King *et al.*, 1980; Elliott & Sealock, 1983; Laine & Crawford, 1988), (2-a) homogeneous catalytic breakdown of formate (Enthaler *et al.*, 2010; Boddien *et al.*, 2011; Boddien *et al.*, 2011; Czaun *et al.*, 2011), (2-b) heterogeneous catalytic breakdown of soluble formate salt (aqueous potassium formate over 5-10% Pd on activated carbon) (Onsager *et al.*, 1996), (2-c) biological reaction with formate hydrogenlyase (FHL) enzyme (Sawers, 2005; Yoshida *et al.*, 2005; Fan *et al.*, 2009; Kim *et al.*, 2010), and (4) CO_2 mineralization (Fricker & Park, 2014).

7.7. Supporting Information

7.7.1. Experimentation with Industrial Catalysts under R&D

A similar reactor arrangement was used as described in materials and methods section of article. The only differences between the article and the following results relate to the type of catalyst and reaction time. The catalysts are proprietary with some characterization information contained in Table 7.2 and compared with the Pt/Al_2O_3 catalyst. The HTS and LTS catalysts were compacted into 6 pellets (roughly 250 mg each) which were loaded into the basket. A reaction time of 300 min was tested in order to observe adequate conversion. The same naming convention was used in the following results.

Results follow the same organization as those in the manuscript. First, the fractional conversion, or depletion, of CO is presented in Figure 7.8. Next the normalized production of WGSR products H_2 and CO_2 are given in Figure 7.9. Figure 7.10 contains the analysis of recovered solids from eWGSR experiments. Lastly, Figure 7.11 includes the liquid phase analysis for the quantification of formate ions and the fractional conversion of CO to HCO_2^-.

Table 7.2: Comparison of the properties of Pt/Al_2O_3 catalyst with proprietary industrial WGSR catalyst.

	Surface Area (m^2/g)	**Active metal**	**Loading (% wt.)**	**Quantity in basket (g)**	**Quantity active (g)**	**Surface (m^2)**
Pt/Al_2O_3	93	Platinum	0.5	10.1	0.051	940
HTS	115	Transition	30	1.8	0.540	207
LTS	30	Transition (no Fe)	30	1.8	0.540	54

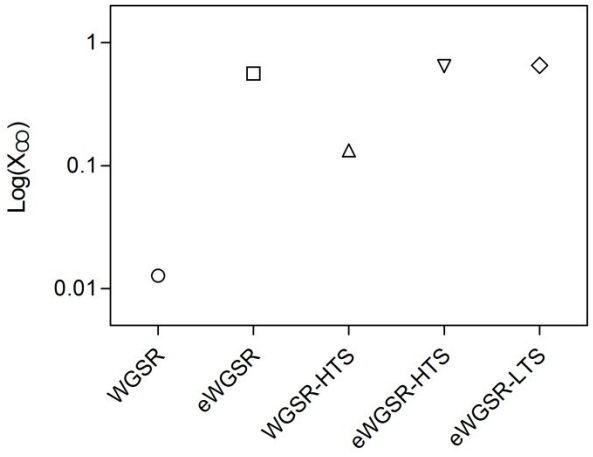

Figure 7.8: Effect of proprietary catalysts and slurry on the depletion of CO. The highest conversion was achieved in eWGSR-LTS, though eWGSR-HTS was very close, at 65.6% and 64.6% respectively. Without catalyst eWGSR depleted 56.0% of the initial CO. The tests without slurry resulted in less conversion with WGSR-HTS reaching13.3% and WGSR converting only 1.28%.

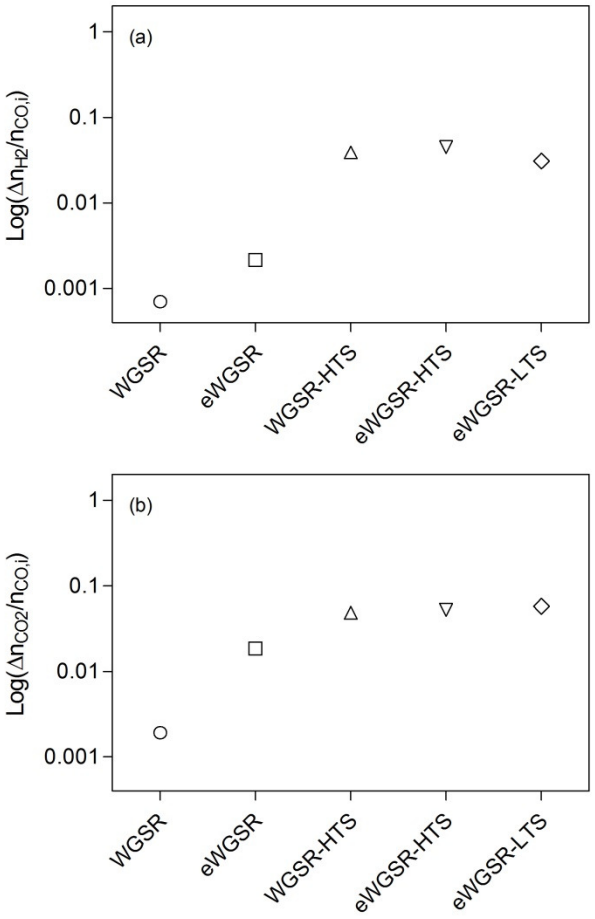

Figure 7.9: Effect of proprietary catalysts and slurry on the production of H_2 (a) and CO_2 (b) normalized to the initial moles of CO. The conversion of CO to H_2 was significantly lower than the experiments with Pt catalyst. WGSR-HTS, eWGSR-HTS, and eWGSR-LTS all achieved 3.8% conversion on average, while the non-catalytic tests produced minimal H_2. Similarly small amounts of CO_2 were formed follow the same trend as H_2 production, except for eWGSR which produced significantly more CO_2 than H_2 as the result of a side reaction likely involving formate.

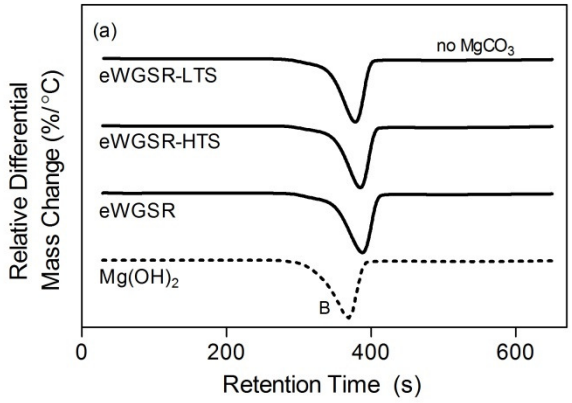

Figure 7.10: Thermal decomposition analysis in TGA of the solids recovered from eWGSR experiments compared against the reagent $Mg(OH)_2$. Label: brucite/$Mg(OH)_2$ (B). The result shows no mass change in the region where $MgCO_3$ decomposes. The concentration of CO_2 likely was not large enough to drive the carbonation reaction.

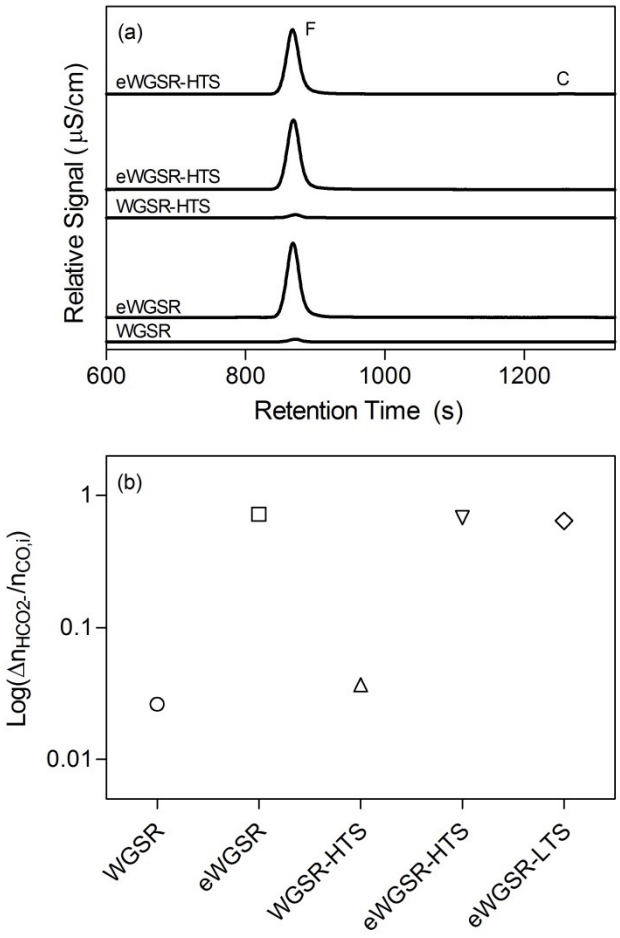

Figure 7.11: Liquid fraction of slurry analyzed via ion chromatography (IC). Samples diluted 50x prior to analysis. Graphs: IC output (a) and production of HCO_2^- normalized to the initial moles of CO. Labels: formate/HCO_2^- (F) and carbonate/CO_3^{2-} (C). More formate was present as compared to the experiments with Pt catalyst due to the increased amounts of CO found in the reactor during tests with HTS and LTS catalysts. Again, significant conversion of CO to HCO_2^- was observed in experiments with the slurry. The conversions for eWGSR, eWGSR-HTS, and eWGSR-LTS were 71.9%, 67.7%, and 64.3% respectively.

7.7.2. Enhanced WGSR Reactor Arrangements

Assuming the WGSR catalyst can be suspended in the slurry, something not investigated in the current study, various fluid-bed reactors could be utilized in the eWGSR system, including slurry reactors, bubble column reactors, and ebulating bed reactors. Figure 7.12 contains a schematic of a slurry bed system for eWGSR. The left side is a reactor for capturing CO_2 and performing forward WGSR. A heat exchange system is included in the case one would be required to remove heat (both carbonation and WGSR reactions are exothermic). The slurry regeneration reactor on the right separates $MgCO_3$ and includes the capability to regenerate the catalyst in cases of deactivation. Separation techniques similar to those used in FTS could be employed to achieve the catalyst/$MgCO_3$ separation. Passive or active sedimentation could separate based on specific gravity differences between the materials. Particle size differences can be exploited to separate using advanced filtration systems. If applicable, the separation scheme could be designed to separate magnetically active catalysts (Zhou & Srivastava, 1991).

The use of a slurry reactor system is advantageous in a number of ways. If gas distribution is done correctly, it is possible to achieve very good mixing and gas-liquid contact. The high degree of mixing helps to maintain a uniform gas composition throughout the reactor. Additionally, heat transfer, heat management, and temperature control are ideal in slurry systems due to the heat capacity of the liquid phase. Highly endothermic or exothermic reactions benefit greatly from the heat transfer properties. Lastly, catalyst regeneration could occur continuously by removing and treating a portion

of the slurry continuously and cycling it back to the reactor (Bartholomew & Farrauto, 2006).

Process design for the eWGSR system is expected to bring challenges, given the complex nature of multiphase reactor systems. Process complexities translate to increased costs associated with various complications and maintenance. Control over gas-liquid contact is a huge concern as large bubbles will decrease mass transfer rates significantly. As compared with other reactor types, slurry bed reactors experience limitations in the residence time range allowable, which could limit conversion. Also, depending on the catalyst, attrition and loss could be very expensive and also necessitate maintenance (Bartholomew & Farrauto, 2006).

The biggest issue expected when designing an integrated WGSR and slurry carbonation process is the efficient separation of catalyst and $MgCO_3$/$Mg(OH)_2$. The separation techniques mentioned above may not be economically or scientifically feasible for this separation. Also, the assumption that the WGSR catalyst could operate in the slurry phase would require significant research and development. Hence, an arrangement is proposed which integrates slurry carbonation of $Mg(OH)_2$ with the WGSR in separate stages. The schematic in Figure 7.13 depicts a conventional HTS reactor, which exploits the faster WGSR kinetics at high temperature to achieve significant conversion quickly. The effluent is sent to a bubble column carbonation system where the syngas is contacted with the $Mg(OH)_2$ slurry to remove the CO_2. The last step depends on the degree of CO conversion required for downstream applications. A recycle stream could ensure a higher degree of carbon capture and also a slightly higher WGSR conversion was achieved. Alternatively, the bubble column effluent could pass to a LTS reactor to remove the

remaining CO. The Sorbent separator can operate by filtration or sedimentation. In both slurry bed and bubble column schemes, the issue of formate buildup within the system as CO reacts with dissolved hydroxide ions must be considered. Various techniques for facilitating its decomposition to desired products are contained in the article.

An alternative to the bubble column is proposed in Figure 7.14. A spray tower fed with a $Mg(OH)_2$ slurry could simplify the $MgCO_3$ separation. The slurry provides the required H_2O for WGSR and as the liquid bubbles vaporize the $Mg(OH)_2$ carbonates to form dry $MgCO_3$ which falls to the reactor bottom for collection. The CO_2-free syngas exits the top of the reactor. Again, the schematic includes the possibility to either recycle a portion of the spray tower effluent or send it to a LTS reactor to achieve a specific conversion of CO. In the spray tower scenario, the issue of formate build-up may be minimized due to the lack of a bulk aqueous phase.

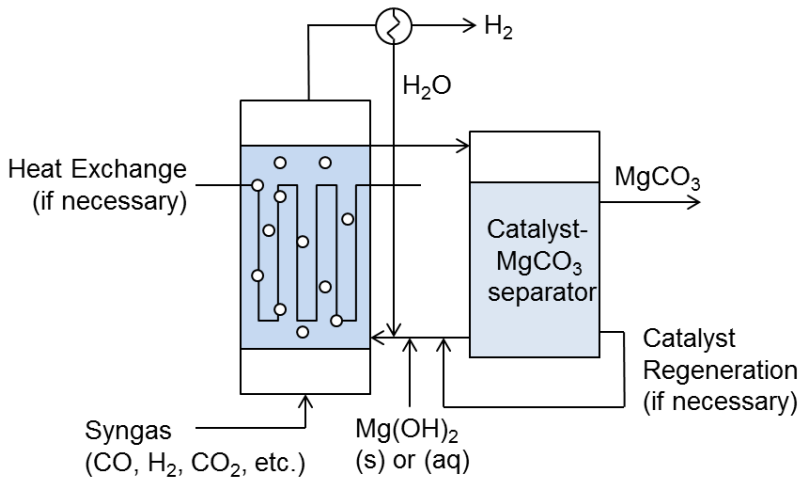

Figure 7.12: Slurry Bed reactor system.

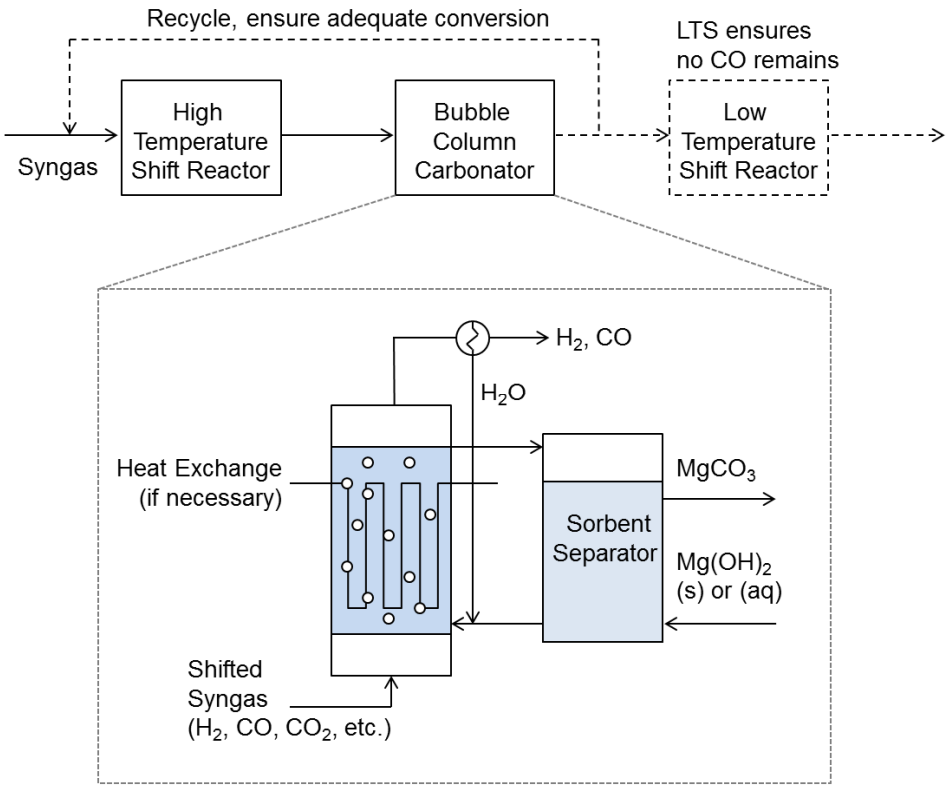

Figure 7.13: Bubble column carbonation in series with conventional WGSR reactor(s).

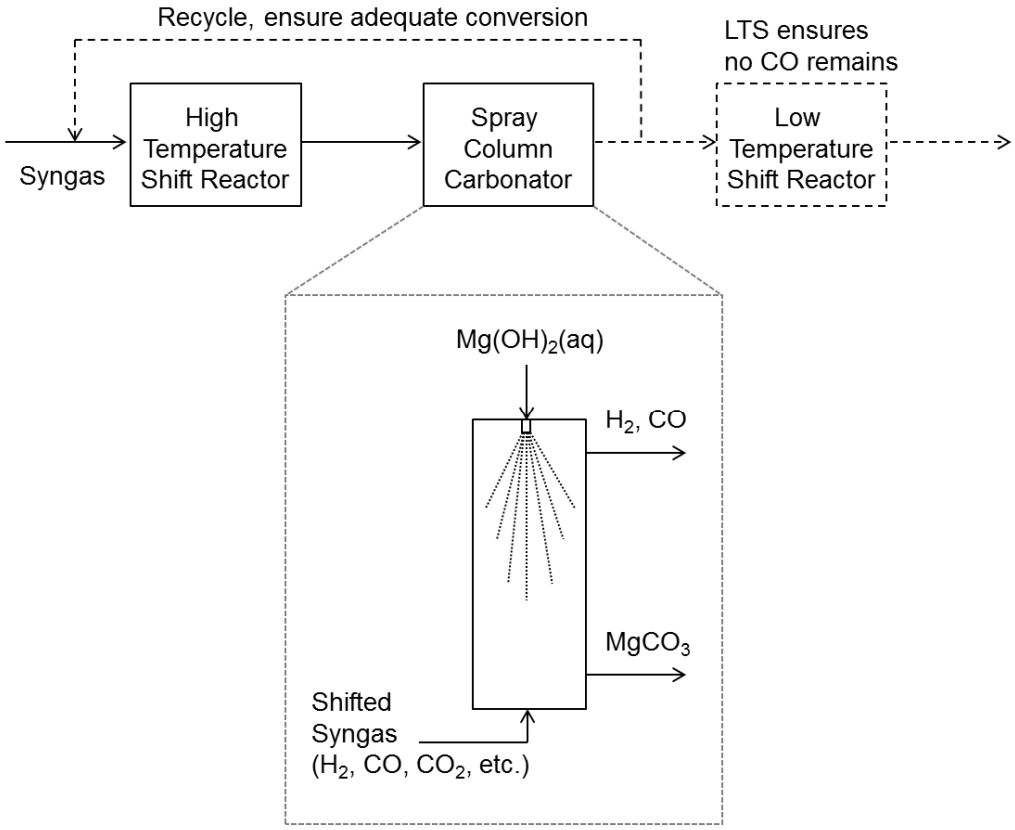

Figure 7.14: Spray tower carbonation in series with conventional WGSR reactor(s).

8. Conclusions and Suggestions for Future Work

8.1. Conclusions

This study aimed to systematically evaluate the carbonation of a $Mg(OH)_2$ sorbent and investigate its integration with an energy conversion reaction (WGSR). The combined CO_2 capture and storage technology was given perspective through a literature review and life cycle assessment of a theoretical process for converting waste plastics to liquid fuels with integrated $Mg(OH)_2$ carbonation. The fundamental chemistry of both gas-solid and slurry phase $Mg(OH)_2$ carbonation were probed to reveal the enhanced effect of H_2O, the dominant effect of temperature on carbonate phase formation in aqueous systems, and the ability to direct precipitation of anhydrous carbonate through the use of seeds. The integration of the $Mg(OH)_2$ carbonation system with the multiphase WGSR reactor system revealed the enhanced effect of slurry carbonation on hydrogen yield. Ultimately, this study expanded the understanding of the $Mg(OH)_2$ carbonation system and assessed its application within a syngas upgrading process.

To bring perspective to the $Mg(OH)_2$ carbonation system, its integration with a waste-to-liquids process was considered in Chapter 3. The combined CO_2 capture and storage process is integrated at the point of CO_2 generation, within the WGSR. On either side of the WGSR/carbonation system lie well developed technologies: gasification for syngas production and FTS to build hydrocarbon chemicals and fuels from shifted syngas. A study of the literature revealed the complexity and customizability of the gasification system. Interestingly, plastics were typically found to enhance the gasification characteristics of mixed feedstocks. An LCA study of the conversion of waste plastics to

diesel fuel via gasification and FTS confirmed literature regarding the carbon intensity of such processes. CCS integration proved to be a requirement to improve the waste-to-liquids process sustainability.

Gas-solid carbonation of $Mg(OH)_2$ has been studied for many years and is generally limited in terms of kinetics and overall conversion. This study explored the limitations, finding that carbonation at low temperature and P_{CO2} was not feasible. Increased temperature and P_{CO2} (400 °C and 10 atm) provided more conversion, though the absolute quantity was still low (< 20%). The presence of steam was shown to enhance $Mg(OH)_2$ carbonation reaction kinetics as well as allow for significantly higher conversion to carbonate (almost 70%). Mechanistic studies revealed the possibility of an alternative reaction pathway where $Mg(OH)_2$ first reacts relatively quickly with CO_2 in the presence of H_2O to form hydrated magnesium carbonate intermediate, which can decompose to form anhydrous $MgCO_3$ given the reaction conditions. A trend linking the increased H_2O loading to the formation of anhydrous carbonate was confirmed, and a slurry (H_2O rich) carbonation test at the same temperature showed the complete conversion to anhydrous $MgCO_3$.

The limitations of the gas-solid carbonation system—even at very high temperature, P_{CO2}, and P_{H2O}—combined with the known high reactivity of aqueous $Mg(OH)_2$ and the lack of research on the slurry phase carbonation system at elevated temperature and P_{CO2} motivated a full study of $Mg(OH)_2$ slurry carbonation. This study focused on understanding the temperature effect on the reaction kinetics and type of carbonate phase formed during slurry phase $Mg(OH)_2$ carbonation. Though generally desired for its efficiency in CCS scenarios, the formation of anhydrous $MgCO_3$ is complicated by the

metastability of various hydrated magnesium carbonates (namely nesquehonite and hydromagnesite). By fixing the temperature, a pure carbonate phase could be formed from the $Mg(OH)_2$ slurry after 120 min at a P_{CO2} of 15 atm. The low temperature study resulted in the relatively slow formation of nesquehonite, which upon complete conversion, equilibrated with the excess P_{CO2} to partially dissolve. Moderate temperatures favor the production of hydromagnesite at the same conditions. A study of various parameters, e.g. reaction time, CO_2 injection temperature, aging up to 18 hours, and CO_2 concentration (fixed amount of CO_2 or constant CO_2 pressure), confirmed the dominant effect of temperature on carbonate phase determination. At the moderate temperature, solution additives enabled the formation of anhydrous carbonate where it would otherwise not be formed. The combined effect of bicarbonate and NaCl provided the highest conversion to $MgCO_3$ due to the faster carbonation and dissolution rates, as well as the interference with the hydration shell surrounding Mg^{2+}(aq). High temperature experiments produced magnesite readily. The XRD time series indicated that a hydromagnesite intermediate may have formed during high temperature tests.

A subsequent study aimed to investigate another technique for enabling magnesite formation at conditions where the metastable hydrate magnesium carbonates tend to form and persist for long periods of time. Ultimately, the slow kinetics of magnesite nucleation leads to the production of metastable species, which reduce the process efficiency and impact the permanence associated with CO_2 storage via mineralization. A review of the literature was conducted, and select studies were modeled to determine the highest saturation index possible during their experiments. The absence of definite relationships between magnesium carbonate phase formation and various reaction parameters (e.g.

saturation index, temperature, and P_{CO2}) warranted a new approach to directing precipitation of a specific phase. The effect of seeding the $Mg(OH)_2$ slurry carbonation system with both inert (alumina) and anhydrous carbonate ($MgCO_3$) was investigated at 150 °C and 15 atm of CO_2. Unseeded and inert-seeded reactions produced hydromagnesite. In the case of the inert seeds, the hydrated carbonate had a more defined structure given the insoluble surfaces to precipitate on. On the other hand, the magnesite-seeded system produced pure magnesite at reasonable rates, bypassing the formation of hydromagnesite. The presence of magnesite seed particles enables the system to circumvent nucleation and begin crystal growth at the start of reaction. Growth of magnesite at temperatures below 150 °C was demonstrated via magnesite-seeding, though the co-precipitation of hydromagnesite and magnesite was observed at lower temperatures. An industrial carbon storage process could utilize a slip stream of the magnesite product to seed the production of new magnesite in the carbon mineralization reactor.

The fundamental understanding of $Mg(OH)_2$ as a sorbent material for process integrated CO_2 capture and storage was applied to the WGSR to both decarbonize the process as well as shift its equilibrium and enhance hydrogen production. Given the improved carbonation kinetics and conversion in the aqueous phase, a high pressure slurry phase carbonation WGSR system was explored. The WGSR required Pt catalyst to achieve significant conversion, and thus, provide enough CO_2 to drive carbonation and the enhanced effect on hydrogen production. Interestingly, the production of hydrogen was less than expected, given the depletion of CO, especially in experiments that utilized the $Mg(OH)_2$ slurry (eWGSR). A side reaction between CO and hydroxide ions in

solution to produce formate ions limited the overall conversion of the conventional, gas-phase WGSR. Formate in solution can decompose, yielding H_2, though the high concentration of Mg^{2+} likely led to highly soluble magnesium formate complex formation. Nevertheless, the presence of the slurry did enhance hydrogen production by shifting the WGSR equilibrium as CO_2 was mineralized. Techniques for promoting formate decomposition were reviewed, and various reactor arrangements were proposed.

8.2. Future Work

The limitations in kinetics and overall conversion experienced in the gas-solid carbonation system could be addressed through the use of synthesized, engineered sorbent particles. $Mg(OH)_2$ sorbents can be synthesized with optimized internal/external surface area and a mesoporous framework capable of managing the buildup of carbonates to avoid the formation of a mass transfer inhibiting carbonate passivation layer. The investigation could include the effect of sorbent additives, like NaOH, which have demonstrated improved CaO carbonation rates and sorbent stability characteristics (Stevens *et al.*, 2010). The step-wise synthesis of an optimized $Mg(OH)_2$ sorbent from magnesium silicate mineral must also be explored. Most of the research in the Park Group and elsewhere has focused on understanding the dissolution of magnesium silicates and aqueous carbonation processes separately, using model systems for the latter. Sustainable production of an engineered $Mg(OH)_2$ sorbent material from magnesium silicates using an adapted pH swing procedure is an area apt for research.

Gas-solid carbonation of $Mg(OH)_2$ could also benefit from the investigation of new reactor designs. A more robust fixed bed reactor system could explore the effect of steam

on carbonation at a wider range of P_{CO2} and P_{H2O} than were tested in this study. Alternatively, a fluidized bed reactor could bring a solution to the passivation layer problem, since particle-particle interactions will result in attrition and removal of surface carbonates. A pressurized fluidized bed provided significant carbonation benefits in the $Mg(OH)_2$ carbonation system (Fagerlund *et al.*, 2010).

The $Mg(OH)_2$ slurry carbonation system could also benefit from the sorbent synthesis from magnesium silicate mineral study. The energy and material inputs must be understood completely to resolve the sustainability of the overall system. A similar reactor system could be used to investigate other carbonation media, such as various industrial wastes. A second generation slurry carbonation reactor should also include a high pressure pH probe to measure pH in situ at elevated temperature and pressure to better understand the phenomena inside the reactor. Catalysts for facilitating CO_2 dissolution and hydration should be investigated as well.

Given the inefficiencies in producing the metastable hydrated carbonates, future research in the aqueous magnesium carbonation system can expand on this study to further investigate the used of solution additives, seeds in particular, to generate a pure, controlled $MgCO_3$. Future work can evaluate the effect of additive concentration and decipher the enhancement mechanism more completely. The effect of additive at controlling the product morphology should also be considered. The potential to utilize undesirable brines in the process to improve the water sustainability as well as drive magnesite formation could be explored. The fundamental chemistry studies can be complimented with an expanded modeling effort and, macroscopically, process design considerations.

Fundamental mechanistic studies can supplement the studies of both gas-solid and slurry phase carbonation. In-situ spectroscopy (Hänchen *et al.*, 2008) and X-ray diffraction (Schaef *et al.*, 2011) are demonstrated and should be used to understand carbonation at a wider range of temperature, pressure, and solution conditions. Isotope tracking helped elucidate the mechanism of $Mg(OH)_2$ in wet supercritical CO_2 and could be further used in a variety of experimental and reactor arrangements to provide insight into the mechanisms (Schaef *et al.*, 2011).

The WGSR integrated carbonation system would benefit greatly from further testing and study. Significant gas-solid carbonation improvements through sorbent and reactor optimization could motivate an investigation of its integration with conventional, heterogeneously catalyzed WGSR. For example, the reactions could be incorporated in a pressurized fluidized bed test rig. In the slurry phase carbonation arrangement, the buildup of formate in solution must be addressed according to Figure 7.7, most likely through homo- or heterogeneous catalysis. In both scenarios, building an experimental continuous reactor system is ideal. A modeling effort in fluid dynamics and chemical/physical separations could address the concerns of the various reactor systems contained in Section 7.7.2.

After further fundamentals of the chemistry are deciphered and process understanding is developed beyond the bench scale, an expansion of the life cycle assessment (LCA) from both environmental and economic perspectives would guide future process development. The LCA of the waste-to-liquid, presented in Section 3.4, could be expanded with more parameters to assess the impacts of waste use and CCS on the fuel production process and how it compares to other waste management processes and fuel

processing methods from different feedstocks. Sorbent synthesis and product use or disposal must also be considered. The broadened context may reveal that some previous assumptions are not necessarily valid. For example, beneficially using the carbonate product in building materials may necessitate hydrated carbonate product of specific morphology (Gadikota *et al.*, 2014).

9. References

I.I. Ahmed, N. Nipattummakul and A.K. Gupta (2011). "Characteristics of syngas from co-gasification of polyethylene and woodchips." *Appl. Energ.* **88**(1): 165-174.

M. Aznar, M. Caballero, J. Sancho, et al. (2006). "Plastic waste elimination by co-gasification with coal and biomass in fluidized bed with air in pilot plant." *Fuel Process. Technol.* **87**(5): 409-420.

P. Ballirano, C. De Vito, V. Ferrini, et al. (2010). "The thermal behaviour and structural stability of nesquehonite, MgCO3·3H2O, evaluated by in situ laboratory parallel-beam X-ray powder diffraction: New constraints on CO2 sequestration within minerals." *J. Hazard. Mater.* **178**(1-3): 522-528.

C.H. Bartholomew and R.J. Farrauto (2006). Fundamentals of Industrial Catalytic Processes, Wiley.

H. Béarat, M.J. McKelvy, A.V.G. Chizmeshya, et al. (2002). "Magnesium Hydroxide Dehydroxylation/Carbonation Reaction Process: Implication for Carbon Dioxide Mineral Sequestration." *J. Am. Ceram. Soc.* **85**(4): 742-748.

P. Bénézeth, G.D. Saldi, J.-L. Dandurand, et al. (2011). "Experimental determination of the solubility product of magnesite at 50 to 200°C." *Chem. Geol.* **286**(1-2): 21-31.

D.T. Beruto and R. Botter (2000). "Liquid-like H2O adsorption layers to catalyze the Ca(OH)2/CO2 solid-gas reaction to form a non-protective solid product layer at 20 C." *J. Euro. Ceram. Soc.* **20**: 497-503.

C. Bethke (2008). The Geochemist's Workbench Release 7.0.2., University of Illinois, Urbana.

A. Boddien, F. Gärtner, C. Federsel, et al. (2011). "CO2-"Neutral" Hydrogen Storage Based on Bicarbonates and Formates." *Angew. Chem. Int. Edit.* **50**(28): 6411-6414.

A. Boddien, D. Mellmann, F. Gartner, et al. (2011). "Efficient Dehydrogenation of Formic Acid Using an Iron Catalyst." *Science* **333**(6050): 1733-1736.

C. Borgianni, P. De Filippis, F. Pochetti, et al. (2002). "Gasification process of wastes containing PVC." *Fuel* **81**: 1827-1833.

A. Botha and C.A. Strydom (2001). "Preparation of a magnesium hydroxy carbonate from magnesium hydroxide." *Hydrometallurgy* **62**: 175-183.

A. Boudjemaa, A. Auroux, S. Boumaza, et al. (2009). "Hydrogen production on iron–magnesium oxide in the high-temperature water-gas shift reaction." *React. Kinet. Catal. L.* **98**(2): 319-325.

S. Boxiong, W. Chunfei and Q. Lei (2006). "MSW catalytic combusion by alkali and alkali-earth salts." *Energy* **31**(14): 2900-2914.

D.P. Butt, K.S. Lackner, C.H. Wendt, et al. (1996). "Kinetics of Thermal Dehydroxylation and Carbonation of Magnesium Hydroxide." *J. Am. Ceram. Soc.* **79**(7): 1892-1898.

W. Cheng and Z. Li (2009). "Precipitation of nesquehonite from homogeneous supersaturated solutions." *Cryst. Res. Technol.* **44**(9): 937-947.

W. Cheng and Z. Li (2010). "Controlled Supersaturation Precipitation of Hydromagnesite for the MgCl2–Na2CO3 System at Elevated Temperatures: Chemical Modeling and Experiment." *Ind. Eng. Chem. Res.* **49**(4): 1964-1974.

D.-H. Choi, J.B. Lee, T.H. Eom, et al. (2013). "Study of MgO-based dry regenerable sorbent for sorption enhanced water gas shift reaction." *Renew. Energ.* **54**: 144-149.

M. Czaun, A. Goeppert, R. May, et al. (2011). "Hydrogen Generation from Formic Acid Decomposition by Ruthenium Carbonyl Complexes. Tetraruthenium Dodecacarbonyl Tetrahydride as an Active Intermediate." *ChemSusChem* **4**(9): 1241-1248.

D. Dasgupta, K. Mondal and T. Wiltowski (2008). "Robust, high reactivity and enhanced capacity carbon dioxide removal agents for hydrogen production applications." *Int. J. Hydrogen Energ.* **33**(1): 303-311.

P.J. Davies and B. Bubela (1973). "The Transformation of Nesquehonite into Hydromagnesite." *Chem. Geol.* **12**: 289-300.

A. De Visscher, J. Vanderdeelen, E. Königsberger, et al. (2012). "IUPAC-NIST Solubility Data Series. 95. Alkaline Earth Carbonates in Aqueous Systems. Part 1. Introduction, Be and Mg." *J. Phys. Chem. Ref. Data* **41**(1): 013105.

J.C. Deelman (2001). "Breaking Ostwald's Rule." *Chem. Erde-Geochem.* **61**(3): 224-235.

D. Dollimore and J.P.N. Gupta, D. V. (1979). "The Thermal Decomposition of Metal Formates. II. Solid State Thermal Decomposition Studies on Magneisum Formate Dihydrate." *Thermochim. Acta* **30**: 339-350.

M. Dong, W. Cheng, Z. Li, et al. (2008). "Solubility and Stability of Nesquehonite (MgCO3•3H2O) in NaCl, KCl, MgCl2, and NH4Cl Solutions." *J. Chem. Eng. Data* **53**(11): 2586-2593.

M. Donnet, P. Bowen, N. Jongen, et al. (2005). "Use of Seeds to Control Precipitation of Calcium Carbonate and Determination of Seed Nature." *Langmuir* **21**(1): 100-108.

R.T. Downs (2006). "The RRUFF Project: an integrated study of the chemistry, crystallography, Raman and infrared spectroscopy of minerals." *Program and Abstracts of the 19th General Meeting of the International Mineralogical Association in Kobe, Japan* **O03-13**.

Z. Duan, R. Sun, C. Zhu, et al. (2006). "An improved model for the calculation of CO2 solubility in aqueous solutions containing Na+, K+, Ca2+, Mg2+, Cl−, and SO42−." *Mar. Chem.* **98**(2-4): 131-139.

H. Edwards, S. Villar, J. Jehlicka, et al. (2005). "FT–Raman spectroscopic study of calcium-rich and magnesium-rich carbonate minerals." *Spectrochim. Acta A* **61**(10): 2273-2280.

EIA (2008). U.S. Energy Information Administration Retreived from http://www.eia.gov/.

EIA (2013). Annual Energy Outlook 2013 with Projections to 2040, US Energy Information Agency.

D.C. Elliott, R.T. Hallen and L.J. Sealock (1983). "Aqueous Catalyst Systems for the Water-Gas Shift Reaction. 2. Mechanism of Basic Catalysts." *Ind. Eng. Chem. Prod. Res. Dev.* **22**: 431-435.

D.C. Elliott and L.J. Sealock (1983). "Aqueous Catalyst Systems for the Water-Gas Shift Reaction. 1. Comparitive Catalyst Studies." *Ind. Eng. Chem. Prod. Res. Dev.* **22**: 426-431.

S. Enthaler, J. von Langermann and T. Schmidt (2010). "Carbon dioxide and formic acid—the couple for environmental-friendly hydrogen storage?" *Energ. Environ. Sci.* **3**(9): 1207.

EPA (2012). Municipal Solid Waste (MSW) in the Uniter States: Facts and Figures.

R.M. Espinosa-Marzal and G.W. Scherer (2010). "Mechanisms of damage by salt." *Geol. Soc. London, Spec. Pub.* **331**: 61-77.

R.L. Evans and H.W. St. Clair (1949). "Carbonation of Aqueous Suspensions containing Magnesium Oxides or Hydroxides." *Ind. Eng. Chem.* **41**(12): 2814-2817.

J. Fagerlund, J. Highfield and R. Zevenhoven (2012). "Kinetics studies on wet and dry gas–solid carbonation of MgO and Mg(OH)2 for CO2 sequestration." *RSC Adv.* **2**(27): 10380.

J. Fagerlund, E. Nduagu, I. Romão, et al. (2010). "A stepwise process for carbon dioxide sequestration using magnesium silicates." *Front. Chem. Eng. China* **4**(2): 133-141.

J. Fagerlund, E. Nduagu, I. Romão, et al. (2011). "CO2 fixation using magnesium silicate minerals part 1: Process description and performance." *Energy* **41**: 184-191.

J. Fagerlund, E. Nduagu and R. Zevenhoven (2011). "Recent developments in the carbonation of serpentinite derived Mg(OH)2 using a pressurized fluidized bed." *Energy Procedia* **4**: 4993-5000.

J. Fagerlund and R. Zevenhoven (2011). "An experimental study of Mg(OH)2 carbonation." *Int. J. Greenhouse Gas Control* **5**: 1406-1412.

Z. Fan, L. Yuan and R. Chatterjee (2009). "Increased Hydrogen Production by Genetic Engineering of Escherichia coli." *PLoS ONE* **4**(2): 1-8.

B. Feng, H. An and E. Tan (2007). "Screening of CO2 Absorbing Materials for Zero Emission Power Generation Systems." *Energ. Fuel* **21**: 426-434.

A.I. Fernández, J.M. Chimenos, M. Segarra, et al. (2000). "Procedure to Obtain Hydromagnesite from a Mg-O-Containing Residue. Kinetic Study." *Ind. Eng. Chem. Res.* **39**: 3653-3658.

V. Ferrini, C. De Vito and S. Mignardi (2009). "Synthesis of nesquehonite by reaction of gaseous CO2 with Mg chloride solution: Its potential role in the sequestration of carbon dioxide." *J. Hazard. Mater.* **168**(2-3): 832-837.

K.J. Fricker and A.-H.A. Park (2013). "Effect of H2O on Mg(OH)2 carbonation pathways for combined CO2 capture and storage." *Chem. Eng. Sci.* **100**: 332-341.

K.J. Fricker and A.-H.A. Park (2014). "Enhanced Water Gas Shift Reaction in the Presence of a Mg(OH)2 slurry in a High Pressure Aqueous System." *Int. J. Hydrogen Energ. (in Review).*

K.J. Fricker and A.-H.A. Park (2014). "Investigation of the Different Carbonate Phases and their Formation Kinetics during Mg(OH)2 Slurry Carbonation." *Ind. Eng. Chem. Res. (in Review).*

R.L. Frost (2011). "Raman spectroscopic study of the magnesium carbonate mineral hydromagnesite (Mg5[(CO3)4(OH)2]· 4H2O)." *J. Raman Spectrosc.* **42**(8): 1690-1694.

G. Gadikota, K.J. Fricker, S.-H. Jang, et al. (2014). "Carbonated silicate minerals and industrial wastes as construction materials." *Minerals (in Review).*

G. Gadikota, J. Matter, P.B. Kelemen, et al. (2014). "Chemical and Morphological Changes during Olivine Carbonation for CO2 Storage in the presence of NaCl and NaHCO3." *Phys. Chem. Chem. Phys.* **16**(10): 4679-4693.

D.E. Giammar, R.G. Bruant and C.A. Peters (2005). "Forsterite dissolution and magnesite precipitation at conditions relevant for deep saline aquifer storage and sequestration of carbon dioxide." *Chem. Geol.* **217**(3-4): 257-276.

F. Goff and K.S. Lackner (1998). "Carbon Dioxide sequestering using ultramafic rocks." *Environ. Geosci.* **5**(3): 89-101.

M.C. Hales, R.L. Frost and W.N. Martens (2008). "Thermo-Raman spectroscopy of synthetic nesquehonite - implication for the geosequestration of greenhouse gases." *J. Raman Spectrosc.* **39**(9): 1141-1149.

A.L. Harrison, I.M. Power and G.M. Dipple (2013). "Accelerated Carbonation of Brucite in Mine Tailings for Carbon Sequestration." *Environ. Sci. Technol.* **47**(1): 126-134.

D.P. Harrison (2008). "Sorption-Enhanced Hydrogen Production: A Review." *Ind. Eng. Chem. Res.* **47**: 6486-6501.

A. Hassanzadeh and J. Abbasian (2010). "Regenerable MgO-based sorbents for high-temperature CO2 removal from syngas: 1. Sorbent development, evaluation, and reaction modeling." *Fuel* **89**(6): 1287-1297.

M. He, Z. Hu, B. Xiao, et al. (2009). "Hydrogen-rich gas from catalytic steam gasification of municipal solid waste (MSW): Influence of catalyst and temperature on yield and product composition." *Int. J. Hydrogen Energ.* **34**(1): 195-203.

M. He, B. Xiao, Z. Hu, et al. (2009). "Syngas production from catalytic gasification of waste polyethylene: Influence of temperature on gas yield and composition." *Int. J. Hydrogen Energ.* **34**(3): 1342-1348.

C. Higman and M. van der Burgt (2008). Gasification. Amsterdam, Elsevier.

M. Höök and K. Aleklett (2009). "A review on coal-to-liquid fuels and its coal consumption." *Int. J. Energ. Res.*

L. Hopkinson, P. Kristova, K. Rutt, et al. (2012). "Phase transitions in the system MgO–CO2–H2O during CO2 degassing of Mg-bearing solutions." *Geochim. Cosmochim. Ac.* **76**: 1-13.

J. Hövelmann, C.V. Putnis, E. Ruiz-Agudo, et al. (2012). "Direct Nanoscale Observations of CO2 Sequestration during Brucite [Mg(OH)2] Dissolution." *Environ. Sci. Technol.* **46**(9): 5253-5260.

G.W. Huber, S. Iborra and A. Corma (2006). "Synthesis of Transportation Fuels from Biomass: Chemistry, Catalysts, and Engineering." *Chem. Rev.* **106**(9): 4044-4098.

M. Hänchen, V. Prigiobbe, R. Baciocchi, et al. (2008). "Precipitation in the Mg-carbonate system—effects of temperature and CO2 pressure." *Chem. Eng. Sci.* **63**(4): 1012-1028.

IEA (2010). World Energy Outlook. International Energy Agency, Retrieved from http://www.oecd-ilibrary.org/.

IEA (2013). World Energy Outlook. International Energy Agency, Retrieved from http://www.oecd-ilibrary.org/.

IPCC (2005). Carbon Dioxide Capture and Storage. New York, Intergovernmental Panel on Climate Change.

IPCC (2005). IPCC Special Report on CCS. UK, Cambridge University Press.

IPCC (2007). Climate Change 2007. New York, Intergovernmental Panel on Climate Change (IPCC).

IPCC (2013). Climate Change 2013 The Physical Science Basis. New York, Intergovernmental Panel on Climate Change (IPCC).

H. Ishida, K. Tanaka, M. Morimoto, et al. (1986). "Isolation of Intermediates in the Water Gas Shift Reactions Catalyzed by [Ru(bpy)2(CO)Cl]+ and [Ru(bpy)2(CO)2]2+ " *J. Am. Chem. Soc.* **5**: 724-730.

S.K. Jeon, C.S. Park, C.E. Hackett, et al. (2007). "Characteristics of steam hydrogasification of wood using a micro-batch reactor." *Fuel* **86**(17-18): 2817-2823.

B. Johnke (2001). Emissions from Waste Incineration. Good Practice Guidance and Uncertainty Management in National Greenhouse Gas Inventories.

W. Kaminsky (2006). Feedstock Recycling and Pyrolysis of Waste Plastics. Hoboken, New Jersey, Wiley.

O. Karoussi and A.A. Hamouda (2007). "Imbibition of Sulfate and Magnesium Ions into Carbonate Rocks at Elevated Temperatures and Their Influence on Wettability Alteration and Oil Recovery." *Energ. Fuel* **21**: 2138-2146.

P.B. Kelemen, G. Savage and G. Hirth (2013). "Reaction-Driven Cracking During Mineral Hydration, Carbonation and Oxidation." *Poromechanics V: Proceedings of the Fifth Biot Conference on Poromechanics*: 823-826.

J.Y.H. Kim, B. Jo and H. Cha (2010). "Production of biohydrogen by recombinant expression of [NiFe]-hydrogenase 1 in Escherichia coli." *Microb. Cell Fact.* **9**(1): 54.

A.D. King, R.B. King and D.B. Yang (1980). "Homogeneous Catalysis of the Water Gas Shift Reaction Using Iron Pentacarbonyl." *J. Am. Chem. Soc.* **102**(3): 1028-1032.

J.A. Kittrick and F.I. Peryea (1986). "Determination of the Gibbs Free Energy of Formation of Magnesite by Solubility Methods." *Soil Sci. Soc. Am. J.* **50**: 243-247.

J.T. Kloprogge, W.N. Martens, L. Nothdurft, et al. (2003). "Low temperature synthesis and characterization of nesquehonite." *J. Mater. Sci. Lett.* **22**(11): 825-829.

K.M. Krupka, K.J. Cantrell and B.P. McGrail (2010). Thermodynamic Data for Geochemical Modeling of Carbonate Reactions Associated with CO2 Sequestration -- Literature Review,. Richland, Washington, Pacific Northwest National Laboratory**:** 135.

J.H. Kwak, J.Z. Hu, D.W. Hoyt, et al. (2010). "Metal Carbonation of Forsterite in Supercritical CO2 and H2O Using Solid State 29Si, 13C NMR Specroscopy." *J. Phys. Chem. C* **114**: 4126-4134.

J.H. Kwak, J.Z. Hu, R.V.F. Turcu, et al. (2011). "The role of H2O in the carbonation of forsterite in supercritical CO2." *Int. J. Greenhouse Gas Control* **5**(4): 1081-1092.

H. Kwon and D.G. Park (2009). "Infra-Red Study of Surface Carbonation on Polycrystalline Magnesium Hydroxide." *Bull. Korean Chem. Soc.* **30**(11): 2567-2573.

S. Kwon (2011). Mineralization for CO2 Sequestration using Olivine Sorbent in the Presence of Water Vapor. Civil and Environmental Engineering, Georgia Institute of Technology. **Ph.D.**

K.S. Lackner (2009). "Capture of carbon dioxide from ambient air." *Eur. Phys. J.-Spec. Top.* **176**(1): 93-106.

K.S. Lackner, C.H. Wendt, D.P. Butt, et al. (1995). "Carbon dioxide disposal in carbonate minerals." *Energy* **20**(11): 1153-1170.

R.M. Laine and E.J. Crawford (1988). "Homogeneous Catalysis of the Water-Gas Shift Reaction." *J. Mol. Catal.* **44**: 357-387.

D. Langmuir (1965). "Stability of Carbonates in the System MgO-CO2-H2O." *J. Geol.* **73**(5): 730-754.

F. Larachi, J.P. Gravel, B.P.A. Grandjean, et al. (2012). "Role of steam, hydrogen and pretreatment in chrysotile gas–solid carbonation: Opportunities for pre-combustion CO2 capture." *Int. J. Greenhouse Gas Control* **6**: 69-76.

P.-C. Lin, C.-W. Huang, C.-T. Hsiao, et al. (2008). "Magnesium Hydroxide Extracted from a Magnesium-Rich Mineral for CO2 Sequestration in a Gas-Solid System." *Environ. Sci. Technol.* **42**: 2748-2752.

L. Lloyd, D.E. Ridler and M.V. Twigg (1989). The Water-gas Shift Reaction. London, Wolfe Publishing Ltd.

J.S. Loring, C.J. Thompson, C. Zhang, et al. (2012). "In Situ Infrared Spectroscopic Study of Brucite Carbonation in Dry to Water-Saturated Supercritical Carbon Dioxide." *J. Phys. Chem. A*: 120503083945007.

J.J. Marano and J.P. Ciferno (2001). Life-Cycle Greenhouse-Gas Emissions Inventory For Fischer-Tropsch Fuels, Energy and Environmental Solutions, LLC.

L. Marini (2007). Geological Sequestration of Carbon Dioxide: Thermodynamics, Kinetics, and Reaction Path Modeling. Amsterdam, Elsevier.

M.L. Mastellone, L. Zaccariello and U. Arena (2010). "Co-gasification of coal, plastic waste and wood in a bubbling fluidized bed reactor." *Fuel* **89**(10): 2991-3000.

M.J. McKelvy, R. Sharma, A.V.G. Chizmeshya, et al. (2001). "Magnesium Hydroxide Dehydroxylation: In Situ Nanoscale Observations of Lamellar Nucleation and Growth." *Chem. Mater.* **13**: 921-926.

D.W. Ming and W.T. Franklin (1985). "Synthesis and Characterization of Lansfordite and Nesquehonite." *Soil Sci. Soc. Am. J.* **49**(5): 1303-1308.

K. Mitsuhashi, N. Tagami, K. Tanabe, et al. (2005). "Synthesis of Microtubes with a Surface of 'House of Cards' Structure via Needlelike Particles and Control of Their Pore Size." *Langmuir* **21**(8): 3659-3663.

P. Möller (1989). Magnesite: geology, mineralogy, geochemistry, formation of Mg-carbonates. Berlin-Stuttgart, Gebrueder Borntraeger.

J. Morris (2005). "Comparative LCAs for Curbside Recycling Versus Either Landfilling or Incineration with Energy Recovery." *Int. J. LCA* **10**(4): 273-284.

K. Nishida, D. Li, Y. Zhan, et al. (2009). "Effective MgO surface doping of Cu/Zn/Al oxides as water–gas shift catalysts." *Appl. Clay Sci.* **44**(3-4): 211-217.

NIST. "Chemistry WebBook."

W.K. O'Connor, C.L. Dahlin, G.E. Rush, et al. (2004). Final report: Aqueous mineral carbonation.

O.-T. Onsager, M.S.A. Brownrigg and R. Lodeng (1996). "Hydrogen Production from Water and CO via Alkali Metal Formate Salts." *Int. J. Hydrogen Energ.* **21**(10): 883-885.

Outotec HSC Chemistry. Software.

S. Pacala and R. Socolow (2004). "Stabilization Wedges: Solving the Climate Problem for the Next 50 Years with Current Technologies." *Science* **205**(5686): 968-972.

A.-H.A. Park (2005). Carbon Dioxide Sequestration: Chemical and Physical Acitivation of Aqueous Carbonation of Mg-Bearing Minerals and pH Swing Process. Chemical Engineering, Ohio State Univesity. **Ph. D.**

A.-H.A. Park and L. Fan (2004). "Mineral sequestration: physically activated dissolution of serpentine and pH swing process." *Chem. Eng. Sci.* **59**(22-23): 5241-5247.

A.-H.A. Park, R. Jadhav and L.-S. Fan (2003). "CO2 Mineral Sequestration: Chemically Enhnaced Aqueous Carbonation of Serpentine." *Can. J. Chem. Eng.* **81**: 885-890.

D.L. Parkhurst and C.A.J. Appelo (2013). Description of Input and Examples for PHREEQC Version 3—a Computer Program for Speciation, Batch-Reaction, One-Dimensional Transport, and Inverse Geochemical Calculations. U.S. Geological Survey Techniques and Methods, Book 6, Chapter A43, United States Geological Survey.

F. Pinto, C. Franco, R.N. André, et al. (2002). "Co-gasification study of biomass mixed with plastic wastes." *Fuel* **81**: 291-297.

O.S. Pokrovsky and J. Schott (1999). "Processes at the Magnesium-Bearing Carbonates Solution Interface. II. Kinetics and Mechanism of Magnesite Dissolution." *Geochim. Cosmochim. Ac.* **63**(6): 881-897.

O.S. Pokrovsky and J. Schott (2004). "Experimental study of brucite dissolution and precipitation in aqueous solutions: surface speciation and chemical affinity control." *Geochim. Cosmochim. Ac.* **68**(1): 31-45.

O.S. Pokrovsky, J. Schott and A. Castillo (2005). "Kinetics of brucite dissolution at 25°C in the presence of organic and inorganic ligands and divalent metals." *Geochim. Cosmochim. Ac.* **69**(4): 905-918.

O.S. Pokrovsky, J. Schott and F. Thomas (1999). "Processes at the Magnesium-Bearing Carbonates Solution Interface. I. a Surface Speciation Model for Magnesite." *Geochim. Cosmochim. Ac.* **63**(6): 863-880.

J. Pronost, G. Beaudoin, J. Tremblay, et al. (2011). "Carbon Sequestration Kinetic and Storage Capacity of Ultramafic Mining Waste." *Environ. Sci. Technol.* **45**(21): 9413-9420.

G. Raade (1970). "Dypingite, a New Hydrous Basic Carbonate of Magnesium, from Norway." *Am. Mineral.* **55**(9-10): 1457-1465.

H. Ren, Z. Chen, Y. Wu, et al. (2013). "Thermal characterization and kinetic analysis of nesquehonite, hydromagnesite, and brucite, using TG–DTG and DSC techniques." *J. Therm. Anal. Calorim.*

G.T. Rochelle (2009). "Amine Scrubbing for CO_2 Capture." *Science* **325**: 1652-1654.

G.D. Saldi, G. Jordan, J. Schott, et al. (2009). "Magnesite growth rates as a function of temperature and saturation state." *Geochim. Cosmochim. Ac.* **73**(19): 5646-5657.

G.D. Saldi, J. Schott, O.S. Pokrovsky, et al. (2012). "An experimental study of magnesite precipitation rates at neutral to alkaline conditions and 100–200°C as a function of pH, aqueous solution composition and chemical affinity." *Geochim. Cosmochim. Ac.* **83**: 93-109.

G.D. Saldi, J. Schott, O.S. Pokrovsky, et al. (2010). "An experimental study of magnesite dissolution rates at neutral to alkaline conditions and 150 and 200°C as a function of pH, total dissolved carbonate concentration, and chemical affinity." *Geochim. Cosmochim. Ac.* **74**(22): 6344-6356.

K. Sandengen, L.O. Josang and B. Kaasa (2008). "Simple Method for Synthesis of Magnesite (MgCO3)." *Ind. Eng. Chem. Res.* **47**: 1002-1004.

F.L. Sanna, M.R. Hall and M.M. Maroto-Valer (2012). "Post-processing pathways in carbon capture and storage by mineral carbonation (CCSM) towards the introduction of carbon neutral materials." *Energ. Environ. Sci.* **5**(7): 7781.

Y. Sawada, K. Uematsu, N. Mizutani, et al. (1978). "Thermal Decomposition of Hydromagnesite 4MgCO3-Mg(OH)$_2$-4H2O." *J. inorg. nucl. Chem.* **40**(6): 979-982.

R.G. Sawers (2005). "Formate and its role in hydrogen production in Escherichia coli." *Biochem. Soc. T.* **33**(1): 42-46.

F.L. Sayles and W.S. Fyfe (1973). "The crystallization of magnesite from aqueous solution." *Geochim. Cosmochim. Ac.* **37**: 87-99.

H.T. Schaef, C.F. Windisch, B.P. McGrail, et al. (2011). "Brucite [Mg(OH2)] carbonation in wet supercritical CO2: An in situ high pressure X-ray diffraction study." *Geochim. Cosmochim. Ac.* **75**(23): 7458-7471.

D. Schrag (2009). "Coal as low-carbon fuel?" *Nat. Geosci.* **2**: 818-820.

L.J. Sealock, D.C. Elliott and R.S. Butner (1985). Developemnt of an Advanced Water-Gas Shift Conversion System: Final Report. Richland, WA, Pacific Northwest Laboratory

S. Senthoorselvan, S. Gleis, S. Hartmut, et al. (2009). "Cyclic Carbonation Calcination Studies of Limestone and Dolomite for CO2 Separation From Combustion Flue Gases." *J. Eng. Gas Turb. Power* **131**(1): 011801.

J. Shabaker (2003). "Aqueous-phase reforming of methanol and ethylene glycol over alumina-supported platinum catalysts." *J. Catal.* **215**(2): 344-352.

D. Sheila and P.R. Khangaonkar (1989). "Precipitation of Magneisum Carbonate." *Hydrometallurgy* **22**(1): 249-258.

S.-M. Shih, C.-S. Ho, Y.-S. Song, et al. (1999). "Kinetics of the Reaction of Ca(OH)2 with CO2 at Low Temperature." *Ind. Eng. Chem. Res.* **38**: 1316-1322.

G.L. Smithson and N.N. Bakhshi (1973). "Kinetics and Mechanism of Carbonation of Magnesium Oxide Slurries." *Ind. Eng. Chem. Process Des. Develop.* **12**(1): 99-106.

N. Sridhar and D. Hill (2011). Electrochemical Conversion of CO2 - Opportunities and Challenges, Research and Innovation - Position Paper, DNV GS.

R.W. Stevens, A. Shamsi, S. Carpenter, et al. (2010). "Sorption-enhanced water gas shift reaction by sodium-promoted calcium oxides." *Fuel* **89**(6): 1280-1286.

S.C. Stultz and J.B. Kitto (1992). Steam - Its Generation and Use. Baberton, Babcock & Wilcox, a McDermott Company.

W. Stumm (1992). Chemistry of the Solid-Water Interface : Processes at the Mineral-Water and Particle-Water Interface in Natural Systems. New York, Wiley.

N. Sutradhar, A. Sinhamahapatra, S.K. Pahari, et al. (2011). "Controlled Synthesis of Different Morphologies of MgO and Their Use as Solid Base Catalysts." *J. Phys. Chem. C* **115**(25): 12308-12316.

E.J. Swanson, K.J. Fricker, M. Sun, et al. (2014). "Directed Precipitation of Hydrated and Anhydrous Magnesium Carbonates for Carbon Storage." *Phys. Chem. Chem. Phys. (in Review)*

S. Teir, R. Kuusik, C.-J. Fogelholm, et al. (2007). "Production of magnesium carbonates from serpentinite for long-term storage of CO2." *Int. J. Miner. Process.* **85**(1-3): 1-15.

D.D. Tommaso and N.H. de Leeuw (2010). "Structure and dynamics of the hydrated magnesium ion and of the solvated magnesium carbonates: insights from first principles simulations." *Phys. Chem. Chem. Phys.* **12**(4): 894.

D.A. Torres-Rodríguez and H. Pfeiffer (2011). "Thermokinetic analysis of the MgO surface carbonation process in the presence of water vapor." *Thermochim. Acta* **516**(1-2): 74-78.

T. Tsuji and A. Hatayama (2009). "Gasification of waste plastics by steam reforming in a fluidized bed." *J. Mater. Cycles Waste* **11**(2): 144-147.

UN (2012). World Population Prospects: The 2012 Revision. New York, Population Division of the Department of Economic and Social Affairs of the United Nations Secretariat.

C. Ungermann, V. Landis, S.A. Moya, et al. (1979). "Homogenious Catalysis of the Water Gas Shift Reaction by Ruthenium and Other Metal Carbonyls. Studies in Alkaline Solutions." *J. Am. Chem. Soc.* **101**(20): 5922-5929.

V. Vágvölgyi, R.L. Frost, M. Hales, et al. (2008a). "Controlled Rate Thermal Analysis of Hydromagnesite." *J. Therm. Anal. Calorim.* **92**(3): 893-897.

V. Vágvölgyi, M. Hales, R.L. Frost, et al. (2008b). "Conventional and Controlled Rate Thermal Analysis of Nesquehonite Mg(HCO3)(OH)-2(H2O)." *J. Therm. Anal. Calorim.* **94**(2): 523-528.

G.P. Van Der Laan and A.A.C.M. Beenackers (1999). "Kinetics and Selectivity of the Fischer–Tropsch Synthesis: A Literature Review." *Cataly. Rev.* **41**(3-4): 255-318.

H. Vehkamäki (2006). Classical Nucleation Theory in Multicomponent Systems. Berlin Heidelberg New York, Springer-Verlag.

S. Werner, N. Szesni, M. Kaiser, et al. (2010). "Ultra-Low-Temperature Water-Gas Shift Catalysis using Supported Ionic Liquid Phase (SILP) Materials*." *ChemCatChem* **2**(11): 1399-1402.

G.H. Wolf, A.V.G. Chizmeshya, J. Diefenbacher, et al. (2004). "In Situ Observations of CO2 Sequestration Reactions Using Novel Microreactor System." *Environ. Sci. Technol.* **38**: 932-936.

Y. Xiong and A.S. Lord (2008). "Experimental investigations of the reaction path in the MgO–CO2–H2O system in solutions with various ionic strengths, and their applications to nuclear waste isolation." *Appl. Geochem.* **23**(6): 1634-1659.

A. Yoshida, T. Nishimura, H. Kawaguchi, et al. (2005). "Enhanced Hydrogen Production from Formic Acid by Formate Hydrogen Lyase-Overexpressing Escherichia coli Strains." *Appl. Environ. Microbio.* **71**(11): 6762-6768.

M.M. Yung, W.S. Jablonski and K.A. Magrini-Bair (2009). "Review of Catalytic Conditioning of Biomass-Derived Syngas." *Energ. Fuel* **23**(4): 1874-1887.

R. Zevenhoven, S. Teir and S. Eloneva (2008). "Heat optimisation of a staged gas–solid mineral carbonation process for long-term CO2 storage." *Energy* **33**(2): 362-370.

K. Zhang, X.S. Li, Y. Duan, et al. (2013). "Roles of double salt formation and NaNO3 in Na2CO3-promoted MgO absorbent for intermediate temperature CO2 removal." *Int. J. Greenhouse Gas Control* **12**: 351-358.

Z. Zhang, Y. Zheng, Y. Ni, et al. (2006). "Temperature and pH-Dependent Morphology and FT-IR Analysis of Magnesium Carbonate Hydrates." *J. of Phys. Chem. B* **110**: 12969-12973.

H. Zhao, N. Dadap and A.-H.A. Park (2010). "Tailored synthesis of precipitated magnesium carbonates as carbon-neutral filler materials during carbon mineral sequestration." *In The 13th International Conference on Fluidization - New Paradigm in Fluidization*: 821-828.

H. Zhao, Y. Park, D.H. Lee, et al. (2013). "Tuning the dissolution kinetics of wollastonite via chelating agents for CO2 sequestration with integrated synthesis of precipitated calcium carbonates." *Phys. Chem. Chem. Phys.* **15**(36): 15185-15192.

L. Zhao, L. Sang, J. Chen, et al. (2010). "Aqueous Carbonation of Natural Brucite: Relevance to CO2 Sequestration." *Environ. Sci. Technol.* **44**(1): 406-411.

L. Zhao, H. Wang, S. Qing, et al. (2010). "Characteristics of gaseous product from municipal solid waste gasification with hot blast furnace slag." *J. Nat. Gas Chem.* **19**(4): 403-408.

P.Z. Zhou and R.D. Srivastava (1991). Status Review of Fischer–Tropsch Slurry Reactor Catalyst/Wax Separation Techniques, Prepared for U.S. Department of Energy Pittsburgh Energy Technology Center.

Appendix 1: List of Publications

Fricker, K.J. and A.-H.A. Park (2013). "Effect of H_2O on $Mg(OH)_2$ carbonation pathways for combined CO_2 capture and storage." *Chem. Eng. Sci.* **100**: 332-341.

Fricker, K.J. and A.-H.A. Park (2014). "Investigation of the Different Carbonate Phases and their Formation Kinetics during $Mg(OH)_2$ Slurry Carbonation." *Ind. Eng. Chem. Res. (in Review).*

Swanson, E.J., K.J. Fricker, et al. (2014). "Directed Precipitation of Hydrated and Anhydrous Magnesium Carbonates for Carbon Storage." *Phys. Chem. Chem. Phys. (in Review).*

Fricker, K.J. and A.-H.A. Park (2014). "Enhanced Water Gas Shift Reaction in the Presence of a $Mg(OH)_2$ slurry in a High Pressure Aqueous System." *Int. J. Hydrogen Energ. (in Preparation).*

Gadikota, G., K.J. Fricker, et al. (2014). "Carbonated silicate minerals and industrial wastes as construction materials." *Minerals* (*in Preparation).*